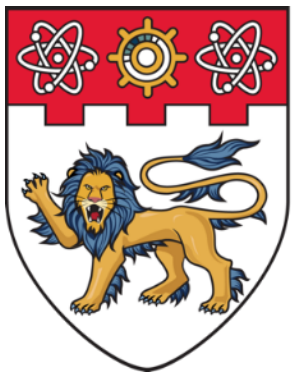

NANYANG TECHNOLOGICAL UNIVERSITY
SINGAPORE

SYNTHESIS AND APPLICATIONS OF TRANSITION METAL DICHALCOGENIDE-BASED NANOMATERIALS

SHI ZHENYU

SCHOOL OF MATERIALS SCIENCE AND ENGINEERING

2020

SYNTHESIS AND APPLICATIONS OF TRANSITION METAL DICHALCOGENIDE-BASED NANOMATERIALS

SHI ZHENYU

SCHOOL OF MATERIALS SCIENCE AND ENGINEERING

A thesis submitted to the Nanyang Technological University
in partial fulfilment of the requirement for the degree of
Doctor of Philosophy

2020

Statement of Originality

I hereby certify that the work embodied in this thesis is the result of original research, is free of plagiarised materials, and has not been submitted for a higher degree to any other University or Institution.

27th-July-2020 史振宇

. . . .

Date Shi Zhenyu

Supervisor Declaration Statement

I have reviewed the content and presentation style of this thesis and declare it is free of plagiarism and of sufficient grammatical clarity to be examined. To the best of my knowledge, the research and writing are those of the candidate except as acknowledged in the Author Attribution Statement. I confirm that the investigations were conducted in accord with the ethics policies and integrity standards of Nanyang Technological University and that the research data are presented honestly and without prejudice.

27th-July-2020 

. . . .

Date Assoc Prof Zhang Qichun

Authorship Attribution Statement

This thesis contains material from 1 paper published in the following peer-reviewed journal in which I am listed as the co-first author.

Chapter 2 is published as Y. Ge, Z. Shi, C. Tan, Y. Chen, H. Cheng, Q. He, and H. Zhang, Two-Dimensional Nanomaterials with Unconventional Phases. *Chem* **6**, 1237-1253 (2020). DOI: 10.1016/j.chempr.2020.04.004.

The contributions of the co-authors are as follows:

- Prof. Zhang Hua proposed the initial idea and edited the manuscript drafts.
- I co-wrote the manuscript with Dr. Ge Yiyao.
- All the authors gave suggestions to revise the manuscript together.

27th-July-2020

史振宇

. . . . . .

Date

. . . . . .

Shi Zhenyu

Abstract

Great advancement has been achieved in two-dimensional (2D) materials which greatly accelerated the research in 2D transition metal dichalcogenides (TMDs) nanomaterials owing to their diverse chemical compositions, atomic structures and unique properties. One of the most important features of 2D TMDs nanomaterials is that they can exist in different polymorphisms with various electronic properties. For example, Group-VI TMDs nanosheets (NSs), such as MoS_2 and $MoSe_2$, exhibit the thermodynamically stable 2H-phase, which is semiconducting, and the metastable 1T or 1T′ phase, which is metallic or semi-metallic. However, due to the metastable nature, the preparation of Group-VI TMDs nanosheets with 1T or 1T′ phase is still required further investigation, thus their intrinsic properties remain unclear. Only the TMDs NSs with mixed phases, *i.e.*, 2H, 1T and 1T′ phases mixed together, can be obtained by using the traditional methods, such as lithium intercalation, hydrothermal or solvothermal methods. Therefore, it is highly desired to develop a facile, controllable method towards the preparation of 1T- or 1T′-TMDs NSs with high phase purity to in-depth study their properties and applications.

First, we reported an electrochemical intercalation and exfoliation method that successfully prepared a variety of metastable 1T′-TMDs materials such as 1T′-MoS_2, 1T′-$MoSe_2$ and 1T′-MoSSe NSs with high quality, high yields, and high phase purity. The as-prepared high purity 1T′-MoS_2 NSs exhibited enhanced hydrogen evolution reaction (HER) activity as compared with the 2H counterpart, which is prepared by using the same method. The electrochemical intercalation and exfoliation method can also be extended to exfoliate other layered materials, showing great generality.

Second, the high phase purity 1T′-MoS_2 and 2H-MoS_2 NSs serve as ideal platforms for the growth of secondary nanomaterials, which enables us to fabricate novel MoS_2-based hybrids nanomaterials and investigate the crystal phase-dependent properties. Here we reported the preparation of Pt/1T′-MoS_2 and Pt/2H-MoS_2 hybrid nanomaterials, in which the Pt nanostructures exhibit distinct electronic properties. The Pt/1T′-MoS_2 shows

excellent HER activity and stability. At the overpotential of only 10 mV, Pt/1T′-MoS_2 can reach a current density of 10 mA cm^{-2}, which is dramatically lower than the Pt/2H-MoS_2 (reaching 10 mA cm^{-2} at the overpotential of 113 mV) and even the commercial Pt/C catalyst (reaching 10 mA cm^{-2} at the overpotential of 19 mV). The superior catalytic performance of Pt/1T′-MoS_2 highlights the significance of the crystal phase for structure and property tailoring towards promising applications.

Lay Summary

The vast consumption of fossil fuel in the modern world established the economic prosperity. However, the growing scarcity of non-renewable fossil fuels will lead to the energy crisis all over the world in the near future. In the meantime, the usage of fossil fuels causes the global environmental crisis. Therefore, developing environmentally friendly clean energy is of great importance to solve both the energy and environmental crisis.

From the clean energy production point of view, hydrogen evolution produced by a clean electrochemical water splitting method has been considered as the most promising clean energy carrier to replace traditional fossil fuel. Noble metal catalysts, especially Platinum is the best hydrogen evolution reaction (HER) catalysts. However, the high expense and scarcity greatly inhibit the vast utilization of noble metal. To successfully produce hydrogen from water splitting, the highly efficient and durable catalyst is most desired. In this work, the preparation of high phase purity 1T′-MoS_2 NSs and the Pt/1T′-MoS_2 electrocatalysts aims to solve this problem. The as-prepared Pt/1T′-MoS_2 electrocatalysts exhibited a superior HER performance outperforming the commercial Pt/C catalysts, showing great potential in the further practical application. The emphasis of 1T′-MoS_2 in this work paves a new way towards the preparation of new type of electrocatalysts towards various applications.

Acknowledgments

First and foremost, I would like to express my deep gratitude to my supervisor Professor Zhang Hua, and my co-supervisor Associate Professor Zhang Qichun, for their continuous support, encouragement, valuable guidance, and useful critiques throughout my Ph.D. period.

Special gratitude is dedicated to Dr. Xiao Zhang, for his constructive and crucial guidance in my Ph.D. period. He plays an important role in the early stage of my Ph.D. period and helps me establish my own research ideas. His patient guidance, enthusiasm, and encouragement support me to pursue perfection in the research work.

Besides, I would thank all the group members, especially Dr. Zhao Meiting, Dr. Liu Guigao, Dr. Yiyao Ge, Dr. Gwang-Hyeon Nam, Dr. Lai Zhuangchai, Dr. Qiyuan He, Dr. Chaoliang Tan, Dr. Bo Chen, from Professor Zhang Hua's group, for their kind help and valuable suggestions. I also express my great gratitude to other group members, it is my great honor to be one of this group.

I also would like to extend my thanks to the technicians in the MSE laboratory and FACTS who have ever given me detailed training and suggestions on the equipment usages.

In addition to the faculty at Nanyang Technological University, I also want to show my great gratitude to Prof Ying Zhang, Prof Zhimin Luo, Prof Xiehong Cao, and Dr. Shibo Xi and Dr. Ling Chongyi for their kind help in the research work.

Finally, I must express my profound gratitude to my parents, for their unlimited support all the time. I also express my thanks to my beloved girlfriend Ms. Li Dan for her strongest support.

Table of Contents

Table Captions

Figure Captions

Figure 2.1 More than 40 different layered TMDs were found in nature. The periodic table highlighted the elements that mainly existed in layered TMDs materials. Partial highlighted elements mean only selected numbers of corresponding dichalcogenides have layered structure.

Figure 2.2 The phase and properties relationship in TMDs.

Figure 2.3 As-exfoliated MoS_2 nanosheets. **a**. Optical image of the MoS_2 nanosheets. The areas with different colors correspond to MoS_2 nanosheets with various layers, while the blue area indicates the substrate. Based on the contrast, the layer number of MoS_2 was labeled as "1L", "2L", "4L" and "6L" which represented for monolayer, bilayer, quadrilayer and hexalayer. **b**, AFM image of the same MoS_2 nanosheets. **c**, Thickness of the exfoliated sample along the red line in **Figure** b.

Figure 2.4 a-c, STEM images of single-layer MoS_2 in a different region with yellow line enclosed 1T region, while blue and red lines included 1T′ and 2H phase. The scale bar is 2 nm. **d-f**, High resolution STEM images of the as-exfoliated single-layer MoS_2 in **d**, 2H, **e**, 1T, and **f**, 1T′ phase region. The Mo and S atom position are indicated with blue and yellow balls. **g**, **h**, Signal intensity along the lines showed 2H phase (**d**) 1T phase (**e**).

Figure 2.5 a, Scheme of the electrochemical exfoliation process. **b**, TEM image of the as-exfoliated MoS_2 monolayer. **c**, AFM image of as-prepared MoS_2 monolayer. Inset in **b** showed a snapshot of MoS_2 solution. Inset in **c** showed height distribution of the same MoS_2 monolayers.

Figure 2.6 As-grown of 1T′ and 2H-MoS_2 monolayers. **a**, Schematic illustration the 1T′, 2H phase MoS_2 structures. Optical images of 1T′ and 2H-MoS_2 monolayer triangular flakes are shown in (**b**) and (**g**). Insets are the AFM images of (inset in **b**) 1T′ and (inset in **b**) 2H-

MoS_2 monolayers. (**c**) 1T′ and (**g**) 2H-MoS_2 monolayers STEM images, respectively. Insets are the SAED patterns of (inset in **c**)1T′ phase and (inset in h)2H phase MoS_2 nanosheets, respectively. Raman spectra of (**d**) 1T′ phase and (**i**) 2H phase MoS_2 monolayers. XPS spectra of (**e**) 1T′ and (**j**) 2H-MoS_2 monolayers of Mo 3d orbits. **f**, Phase diagram influenced by H_2 concentration and reaction temperature in the growth process of MoS_2.

Figure 2.7 a-c HRSTM images of MoS_2 monolayer grown on graphite (**a**) before and (**b, c**) after plasma radiation. Inset in (**a**) showed the FFT pattern of panel a, where larger set of hexagonal patterns are the top S atoms of MoS_2, and the smaller one corresponds to the Moiré pattern. **d**, Schematics of three types of devices. **e,** Schematic illustration of the 1T-MoS2 contacted device fabrication process.

Figure 2.8 Structure and application analysis of Pt-MoS_2 hybrid nanomaterials. **a**, TEM image (scale bar, 100 nm) and **b**, magnified TEM image (scale bar, 5 nm) of Pt NPs synthesized on a MoS_2 nanosheet. **c**, the corresponding SAED pattern of a Pt-MoS_2 hybrid structure. **d-f**, HRTEM image showed distinguishable lattice fringes for Pt and MoS_2 of the Pt-MoS_2 hybrid (scale bar, 2 nm). Inset in f, the photograph of the Pt-MoS_2 solution. **g-h**, Polarization curves (**g**), and the corresponding Tafel plots (**h**) of Pt-MoS_2, Pt/C, and MoS_2 nanosheets, respectively.

Figure 2.9 a, Scheme shows the Pd doping process. **b**, Dark-field STEM image of the 1% Pd-MoS_2. Blue balls represent for Mo and the yellow balls are S atoms, respectively. Scale bar: 1 nm. **c**, LSV curves and the **d**, Tafel plots of samples.

Figure 4.1 Ultraviolet-visible absorption spectra of the 1T′-MoS_2 sonicated in the DMF solvent for **a**, 1 minute, **b**, 5 minutes, and **c**, 30 minutes. Insets show the photographs of the as-sonicated samples in DMF samples.

Figure 4.2 a, UV-Vis spectrum of the lithium intercalation exfoliated 1T′-MoS_2 NSs. Inset in **a** shows the photograph of the as-exfoliated sample in water.

Figure 4.3 a, SEM image and the corresponding **b**, EDS spectra, and **c**, element composition of $KMoS_2$ crystals. **d**, SEM image, and the corresponding **e**, EDS spectra and **f**, element composition of K_xMoS_2 crystals after washing.

Figure 4.4 a, XRD patterns showing the structural transition during the intercalation process.

Figure 4.5 Schematic illustration of preparing 1T′-MoS_2 NSs from K_xMoS_2 crystals through the electrochemical intercalation (Step 1) and subsequent exfoliation (Step 2).

Figure 4.6 Morphology characterization of the exfoliated 1T′-MoS_2 nanosheets: **a**, SEM image of 1T′-MoS_2 NSs. **b**, AFM image of the 1T′-MoS_2 NSs. Insets in **b**: the height profiles and measured thicknesses of 1T′-MoS_2 NSs. **c**, Statistical analysis of the thickness of 1T′-MoS_2 NSs measured by AFM. **d**, TEM image and **e**, the corresponding SAED pattern of the 1T′-MoS_2 NSs. **f**, HAADF-STEM image of a typical 1T′-MoS_2 NS. Inset: the corresponding FFT pattern.

Figure 4.7 a, HAADF-STEM image of 1T′-MoS_2 NS. **b**, The corresponding line-scanning intensity profile obtained from the white dotted line in **a**.

Figure 4.8 a,b, Schematic illustrations of the atomic structures of 1T′-MoS_2 (**a**) and 2H-MoS_2 (**b**). The red dashed lines in a show the zig-zag chain of Mo atoms in 1T′-MoS_2 with a shortest Mo-Mo distance of 2.78 Å. The black dashed lines in b show the (100) planes of 2H-MoS_2 with a theoretical interlayer spacing of 2.74 Å.

Figure 4.9 a, STEM image, and **b**,**c**, the corresponding EDS mappings of a representative 1T′-MoS_2 NS. **d**, EDS spectrum of the 1T′-MoS_2 NS in **a**, indicating no detectable potassium (Kα 3.31 eV), bromide (Lα 1.48 eV), and other residues in 1T′-MoS_2 NS. Inset in **d**, the corresponding elemental ratio.

Figure 4.10 a, The K 2*p* XPS spectra of the K_xMoS_2 crystals and the obtained 1T′-MoS_2 NSs.

Figure 4.11 a, SEM image of the exfoliated 2H-MoS_2 NSs. **b**, TEM and **c**, HRTEM images of a representative 2H-MoS_2 NS. Inset in **b** shows the corresponding SAED pattern. **d**, EDS spectrum and the element ratio (inset in **d**) of the 2H-MoS_2 NSs. **e**, AFM image and the measured thicknesses (insets in **e**) of 2H-MoS_2 NSs. **f**, Statistical analysis of the thickness of 2H-MoS_2 NSs measured by AFM.

Figure 4.12 a, UV-Vis spectra of the exfoliated 1T′-MoS_2 NSs and 2H-MoS_2 NSs dispersed in DMF. Four featured peaks are clearly observed in the UV-Vis spectrum of 2H-MoS_2 NSs as indicated by the black dashed lines.

Figure 4.13 a, XPS spectra of exfoliated 1T′-MoS_2 NSs and 2H-MoS_2 NSs. The grey circles and the solid lines show the experimental XPS data and the corresponding deconvoluted spectra, respectively. **b**, Raman spectra of exfoliated 1T′-MoS_2 NSs and 2H-MoS_2 NSs.

Figure 4.14 a, Raman spectra of 1T′-MoS_2 crystals and 1T′-MoS_2 NSs. **b**, Raman spectra showing the phase transition from 1T′-MoS_2 NSs to 2H-MoS_2 NSs under the continuous laser beam.

Figure 4.15 a, SEM, **b**, AFM, **c**, TEM, and **d**, the corresponding SAED patterns of the obtained 1T′-$MoSe_2$ NSs.

Figure 4.16 a, SEM, **b**, AFM, **c**, TEM, and **d**, the corresponding SAED patterns of the obtained 1T′-MoSSe NSs.

Figure 4.17 TEM images of the as-exfoliated **a**, Te, **b**, BN, **c**, $NbSe_2$, and **d**, $CuInP_2S_6$.

Figure 4.18 Electrocatalytic HER performance of 1T′-MoS_2 and 2H-MoS_2 nanosheets. **a**, Polarization curves and the corresponding Tafel plots of 1T′-MoS_2 and 2H-MoS_2

nanosheets in comparison to commercial Pt/C catalysts. **b**, Current-voltage (I-V) characteristic curves of 1T′-MoS_2 and 2H-MoS_2 films.

Figure 4.19 Electrocatalytic HER performance of 1T′-MoS_2 and 2H MoS_2 nanosheets. **a**, Polarization curves and the corresponding Tafel plots of 1T′-MoS_2 and 2H-MoS_2 nanosheets in comparison to commercial Pt/C catalysts.

Figure 4.20 a, EIS spectra of 1T′-MoS_2 NSs and 2H-MoS_2 NSs. **b**, Current-voltage (I-V) characteristic curves of 1T′-MoS_2 and 2H-MoS_2 films.

Figure 5.1 a, TEM image and. **b**, The diameter distribution of Pt nanoclusters with 100 nanoclusters counted. **c**, the corresponding SAED pattern of Pt/1T′-MoS_2. **d**, HAADF-STEM image and **d**, the magnified HAADF-STEM image of Pt/1T′-MoS_2. **e**, High resolution EDS mapping images the Pt/1T′-MoS_2.

Figure 5.2 a, STEM image and the **b**,**c**, high resolution EDS line-scanning results of the Pt/1T′-MoS_2.

Figure 5.3 a, Large area EDS mapping results and **b**, the EDS spectrum of Pt/1T′-MoS_2.

Figure 5.4 a, TEM image of Pt/2H-MoS_2. Inset: the diameter distribution histogram of PtNPs grown on 2H-MoS_2 NSs. **b**, SAED pattern of Pt/2H-MoS_2. **c**, HAADF-STEM image of Pt/2H-MoS_2. **d**, The corresponding line-scanning intensity profiles obtained from the areas **i** and **ii** in **c**, respectively. The average lattice spacings of Pt(111) planes were calculated to be 2.28 Å, which is consistent with the theoretical value of 2.27 Å.

Figure 5.5 a, EDS mapping images and **b**, the EDS spectrum of Pt/2H-MoS_2.

Figure 5.6 a, Pt 4*f*, and b, Mo 3*d* XPS spectra of Pt/1T′-MoS_2 and Pt/2H-MoS_2. The grey circles and the solid lines in (**a**,**b**) show the experimental XPS data and the corresponding deconvoluted spectra, respectively.

Figure 5.7 a, Raman spectra of 1T′-MoS_2 NSs and Pt/1T′-MoS_2. **b**, Raman spectra of 2H-MoS_2 NSs and Pt/ MoS_2 NSs.

Figure 5.8 The S K-edge XANES spectra of Pt/1T′-MoS_2, commercial PtS_2, Pt/2H-MoS_2, and Pt foil.

Figure 5.9 a, TEM image, **b**, HRTEM image, and **c**, STEM image and the corresponding EDS mappings of the commercial Pt/C catalysts.

Figure 5.10 a, HER polarization curves of Pt/1T′-MoS_2, Pt/2H-MoS_2, 1T′-MoS_2 NSs, 2H-MoS_2 NSs, and commercial Pt/C electrocatalysts loaded on the glassy carbon electrode. The weights of 1T′-MoS_2 NSs, 2H-MoS_2 NSs and Pt/1T′-MoS_2 were kept the same (0.1 mg cm^{-2}). The mass loadings of Pt were kept the same (0.01 mg cm^{-2}) for Pt/1T′-MoS_2, Pt/2H-MoS_2 and Pt/C. **b**, Tafel plots of the catalysts derived from **a**. **c**, Mass activities of Pt/1T′-MoS_2 and commercial Pt/C. **d**, Long-term stability test for Pt/1T′-MoS_2. The polarization curves were recorded before and after 10,000 potential cycles. Inset: the chronoamperometric test of Pt/1T′-MoS_2, showing that the current density remains stable over 30 h. **e**, Comparison of the TOF values of Pt/1T′-MoS_2 and Pt/C. **f**, EIS spectra of Pt/1T′-MoS_2 and Pt/2H-MoS_2, showing that the R_{ct} of Pt/1T′-MoS_2 is much lower than that of Pt/2H-MoS_2.

Figure 6.1 a, TEM image and **b**, the corresponding SAED pattern of Pd/1T′-MoS_2. **c**, HAADF-STEM image and **d**, the magnified HAADF-STEM image of Pd/1T′-MoS_2.

Table Captions

Abbreviations

2D	Two dimensional
CV	Cyclic Voltammetry
CVD	Chemical Vapor Deposition
CVT	Chemical Vapor Transport
DFT	Density Functional Theory
EDS	Energy Dispersive X-ray Spectroscopy
FFT	fast Fourier Transform
STEM	Scanning Transmission Electron Microscopy
HAADF	High-Angle Annual Dark-Field
HRTEM	High Resolution Transmission Electron Microscopy
SAED	Selected Area Electron Diffraction
SEM	Scanning Electron Microscopy
TMDs	Transition metal dichalcogenides
TEM	Transmission Electron Microscopy
XRD	X-ray Diffraction
XPS	X-Ray Photoelectron Spectroscopy

Chapter 1

Introduction

This chapter acts as a brief introduction to the whole thesis. First, a precise summary of the hypothesis and the research background of the metastable phase TMDs and their hybrids is given. Subsequently, the objectives and scope of this thesis are proposed. Then, a brief description is given to the three parts of the research works which will be presented in detail in the following Chapter 4-6. Finally, the main findings, outcomes, and perspectives of this thesis are concluded in Chapter 7.

1.1 Hypothesis/Problem Statement

Two-dimensional (2D) nanomaterials have become one of the fastest developing areas since the first isolation of graphene in 2004[1]. From three-dimensional bulk materials to 2D nanomaterials such as nanosheets (NSs), nanoribbons, etc., a variety of unique properties arise with enormous potential in both fundamental research and practical application.

As one of the most attractive areas, 2D transition metal dichalcogenides (TMDs) with various polymorphs have been widely studied towards various applications such as energy storage[2], electronic devices[3], and electrocatalysis[4]. Recently, metastable phase 2D TMDs with the unusual physiochemical properties compared with their stable counterparts, open up a new way towards the properties modulation[5-7]. For example, Group-VI TMDs, such as MoS_2 and $MoSe_2$, exhibit the thermodynamically stable 2H-phase, which is semiconducting, and the metastable 1T or 1T′ phase, which is metallic or semi-metallic[8,9]. The 1T- or 1T′-MoS_2 possess dramatically lower charge transfer resistance and would exhibit much better HER performance as compared with the 2H counterpart[9-11]. However, to prepare Group-VI TMDs NSs with 1T or 1T′ phase remains a great challenge owing to their metastable nature. Recently, the preparation of high phase purity 1T′-TMDs crystals has been reported by using a gas-solid synthesis method[9]. Therefore, exfoliating the 1T′-TMDs crystals in a controllable way could be one strategy to prepare the 1T′-TMDs NSs. Traditionally, the exfoliating of TMDs crystals can be accomplished by a Lithium intercalation and exfoliation process[12,13]. However, as a high electron donation, the Lithium intercalation will change the original phase of TMDs resulting in mixed-phase TMDs NSs (2H phase TMDs mixed with 1T or 1T′ phase TMDs). Therefore, the intercalation of the molecule with limited electron donation to the TMDs NSs should be a possible route to reserve the 1T or 1T′ phase of the TMDs crystals during the intercalation and exfoliation process. Upon successful preparation, the detailed phase-relationship of 2D TMDs materials study can also be executed.

2D TMDs have been regarded as ideal platforms for the growth of secondary nanomaterials to prepare the TMDs-based hybrids towards enhanced performances towards various

promising applications[14-17]. Compared with the semiconducting 2H phase TMDs, the 1T′-TMDs with low charge transfer resistance can exhibit enhanced electrocatalytic activities. Therefore, incorporating noble metals on 1T′-TMD NS templates to form noble metal-TMDs hybrids can exhibit enhanced performance towards the electrocatalytic hydrogen evolution reaction (HER)[9-11]. Various researches have been focused on the preparation of metastable TMDs-based electrocatalysts. Although various 1T or 1T′-MoS_2-based hybrids have been reported with versatile properties and functionalities, the role of MoS_2 crystal phase in directing the growth of second deposited materials is rarely investigated. The grand difficulty lies in preparing 1T or 1T′-MoS_2 with high phase purity owing to the metastable nature of 1T or 1T′ phase. The reported MoS_2-based hybrids only based on the 2H-MoS_2 or the mixed-phase MoS_2. Although the mixed-phase MoS_2-based hybrids exhibit better electrocatalysis performance than the hybrids based on the 2H-MoS_2 templates[18,19], the presence of 2H-MoS_2 with high charge transfer resistance limits the further enhancement of their electrochemical performance. Therefore, the successful preparation of high phase purity 1T-or 1T′-TMDs NSs could enable us to prepare the novel electrocatalysts towards highly efficient hydrogen evolution.

This thesis tests the following hypotheses: First, the 2D TMDs with thermodynamically metastable phases can be prepared with electrochemical intercalation and exfoliation process. Second, the thermodynamically metastable 2D TMDs with superior HER activity could be an ideal template for the growth and of noble metal nanostructures towards enhanced HER performance.

1.2 Objectives and Scope

The present research aims to achieve the following objectives:

First, to develop a general method towards the preparation of metastable 2D TMDs with high yield, high quality, and high phase purity. Second, to incorporate novel noble nanostructures with metastable 2D TMDs to prepare electrocatalysts towards enhanced HER performance.

1.3 Dissertation Overview

The thesis addresses the preparation of metastable 2D TMDs nanomaterials by mild electrochemical intercalation and exfoliation method to maintain the high phase purity. The thesis also demonstrates that the metastable phase 2D TMDs-based electrocatalysts exhibited a much enhanced electrocatalytic performance. The role of TMD crystal phase in determining the electrocatalytic performance is uncovered in this thesis. This thesis paves a new way of developing highly efficient electrocatalysts based on the metastable phase TMDs NSs.

Chapter 1 provides a rationale for the research and outlines the goals and scope.

Chapter 2 reviews the literature regarding the current research progress on the preparation of 2D TMDs nanomaterials with an emphasis on the metastable TMDs. The metastable TMDs-based electrocatalysts are also introduced as following.

Chapter 3 discusses rational design and selection of experimental methods and target materials, the detailed preparation procedures, characterization techniques, calculation models and principles, as well as the potential applications.

Chapter 4 elaborates the preparation and characterizations of metastable 1T′-TMDs NSs. The obtained solution-processable 1T′-TMDs NSs exhibit high phase purity, high crystallinity, large lateral size, and ultrathin nature. The conductivity and electrocatalytic performance are also tested.

Chapter 5 elaborates the epitaxial growth of noble metal nanostructures on 1T′ and 2H-MoS_2 NSs. The differences in structure, properties, and applications are compared in detail to unravel the crystal phase effect. The obtained Pt/1T′-MoS_2 exhibited a superior performance towards HER.

Chapter 6 summarizes the whole thesis and discusses the reconnaissance research that can be carried out in the near future.

1.4 Findings and Outcomes/Originality

This research led to several novel outcomes by:

1. Establishing a facile and straightforward method to prepare 1T′ phase TMDs NSs. The obtained 1T′-MoS_2 exhibited high phase purity, high crystallinity, large size, and ultrathin thickness. In addition, such a method could also be utilized to successfully exfoliate numbers of 1T′ phase TMDs such as 1T′-$MoSe_2$, 1T′-MoSSe. Many other kinds of layered materials have also been exfoliated successfully by such a method which proved the generality of our electrochemical exfoliated method. As a proof-of-concept application, the obtained 1T′-MoS_2 exhibited superior performance towards HER as compared with the 2H-MoS_2.

2. Correlating the crystal phase and properties of MoS_2-based hybrid nanomaterials. Specifically, Pt nanostructures are grown on 1T′-MoS_2 and 2H-MoS_2 NSs under the same photoreduction process, and denoted as Pt/1T′-MoS_2 and Pt/2H-MoS_2, respectively. The Pt/1T′-MoS_2 showed excellent HER activity (reaching 10, and 50 mA cm^{-2} current density at only 10, and 30 mV overpotential, respectively), outperforming the Pt/2H-MoS_2 (reaching 10, and 50 mA cm^{-2} current density at 113, and 235 mV overpotential, respectively) and most of the previously reported electrocatalysts. The exceptional performance can be ascribed to the synergetic effect between highly conductive 1T′-MoS_2 substrate and Pt nanoclusters with high intrinsic activity.

.

References

1 Novoselov, K. S. Electric Field Effect in Atomically Thin Carbon Films. *Science* **306**, 666-669 (2004).

2 Bonaccorso, F. *et al.* 2D materials. Graphene, related two-dimensional crystals, and hybrid systems for energy conversion and storage. *Science* **347**, 1246501 (2015).

3 Lin, Z. *et al.* Solution-processable 2D semiconductors for high-performance large-area electronics. *Nature* **562**, 254-258 (2018).

4 Voiry, D. *et al.* Enhanced catalytic activity in strained chemically exfoliated WS_2 nanosheets for hydrogen evolution. *Nat. Mater.* **12**, 850-855 (2013).

5 Chhowalla, M. *et al.* The chemistry of two-dimensional layered transition metal dichalcogenide nanosheets. *Nat. Chem.* **5**, 263-275 (2013).

6 Chen, Y. *et al.* Phase engineering of nanomaterials. *Nat. Rev. Chem.* **4**, 243-256 (2020).

7 Yang, H., Kim, S. W., Chhowalla, M. & Lee, Y. H. Structural and quantum-state phase transitions in van der waals layered materials. *Nat. Phys.* **13**, 931-937 (2017).

8 Nam, G. H. *et al.* In-plane anisotropic properties of 1T′-MoS_2 layers. *Adv. Mater.* **31**, e1807764 (2019).

9 Yu, Y. *et al.* High phase-purity 1T′-MoS_2- and 1T′-$MoSe_2$-layered crystals. *Nat. Chem.* **10**, 638-643 (2018).

10 Voiry, D. *et al.* Conducting MoS_2 nanosheets as catalysts for hydrogen evolution reaction. *Nano Lett.* **13**, 6222-6227 (2013)

11 Liu, L. *et al.* Phase-selective synthesis of 1T′ MoS_2 monolayers and heterophase bilayers. *Nat. Mater.* **17**, 1108-1114 (2018).

12 Zeng, Z. *et al.* Single-layer semiconducting nanosheets: High-yield preparation and device fabrication. *Angew. Chem. Int. Ed. Engl.* **50**, 11093-11097 (2011)..

13 Eda, G. *et al.* Coherent atomic and electronic heterostructures of single-layer MoS_2. *ACS Nano*, 2012, **6**, 7311-7317.

14 Geim, A. K. & Grigorieva, I. V. Van der waals heterostructures. *Nature* **499**, 419-425 (2013)

15 Sahoo, P. K., Memaran, S., Xin, Y., Balicas, L. & Gutierrez, H. R. One-pot growth of two-dimensional lateral heterostructures via sequential edge-epitaxy. *Nature* **553**, 63-67 (2018).

17 Liu, G. *et al.* MoS_2 monolayer catalyst doped with isolated co atoms for the hydrodeoxygenation reaction. *Nat. Chem.* **9**, 810-816 (2017).

18 Qi, K. *et al.* Single-atom cobalt array bound to distorted 1T MoS_2 with ensemble effect for hydrogen evolution catalysis. *Nat. Commun.* **10**, 5231 (2019).

19 Li, H. *et al.* Amorphous nickel-cobalt complexes hybridized with 1T-phase molybdenum disulfide via hydrazine-induced phase transformation for water splitting. *Nat. Commun.* **8**, 15377 (2017).

Chapter 2*

Literature Review

This chapter provides a comprehensive review of current progress and challenges in the research area. Transition Metal Dichalcogenides (TMDs) and their metastable phases are first introduced, with a focus on their phase-property relationship. Then, a comprehensive summary of the hitherto reported preparation strategies and the results towards the metastable 2D TMDs was presented, with an emphasis on phase engineering. Thirdly, a detailed summary of previous reported 2D metastable TMDs-based electrocatalysts and the applications were presented. Based on the literature review, a summary and outlook are proposed in the end, highlighting the challenges and perspectives in this area.

---

*This section published substantially as Y. Ge, Z. Shi, C. Tan, Y. Chen, H. Cheng, Q. He, and H. Zhang, Two-Dimensional Nanomaterials with Unconventional Phases. *Chem* **6**, 1237-1253 (2020). DOI: 10.1016/j.chempr.2020.04.004. (No written permission from Elsevier is necessary for thesis purposes)

2.1 Phase Engineering of Transition Metal Dichalcogenide (TMDs)

The two-dimensional (2D) materials family developed strikingly since the first isolation of graphene[1]. From three dimensional to two dimensional, each new material exhibits brand new properties and enormous potential in both various research and application areas. As the fastest-growing part of 2D materials, transition metal dichalcogenides, known as TMDs, have attracted extensive interests owing to the unique properties and promising applications. TMDs can be written as MX_2, where M is a transition metal and X represents the chalcogens[2].

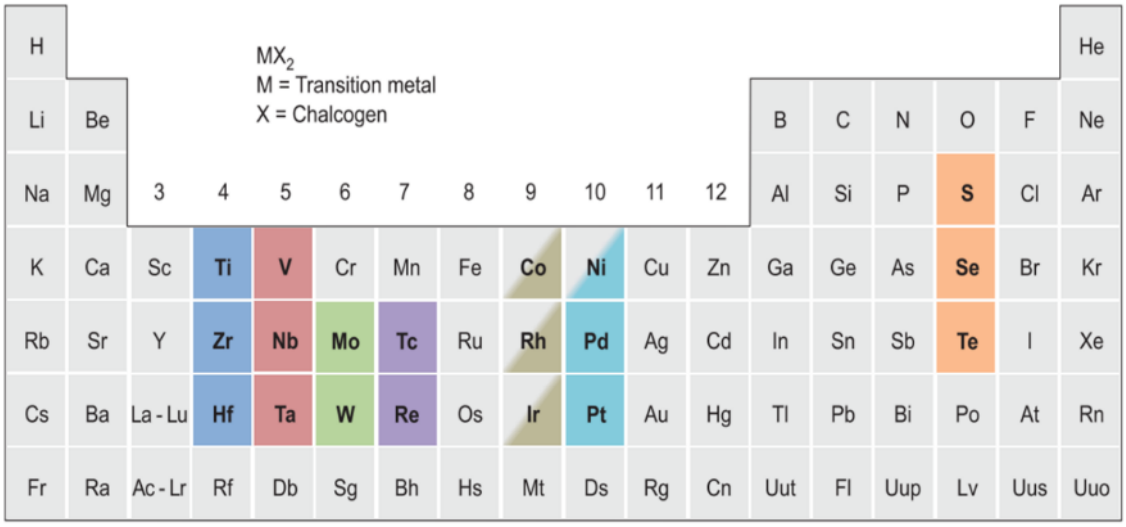

Figure 2.1 More than 40 different layered TMDs were found in nature. The periodic table highlighted the elements that mainly existed in layered TMDs materials. Partial highlighted elements mean only selected numbers of corresponding dichalcogenides have layered structure.[2]

With different elements combination, TMDs materials were found with a wide range of electronic properties, from insulating or semiconducting (e.g. TiS_2, HfS_2, ZrS_2, MoS_2, WS_2) to semi-metallic ($TiSe_2$ and WTe_2), metallic (VSe_2 and NbS_2), superconducting (TaS_2 and $NbSe_2$) and so on[3]. The different electronic properties can be attributed to the different filling numbers of d orbital electrons in transition metals, which varies from 0 and 6[4]. For example, semiconducting behavior is owing to completely filling of orbitals, while partial filling gives rise to a metallic behavior.

2.1.1 Phase-Property Relationship

The different transition metal coordination of TMDs result in two basic phases in monolayer TMDs—1H (hexagonal) with D_{3h} symmetry and 1T (trigonal) phase with D_{3d} symmetry, respectively. Furthermore, according to the different distortions, 1T phase can also be distorted as 1T′ and 1T″ phases[4]. In addition, different stacking orders of the 1H and 1T monolayer resulted in various phases in bulk TMDs materials. The most common phases are 2H, 1T, and 3R (rhombohedral), the digit indicates the number of layers in stacking. The 2H-TMD has an AbA BaB stacking sequence (The capital letters A and B represented for the atoms of chalcogen, while a and b represented metal atoms, respectively). The stacking sequence of 3R phase is AbA CaC BcB (same denotation as 2H phase). The preferred structure or phase in the ambient condition adopted by TMDs materials depends primarily on the d orbital electrons density of transition metal. The Group 4 (d_0) and Group 10 (d_6) TMDs only have octahedral structures, while Group 7 (d_3) TMDs mostly show distorted octahedral structures. Group 6 (d_2) TMDs typically show trigonal prismatic structure, while Group 5 (d_1) TMDs may have both octahedral and trigonal prismatic form. Taking the most commonly encountered Mo- and W-based TMDs as examples, MoS_2, WS_2, $MoSe_2$, WSe_2, and $MoTe_2$ prefer trigonal prismatic structure, which is the 2H phase in other words. While specifically, WTe_2 prefers 1T′ phase rather than 2H phase under ambient condition. Besides the thermodynamic stable phase, metastable phases have attracted tremendous attention during recent years. **Figure 2.2** listed the existing structural phase (either stable or metastable) and the corresponding electronic properties[4].

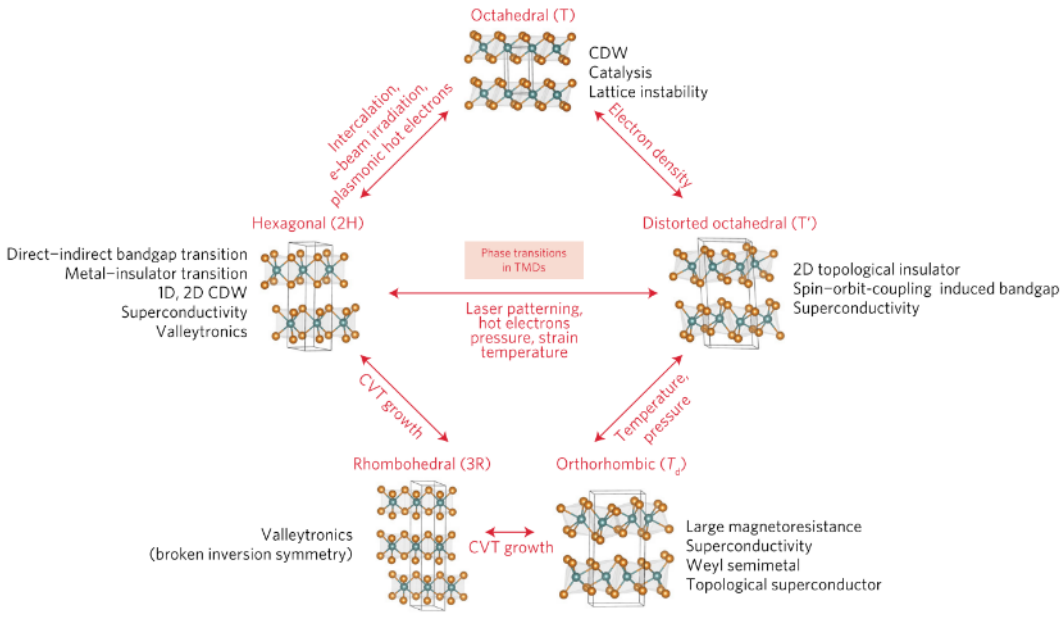

Figure 2.2 The phase and properties relationship in TMDs[4].

As listed in **Figure 2.2**, TMDs materials with different phases will exhibit different properties. For example, the most studied MoS_2 exhibited a stable 2H phase and the metastable 1T, 1T′ phase. Semiconducting 2H-MoS_2 showed a ~1 eV bandgap of while the 1T and 1T′ phase MoS_2 have metallic properties. The metastable 1T′-MoS_2 has a conductivity of 700-1000 S/m and a better charge transport capability which generates a much higher hydrogen evolution reaction performance than its 2H counterpart[5]. Another attractive TMDs materials are $MoTe_2$ with stable 2H, metastable 1T′, and T_d phases. Each metastable phase of $MoTe_2$ exhibits unique physical properties compared to the 2H one. The 1T′-$MoTe_2$ bulk crystals exhibit a 16,000% giant magnetoresistance within a 14 T magnetic field at 1.8 K as well as a maximum carrier mobility of 4,000 $cm^2\ V^{-1}\ s^{-1}$(REF[6]). In addition, the 1T′-$MoTe_2$ nanosheets (NSs) presented a 60 meV bandgap opening induced by strong interband spin-orbit coupling, according to the DFT calculations[7]. Besides that, the metastable T_d phase $MoTe_2$ could be considered as type-II Weyl semimetal which offering a great opportunity to further probe this new existing state through direct experimental observation[8]. Apart from well-studied Group 6 TMDs, $NbSe_2$ as a member of Group 5 TMDs gained intensive investigation due to the unusual physical behaviors. A

most recent research revealed that 1T monolayer $NbSe_2$ was a Mott insulator, with a 0.4 eV energy gap[9]. The diversity of TMDs structure, phases and the resulting versatile electronic properties give rise to numbers of applications such as catalysis, energy storage, chemical sensors, electronics and bio-related applications.

2.1.2 Preparation of 2D TMDs with metastable phase

The weak van der Waals (vdW) interaction between the TMDs layers allows the exfoliation down to few or monolayers. The as-exfoliated TMD NSs presented an ideal platform for fundamental research and the ultrathin device exploration. Upon decreasing the thickness, 2D TMDs display extraordinary electrical and optical properties which caused by surface effects and quantum confinement. What′s most noteworthy is the indirect to direct transition of bandgap as bulk TMDs materials exfoliated down to monolayers. For example, the calculated bandgap value of bulk 2H-MoS_2 is 0.88 eV while the monolayer 2H-MoS_2 has a bandgap of about 1.71 eV[3]. This indirect to direct transition of bandgap arises from the d-orbital interactions and the related quantum confinement effects[10]. Such behaviors are identified by the enhanced photoluminescence in a series of TMDs monolayers. While the few-layered counterparts of the above materials show only weak emission[10-12].

The tunable bandgap in 2D TMDs, strong photoluminescence (PL) enhancement along with the high exciton binding energy, opening up great possibility for the next-generation devices. As for now, single-layer 2H-MoS_2 has been utilized for phototransistor and other electronic or opto-electronic devices[12]. With excellent properties including good mobility, high on/off ratio, large optical absorption, direct bandgap, and the resulting giant PL enhancement, an extensive exploration of 2D MoS_2 based electronic/opto-electronic devices has been conducted. Phototransistors, light-emitting diodes, solar cells, and photo/electronic detectors based on 2D MoS_2 or other 2D TMDs are investigated at surprising speed[11].

In the meantime, the metastable phases of 2D TMDs have gained enormous attention due to the unusual and special physical properties such as superconducting, spin-orbit-coupling

behavior, unusual magnetism, ferroelectricity, and memristive behavior[13]. Besides, metastable 2D TMDs were also regarded as potential candidates for novel applications in the energy storage, catalysis, sensor, and devices area. The metallic 1T and 1T′ phase MoS_2 are found to be good supercapacitor electrode materials and electrocatalysts for HER. Field-effect transistors based on 1T-MoS_2 and 1T′-$MoTe_2$ were also fabricated and studied. In addition, 1T $NbSe_2$ monolayer was proved as Mott insulator which may offer an opportunity for precise device control.

Therefore, it is urgently needed to prepare the metastable 2D TMDs in high quality, large scale and high stability with largely preserve of the metastable phases. Traditionally, the ultrathin 2D TMDs materials are prepared by a large variety of methods. Bulk crystal exfoliation, solution-processed exfoliation or synthesis, chemical vapor deposition and intercalation have all been utilized. The main ideas of 2D TMDs exfoliation can be summarized into the following three strategies, that is the top-down exfoliation, bottom-up synthesis, and phase transition.

Strategy of Top-down Exfoliation

Mechanical exfoliation. The top-down exfoliation strategy can be divided into mechanical exfoliation and liquid-phase exfoliation method. Mechanical exfoliation is a traditional method to get monolayer or few-layered TMDs. In 2010, by using the mechanical exfoliation method, monolayer MoS_2 was prepared and studied, which stimulated the fast development of 2D TMDs materials[10,11]. High-quality MoS_2 NSs with different layers were first prepared and observed under the optical microscope and AFM as shown in **Figure 2.3**[10]. The as-exfoliated sample shows clean surface and few-layer structure. The layer number could be determined according to the color of optical images.

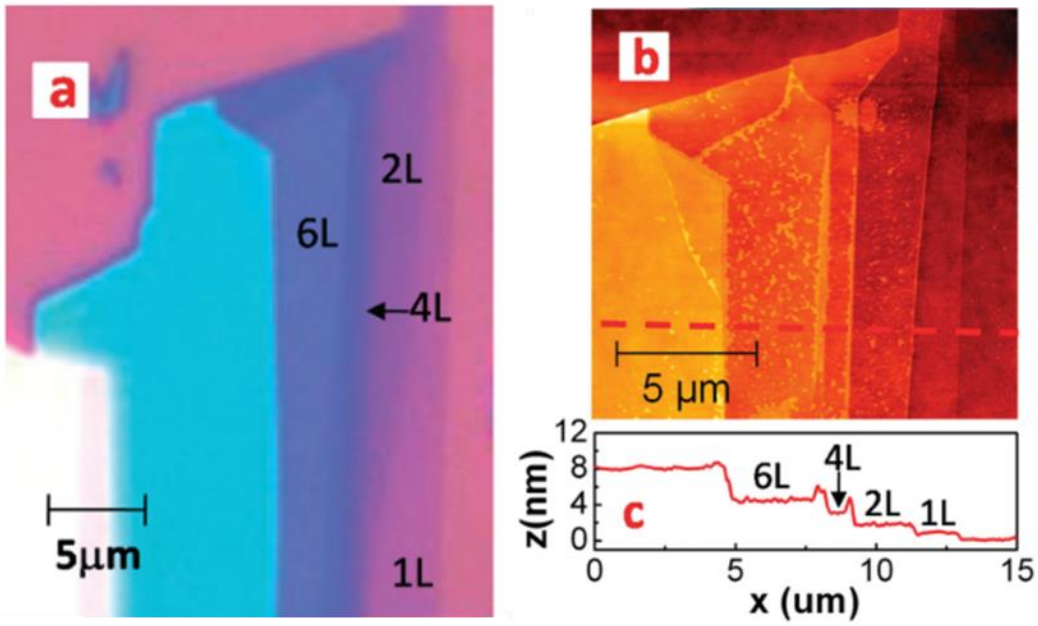

Figure 2.3 As-exfoliated MoS_2 NSs. **a**. Optical image of the MoS_2 NSs. The areas with different colors correspond to MoS_2 NSs with various layers, while the blue area indicates the substrate. Based on the contrast, the layer number of MoS_2 was labeled as "1L", "2L", "4L" and "6L" which represented for monolayer, bilayer, quadrilayer and hexalayer. **b**, AFM image of the same MoS_2 NSs. **c**, Thickness of the exfoliated sample along the red line in **Figure** b (REF[10]).

This method was then expanded to metastable TMDs for single sheets device fabrication and the later physical properties investigation. Keum, D. H. prepared the 1T′-$MoTe_2$ crystals, and get few-layered samples by using the mechanical exfoliation method[6]. A 60 meV bandgap opening was found in the 1T′-$MoTe_2$ few-layered NSs after exfoliation. Recently, Yu Yifu and co-workers used the mechanical exfoliation method to get few-layered 1T′-MoS_2 from the synthesized 1T′-MoS_2 crystals with high phase-purity[5]. High-quality electrochemical microcells were fabricated based on the as-exfoliated 1T′-MoS_2 NSs, a remarkable HER performance from the 1T′-MoS_2 basal plane was first observed and further studied. The mechanical exfoliation method can produce 2D TMDs materials with high preservation of the original phase or properties. But this method is also time-consuming and cannot produce metastable 2D TMDs in a large scale.

Liquid-phase exfoliation. The vdW gap of TMDs layered materials allows small molecules to intercalate inside. The liquid-phase exfoliation is to use suitable dispersion chemicals, such as solvent, inorganic salts, surfactants or reaction reagents, to intercalate inside the TMDs materials. The affinity between the selective chemical and host TMDs materials will then weaken the vdW interaction between layers. A wise selection of dispersion chemical is to get the highest exfoliation yield as well as preserve the quality of as-exfoliated NSs. As long as the van der Waals interaction is weakened sufficiently, the subsequent sonication or just mild shaking could easily isolate the TMDs NSs in the solvent.

Exfoliation of various layered materials can be accomplished using the different organic solvent as dispersion chemical combined with the subsequent sonication process[14]. The systematic experimental data suggested the 1-methyl-2-pyrrolidone (NMP) being the most efficient exfoliation solvent. However, the NMP is difficult to remove from the surface of TMDs NSs, which could be detrimental for device fabrication or other specific applications. And the toxicity further hinders it from being used in large-scale applications. To cope with this situation, researchers used the simple water-ethanol mixture as an effective solvent for TMDs exfoliation such as MoS_2 and WS_2[14]. Moreover, with the assistance of alkylamine, the as-exfoliated MoS_2 NSs could be well dispersed in many kinds of organic solvents, either polar or nonpolar, with high stability for months. Alkaline metal intercalation is one of the most important methods to prepare solution-processable TMD NSs. Eda and coworkers used n-butyllithium to intercalate lithium inside the layers, they can exfoliate bulk MoS_2 into single-layers with high yield[15]. Meanwhile, the lithium intercalation will induce the phase transition and get the MoS_2 with 2H phase, 1T, and distorted 1T′ mixed-phase as shown in **Figure 2.4**[16]. **Figure 2.4** shows that the 1T phase is predominantly in the chemical exfoliated MoS_2 monolayers. In addition, the high inhomogeneity nature of the sample which is composed of nanometer-sized domains of different phases is clearly observed. The 1T WS_2 monolayer was also prepared by this intercalation method. The as-prepared sample exhibited enhanced HER performance which is ascribed to the high density 1T metallic phase[17]. Even though the chemical exfoliation by using butyllithium is proved to be an effective way to get single-layer metastable TMDs with large scale, the

strict operating conditions and long intercalation time (3 days) were required, let alone the uncontrollable lithium intercalation amount.

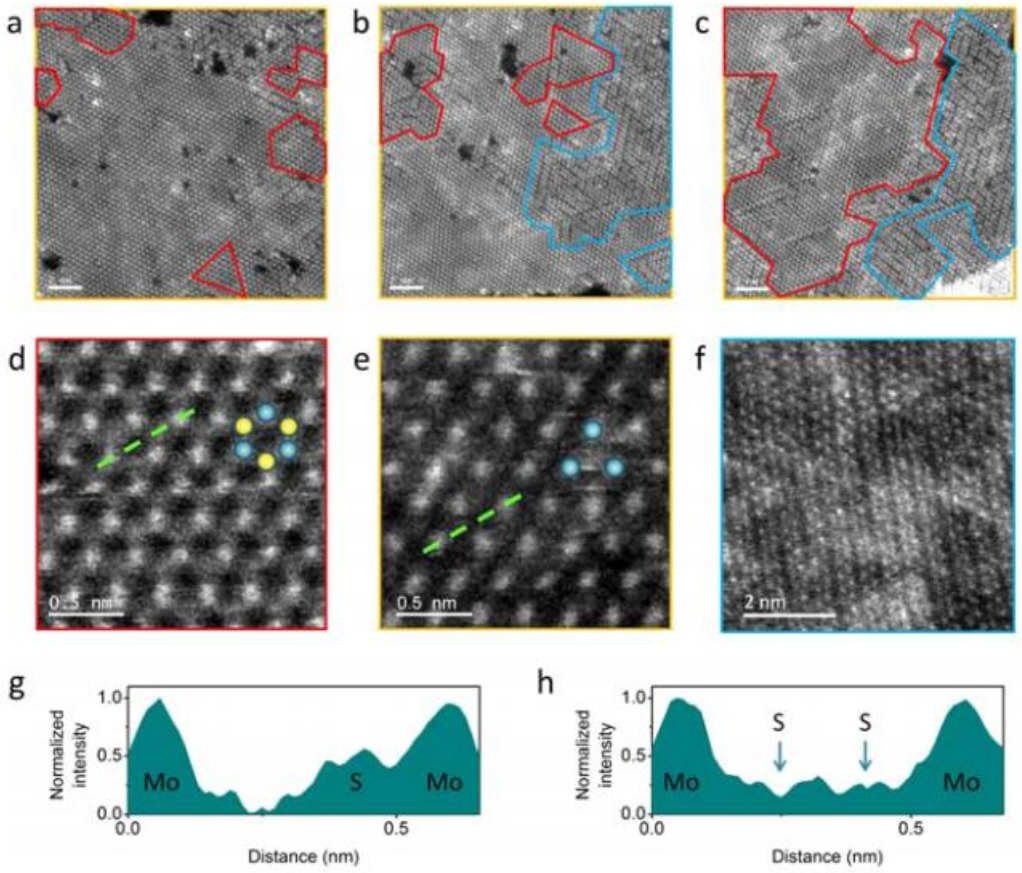

Figure 2.4 a-c, STEM images of single-layer MoS_2 in a different region with yellow line enclosed 1T region, while blue and red lines included 1T′ and 2H phase. The scale bar is 2 nm. **d-f**, High resolution STEM images of the as-exfoliated single-layer MoS_2 in **d**, 2H, **e**, 1T, and **f**, 1T′ phase region. The Mo and S atom position are indicated with blue and yellow balls. **g**, **h**, Signal intensity along the lines showed 2H phase (**d**) 1T phase (**e**)[16].

While then, Zeng and coworkers developed the electrochemical lithium intercalation method to get the metastable 2D TMDs[18]. The experiments were conducted in a battery system, which is illustrated in **Figure 2.5**. The Li^+ ions were inserted into the MoS_2 layers through a controllable galvanic discharge process in the lithium battery system. The Li^+

ions amount during intercalation can be precisely controlled and monitored within the battery system. After the ultrasonication and purification process, well-dispersed single-layer MoS_2 with extremely high yields of 92% is prepared. Similar to the butyllithium intercalation method, the as-prepared MoS_2 shows a high concentration of 1T phase. This method has also been expanded to the exfoliation of WS_2, TiS_2, TaS_2, ZrS_2 with high yields and high quality.

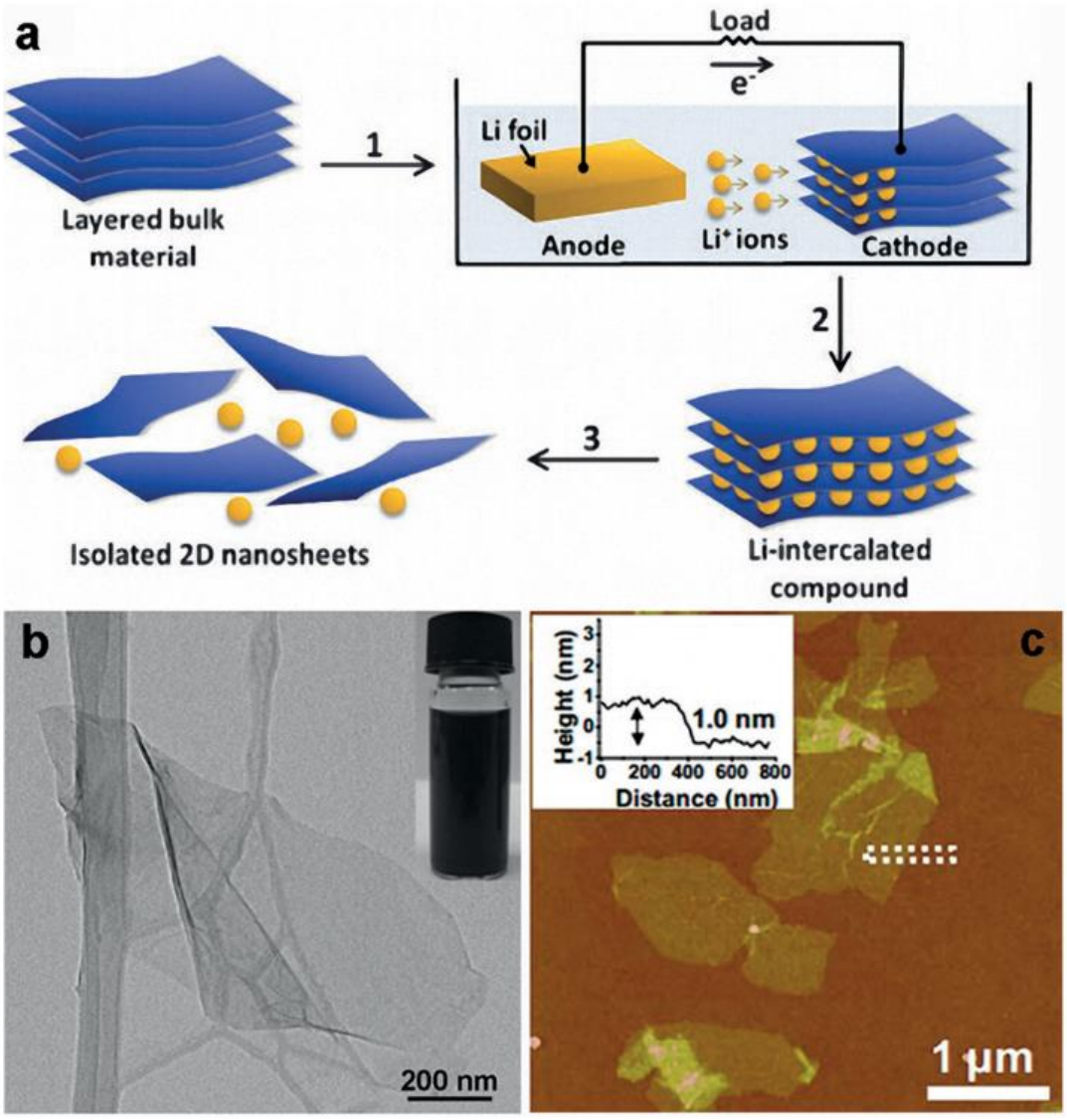

Figure 2.5 a, Scheme of the electrochemical exfoliation process. **b**, TEM image of the as-exfoliated MoS_2 monolayer. **c**, AFM image of as-prepared MoS_2 monolayer. Inset in **b** showed a snapshot of MoS_2 solution. Inset in **c** showed height distribution of the same MoS_2 monolayers[18].

Although the lithium intercalation method effectively produced the single or few-layer TMD NSs with the high percentage of metastable 1T phase, the mixed-phase nature within the as-prepared TMD NSs makes it impossible to further study the pure 1T phase properties. Lin and coworkers reported a general solution-processable approach to prepare phase-pure TMDs NSs with high uniformity[19]. The whole process included the intercalation of tetraheptylammonium bromide (THAB) molecules into 2D TMDs crystals during an electrochemical process, followed by a mild sonication process. The large size nature of THAB (about 20 Å in diameter) limits electrons injection, which is only 0.02 electrons for each MoS_2 formula unit. Such a limited electron donation which is much lower than the phase transition threshold (0.29 e^- per MoS_2 formula unit) will prefer maintaining the original phase of the TMDs materials after exfoliation. The main drawback of this method is that the raw materials have to be large size bulk crystals which impede the extensive application in powder materials.

In conclusion, a top-down exfoliation strategy can produce any kind of 2D TMDs materials as long as the bulk materials are existed or can be synthesized. The mechanical method is suitable for preparing metastable 2D TMDs with high quality towards microelectronic. Liquid-phase exfoliation is suitable for large scale preparation, but the original phase or structure of the metastable TMDs crystals are hard to preserve during the sonication, intercalation in the whole process. Therefore, it is necessary to find a balanced method with high yield as well as the phase preservation to promote the further exploration of metastable 2D TMDs materials.

Strategy of Bottom-up Synthesis

The bottom-up strategy is to synthesis the metastable 2D TMDs directly from transition metal sources and chalcogen precursors. Significant efforts have been devoted to the bottom-up synthesis with large scale, controllable thickness and wafer-scale uniformity

including chemical vapor deposition (CVD) and other direct deposition methods, such as wet chemical method, sputtering, and electron beam method[20].

Chemical vapor deposition (CVD). CVD is one of the most effective methods that generate TMDs layers with high-quality, controllable thickness, large size, and extraordinary electronic properties. However, the direct growth of metastable 2D TMDs remains a huge challenge. That is due to the higher formation energy compare with their stable counterpart, which will form the stable 2D TMDs NSs instead of the metastable one. Therefore, it is of great necessity to develop a new and controllable strategy for CVD growth of metastable 2D TMDs. In 2017, Empante and coworkers used the MoO_3 and Te powders as precursor to prepare few-layer films of $MoTe_2$(REF[21]). By controlling the growth quench temperature of less than 100 ^oC, 350 ^oC, and 450 ^oC, three distinct structural phases of 2H, 1T′, and 1T-$MoTe_2$ can be prepared respectively. In addition, Zhang and coworkers used iodine-mediated CVD method to grow the 1T′-$MoTe_2$ flakes[22]. The researchers used SiO_2-covered silicon as the substrate, and all the reactants were placed in a CVD furnace. It was heated to 700 °C and held for 80 min in an atmosphere of Argon and Hydrogen. The as-prepared sample can be seen in the optical images with micrometer size and ribbon-like shape. The Raman spectra show the 1T′ peaks, the AFM images show the 1 nm uniform height suggesting this part of the sample is monolayer. The thickness distribution is shown here, indicates the sample is few-layered. And the Raman mapping of the B_g and A_g peak intensity confirmed the uniformity of the 1T′ phase. TEM, SAED images show the 1T′-$MoTe_2$ atomic structure of, that is the zigzag morphology of Mo atoms. The distances between two continuous Mo atoms along the yellow and blue lines are also be shown. In this work, the iodine served as a catalyst which can lower the 1T′-2H phase energy barrier and make the phase transition process much easier.

In 2018, for the first time, Liu and coworkers realized the direct synthesis of high phase-purity, highly crystallinity metastable 1T′-MoS_2 monolayers through one-step CVD growth method[23]. The introduction of potassium is the key point to successful growth. Through theoretical calculation, the introduction of potassium is capable of decreasing the formation energy of the 1T′ phase MoS_2 favors the formation of 1T′ phase instead of the 2H-MoS_2.

Moreover, pure 2H phase monolayers and 1T′/2H heterophase bilayers of MoS_2 were also obtained by altering preparation parameters. Raman, XPS and atomically resolved filtered STEM were used to characterize the structure of the monolayer 2H-and 1T′-MoS_2 as shown in Figure 2.7.

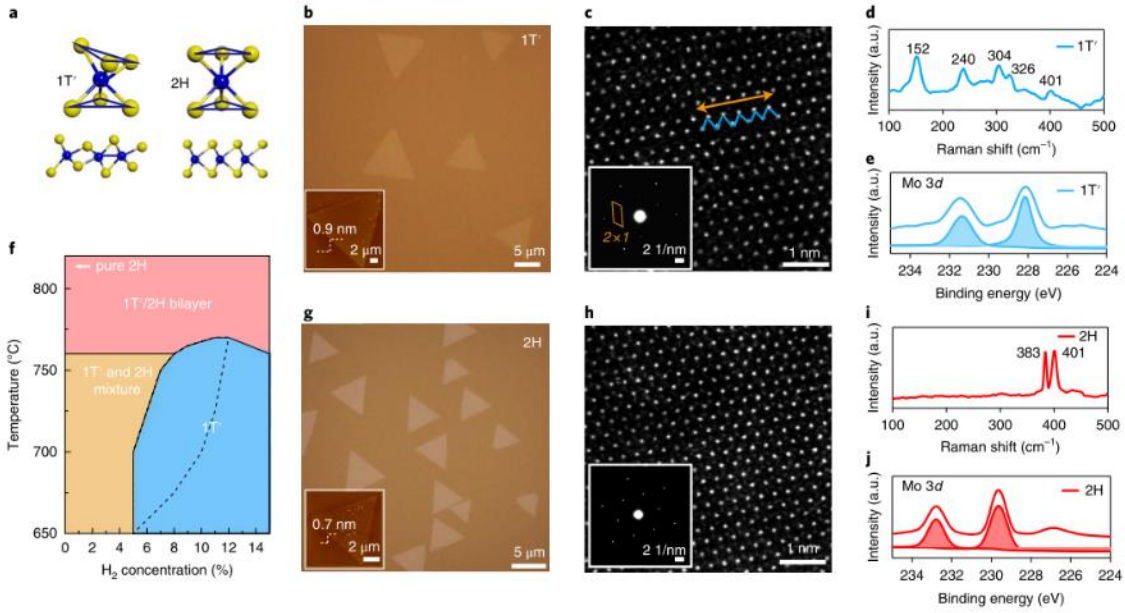

Figure 2.6 As-grown of 1T′ and 2H-MoS_2 monolayers. **a**, Schematic illustration the 1T′, 2H phase MoS_2 structures. Optical images of 1T′ and 2H-MoS_2 monolayer triangular flakes are shown in (**b**) and (**g**). Insets are the AFM images of (inset in **b**) 1T′ and (inset in **b**) 2H-MoS_2 monolayers. (**c**) 1T′ and (**g**) 2H-MoS_2 monolayers STEM images, respectively. Insets are the SAED patterns of (inset in **c**)1T′ phase and (inset in h)2H phase MoS_2 NSs, respectively. Raman spectra of (**d**) 1T′ phase and (**i**) 2H phase MoS_2 monolayers. XPS spectra of (**e**) 1T′ and (**j**) 2H-MoS_2 monolayers of Mo 3d orbits. **f**, Phase diagram influenced by H_2 concentration and reaction temperature in the growth process of MoS_2 (REF[23]).

Other methods. Besides CVD growth other methods such have also been conducted to prepare the metastable 2D TMDs. Nakata and the co-workers used the molecular-beam epitaxy combing with the electron spectroscopy methods, the selective fabrication of 1T and 2H single-phase $NbSe_2$ monolayer was realized for the first time[9]. Bilayer graphene was firstly prepared on a single-crystal silicon wafer to act as a template. The evaporation

of Nb was then conducted on the bilayer graphene in a Se atmosphere within a high vacuum. The sample along with the substrate was then transferred directly into angle-resolved photoemission spectroscopy (ARPES)-measurement chamber within the vacuum condition for further characterization.

The wet chemical method is also an effective method to obtain metastable TMDs. Sun and coworkers used the hot injection method preparing the 1T′-$MoTe_2$[24]. The possibility to access metastable TMDs phase by a simple wet-chemical method offering an opportunity to high yields preparation of metastable 2D TMDs. Liu and coworkers used a templated growth strategy to synthesize 1T′-MoS_2 and $MoSe_2$ monolayers[25]. In a colloidal system, 1T′-MoS_2 and $MoSe_2$ monolayers with high-concentration metallic phase were grown successfully on the Au nanorod with 4H/face-centered cubic (fcc) structure and form the nanocomposite of 4H/fcc-Au@MoX_2.

In conclusion, the fast development of bottom-up synthesis method, especially the CVD growth method, make it possible to prepare all kinds of 2D TMDs from their transition metal and chalcogen precursor. Although the higher formation energy metastable phase TMDs monolayer hampered the direct growth, various kinds of metastable 2D TMDs have been successfully obtained by the carefully designed bottom-up synthesis strategy. Based on these inspiring progresses, further developing CVD growth and other bottom-up synthesis methods with high controllability, large scale, and high quality could be a promising way to obtain metastable 2D TMDs materials.

Strategy of Phase Transition

Phase transition is another accessible way to obtained metastable 2D TMDs materials. The TMDs phases exhibit a strong dependence on the d orbital electron density of transition metal. Therefore, phase transitions could be induced by changing electron structures of the 2D TMDs materials, including intercalation, electron doping, high energy irradiation, mechanical force, thermal treatment, and other methods.

Intercalation. The most common intercalation method to get metastable 2D TMDs is the lithium intercalation. As mentioned above, the chemical or electrochemical lithium intercalation method will exfoliate the TMDs bulk into 2D NSs while simultaneously induce 2H to 1T phase transition[10,18]. This method was soon expanded to other kinds of alkali metals and small molecules. In 2014, Wang and coworkers reported an electrochemical method to intercalate controlled amount of Na ions into MoS_2 layers while in situ and ex situ monitored the phase transition[26]. In 2016, Zhang and coworkers demonstrated that potassium intercalation in MoS_2 will facilitate 2H to 1T and 1T′ phase transition while simultaneously induce the superconductivity in such metallic phases[27]. The relationship between intercalated potassium amount and the phase transition process is studied in detail. A complete phase transition will only occur when the K intercalation amount is about 12 atom% (corresponding to $x = 0.4$ in K_xMoS_2 formula). As the K atomic ratio increased from 12% to 25%, MoS_2 continuously changed from 2H to 1T phase. When the potassium increased to more than 25%, 1T′ phase MoS_2 begin to replace the 1T-MoS_2. The ammonia intercalation was also used to obtain and stable the metallic 1T WS_2 nanoribbons[28]. During the intercalation, every NH_4 transferred about 0.75 electrons to WS_2 layer thus formed the $WS_2^{-}\cdot NH_4^{+}$ ionic complex. The strong interaction of NH_4 with the WS_2 layers will stabilize the metastable metallic phase.

Electron doping. The electron could be transferred into TMDs from an external electrical field or the contact interface. Wang and co-workers realized the reversible electrostatic-doping-driven phase transition in $MoTe_2$[29]. The reversible 2H to 1T′ phase transition of $MoTe_2$ can be achieved in a gate device by gate voltage increasing or decreasing without damage the sample. The electron transfer from some highly charged materials through the contact interface was also proved to be an effective way of electron doping. Kim and co-workers reported a long distance (over 100 nm) electron transfer from the 2D electride to $MoTe_2$ on interface and induced a structure change of $MoTe_2$ from hexagonal 2H-$MoTe_2$ to the monoclinic 1T′-$MoTe_2$[30]. The selective electride $[Ca_2N]^{+}\cdot e^{-}$ is highly crystalline with a low work function of 2.6 eV and highly mobile anionic electron layers. As the 2D electride $[Ca_2N]^{+}\cdot e^{-}$ is placed in contact with the target materials 2D $MoTe_2$, the generated

unusually high electron transfer from the 2D electride to $MoTe_2$ facilitated the 2H to 1T′ phase transition.

High energy irradiation. High energy irradiation including plasma, electron beam and laser will also induce the 2D TMDs phase transition. Zhu and co-workers reported Ar-plasma treatment induced phase transition method which can locally induce phase transition from 2H to 1T in MoS_2 single layer[31]. After the 40 s treatment, more than 40% MoS_2 metallic 1T phase was formed. By introducing the selected-area plasma patterning process, the MoS_2 FETs with different phase domains can be fabricated. In more details, such FETs were fabricated by standard process in sequence as shown in **Figure** 2.7.

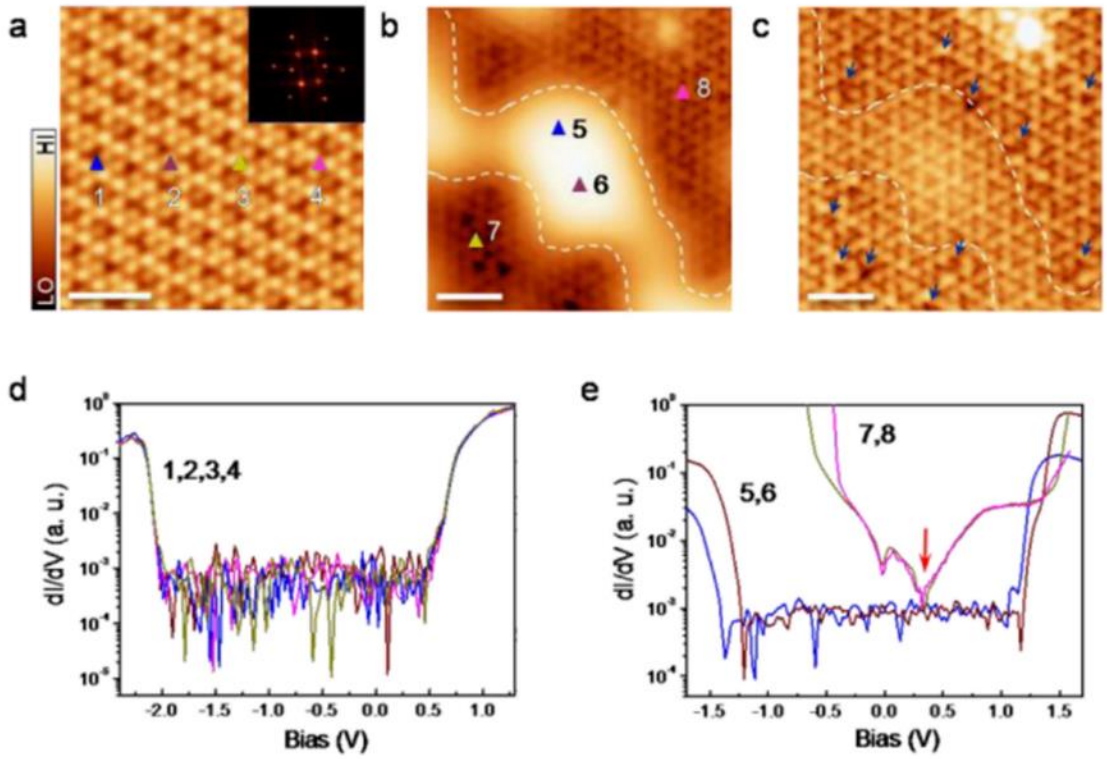

Figure 2.7 a-c HRSTM images of MoS_2 monolayer grown on graphite (**a**) before and (**b, c**) after plasma radiation. Inset in (**a**) showed the FFT pattern of panel a, where larger set of hexagonal patterns are the top S atoms of MoS_2, and the smaller one corresponds to the Moiré pattern. **d**, Schematics of three types of devices. **e,** Schematic illustration of the 1T-MoS2 contacted device fabrication process[31].

Lin and co-workers introduced the electron-beam induced phase transition on a MoS_2 monolayer[32]. After electron-beam continuous treatment, the 1T phase domain occurred and enlarged into a triangular shape area of around 8.5 nm^2. As the phase transformation only took place at the electron beam scanned area, the electron beam irradiation can be applied intentionally to obtain a pattern of different phases with predetermined size toward specific nanoelectronic devices. Phase transition can also be achieved by laser irradiation. Cho and co-workers fabricated an ohmic homojunction contact in $MoTe_2$ monolayer by using laser-induced phase patterning method. The as-fabricated 2H/1T′-$MoTe_2$ hetero-phase homojunction is stable even at 300°C, which is compatible with almost all the manufacturing processes of semiconductor.

Mechanical force. The crystal structure of TMDs can be altered by mechanical force providing another phase transition strategy. Strain can induce the phase transformation in 2D TMDs. Nayak and co-workers used the high-pressure diamond anvil cell (DAC) to apply high pressure on the multilayered single-crystal MoS_2 (REF[33]). The experimental results reveal that the sample undergoes a transition from semiconductor to metal at about 19 GPa. Due to the calculation in this work the origin of metallic electronic states is the sulfur-sulfur interaction as the van de Waals′s gap closed under high pressure. The mechanically induced phase transition phenomenon indicates a promising way towards the construction of multi-functional devices towards various applications based on the 2D TMDs materials with tunable phase.

In conclusion, the controlled and locally phase transition in 2D TMDs materials can be achieved by electron doping, external irradiation and mechanical force. Hetero-phase TMDs structure with stable phase and metastable phase coexisted is easily obtained by the phase transition method which enables the fabrication of high-quality homojunction towards nanoelectronics.

2.2 Incorporating metastable TMDs with noble metal nanostructures

2D TMD have attracted tremendous interests due to great potential in electrocatalysis, electronics, and energy storage applications. Especially, the TMD materials were regarded as the promising low-cost electrocatalysts for HER to replace the noble metal Pt. However, the HER activity of the TMD materials does not as high as the commercial Pt or Pt based materials. Incorporating 2D TMD with metals, metal oxides, metal sulfides, and many other materials, is an effective way to towards the high HER performance. Traditionally, the design and controlled synthesis of 2D TMD-based hybrid nanomaterials mainly focused on fine-tuning the composition, morphology, size, dimensionality, and other structural parameters. The emerging phase engineering strategy of nanomaterials has demonstrated that tailoring the phase of the TMD substrate could be an effective strategy to modulate the structure and properties of TMD-based hybrid materials towards promising applications. TMD materials have various stable or metastable phases, such as the 2H, 1T, 1T′, Td and 3R phases. Each phase has its own unique properties. For example, the 2H-MoS_2 exhibited a semiconducting property while 1T or 1T′-MoS_2 exhibited a metallic property. Such a high conductivity endows 1T or 1T′-MoS_2 with lower charge transfer resistance. In addition, 1T and 1T′-MoS_2 have an electrochemical active basal plane, the in-plane sulfur also acts as active sites. Therefore, when compared with the 2H-MoS_2, the 1T and 1T′-MoS_2 exhibit superior electrochemical performance.

Based on this, various 1T or 1T′-MoS_2-based hybrid nanomaterials have been prepared with compelling structure and enhanced performance as compared with the conventional 2H-MoS_2-based hybrids, especially for electrocatalytic hydrogen evolution reaction (HER). Previous, Huang and coworkers reported the epitaxial growth of noble metals Pt, Pd, and Ag on 1T-MoS_2 substrate[34], the Pt-MoS_2 materials exhibited a high HER activity as shown in Figure 2.8. The 1T-MoS_2 NSs are prepared by the traditional Li-intercalation method. As we can see from the XPS spectrum, such method resulted in a coexistence of 1T and 2H phase.

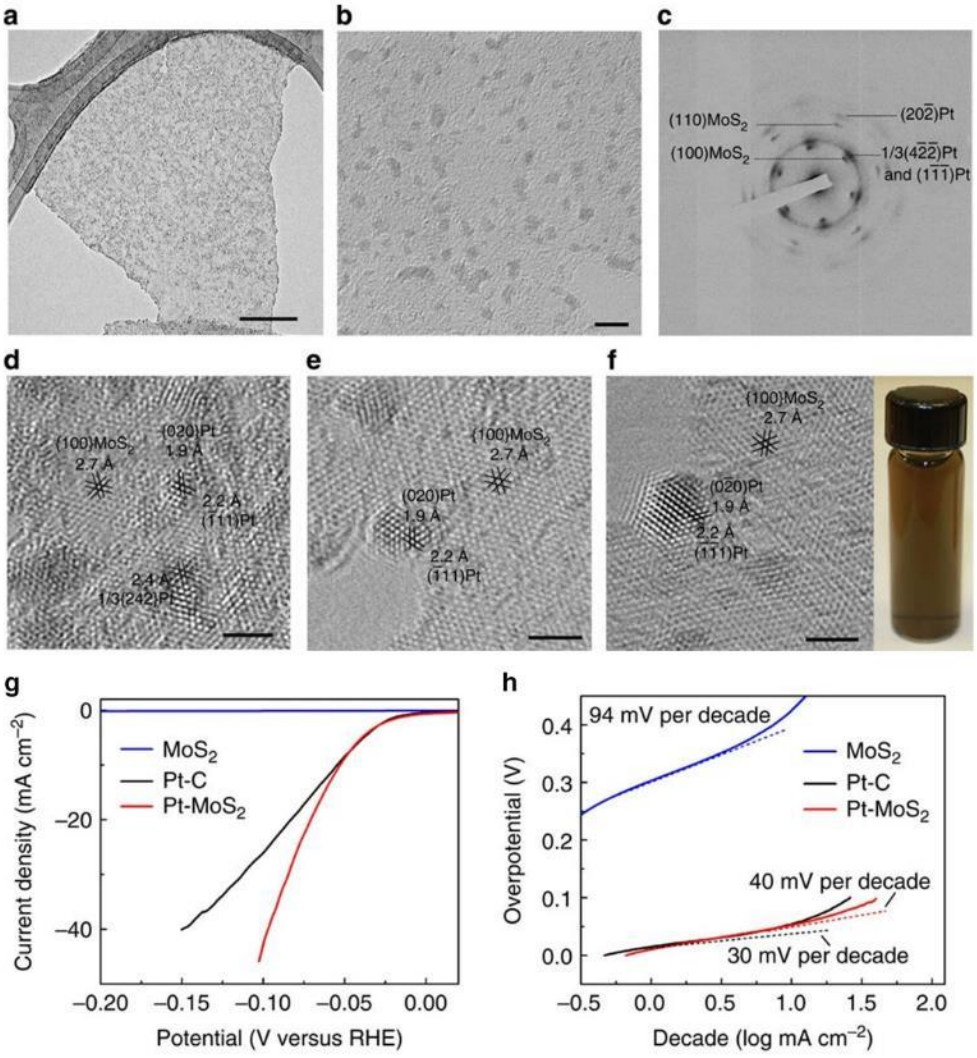

Figure 2.8 Structure and application analysis of Pt-MoS_2 hybrid nanomaterials. **a**, TEM image (scale bar, 100 nm) and **b**, magnified TEM image (scale bar, 5 nm) of Pt NPs synthesized on a MoS_2 nanosheet. **c**, the corresponding SAED pattern of a Pt-MoS_2 hybrid structure. **d-f**, HRTEM image showed distinguishable lattice fringes for Pt and MoS_2 of the Pt-MoS_2 hybrid (scale bar, 2 nm). Inset in f, the photograph of the Pt-MoS_2 solution. **g-h**, Polarization curves (**g**), and the corresponding Tafel plots (**h**) of Pt-MoS_2, Pt/C, and MoS_2 NSs, respectively[34].

Recently, the 1T-Phase MoS_2−Pd/Au hybrid nanomaterials have been prepared[35]. The researched used a hydrothermal method to prepare the 2H-MoS_2, and incorporated it with the Au-Pd heterostructure, and form a 1T-MoS_2-Au/Pd hybrid nanomaterials[35]. The lattice

mismatch between Pd and 2H-MoS_2 to facilitate the 2H to 1T phase transition. The obtained SSN-Au/Pd-MoS_2 exhibited superior photocatalytic hydrogen evolution performance light illumination. However, this method can only induce the formation of 1T-MoS_2 which is directly under the Au/Pd structure. Other places which are free from the Pd-Au structure still remain the 2H phase. As we can see from the Raman spectra, there still exited the 2H characterized Peaks. In 2018, researchers used the lithium intercalated method to get the 1T-MoS_2 substrate and incorporated it with Pd atoms as shown in Figure 2.9 (REF[36]). Pd atoms replace the Mo atoms and incorporated inside the 1T-MoS_2 lattice, covalently bonded with the surrounding S atoms and induce the phase transition. Such Pd incorporation strongly activates the neighboring S sites with high HER activity. The Pd-MoS_2 catalyst possesses a superior activity towards the HER with an overpotential of only 78 $mVcm^{-2}$ at 10 $mAcm^{-2}$. Impressively, the Pd-MoS_2 with a large amount of defects possesses a high stability. The Ir/1T-MoS_2 heterostructures are also reported for HER, OER, and the overall water splitting with high performance[37]. Researchers found that by incorporating the 2H-MoS_2 and Ir particles, the phase transition from 2H to 1T is induced and get an Ir/1T-MoS_2. When the Ir ratio is increased, the MoS_2 substrate transfer from the 2H to 1T phase.

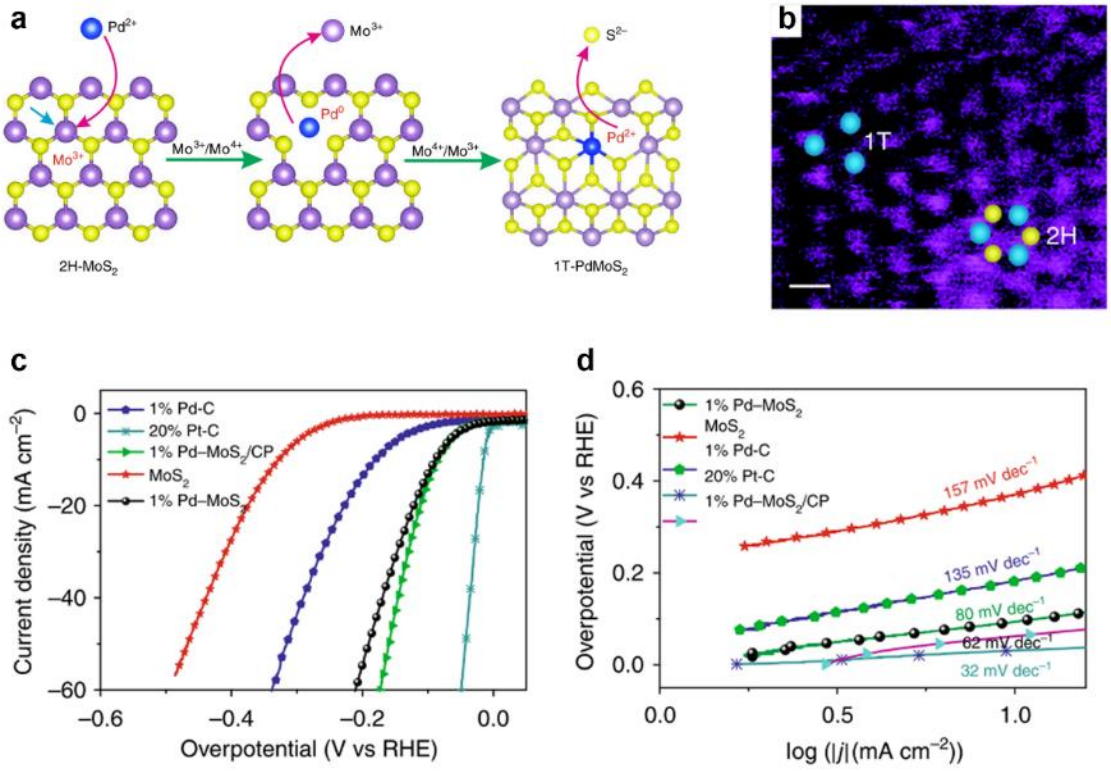

Figure 2.9 a, Scheme shows the Pd doping process. **b**, Dark-field STEM image of the 1% Pd-MoS_2. Blue balls represent for Mo and the yellow balls are S atoms, respectively. Scale bar: 1 nm. **c**, LSV curves and the **d**, Tafel plots of samples[36].

Besides the noble metal, the non-noble metal is also introduced in MoS_2 to form a hybrid nanomaterial. By using a solvothermal method, the Cu atoms and Co single atoms are introduced inside the MoS_2 materials, to form Cu-1T-MoS_2 and Co-1T′-MoS_2 materials with enhanced HER performance[38]. Another example is the amorphous Ni-Co complexes and 1T-MoS_2 hybrids[39]. N_2H_4 was used to induce the phase transition. In summary, various 1T or 1T′-based MoS_2 are reported with enhanced HER performance showing that incorporating noble metal with unconventional phase MoS_2 pave an effective way to develop novel electrocatalysts.

2.3 Questions to Answer Based on Literature

As discussed in the previous section, tremendous effort has been devoted to preparing the novel structured TMDs nanomaterials due to their unique physicochemical properties and great potential in various promising applications. Till now, various methods such as alkali-ion intercalation method, external irradiation method, strain and pressure-induced phase transition method and the hydrothermal synthesis method, etc, has been utilized to prepare novel structured TMDs nanomaterials. Furthermore, diverse components such as noble metal, non-noble metal, etc have been incorporated with the obtained metastable 2D TMDs, such as 1T and 1T′-MoS_2 to prepared metastable 2D TMDs-based electrocatalysts. Such electrocatalysts exhibited much superior HER performance not only better than the traditional 2H-MoS_2-based electrocatalysts but also approaches the Pt or Pt-based electrocatalysts.

However, great challenges lie in this area and remain unresolved. First and foremost is the phase purity issue. Enormous efforts have been put in developing new synthesis or exfoliation strategies with high quality and excellent efficiency. Metastable 2D TMDs can either prepared by mechanical and liquid phase exfoliation method from bulk crystals; or directly synthesized by wet-chemical, CVD, and MBE methods from metal and chalcogen precursor. In addition, phase transition induced by electron doping, external irradiation and mechanical force is also proved to be a controllable, effective method to obtain specific phase pattern of TMDs. However, such a variety of methods are varying in efficiency, controllability, and phase purity. For example, the chemical or electrochemical lithium intercalation method enables researchers to prepare MoS_2 NSs with high controllability and efficiency. But the as-prepared MoS_2 NSs exhibited a high phase impurity with 1T, 1T′, and 2H phase coexisted[16,18]. While the mechanical exfoliation and CVD grown methods exhibited high phase purity and low efficiency. Previous reported 1T or 1T′-MoS_2 substrate obtained from traditional phase transition method contains a certain portion of 2H phase. The ultralow conductivity of 2H-MoS_2 largely reduced the overall conductivity of the 1T or 1T′-MoS_2 substrate. In addition, the existence of 2H phase introduced numerous defects such as dislocation at phase boundaries, vacancies which greatly retarded

the electron transfer rate. Owing to these, the potential of 1T or 1T′-MoS_2 using as electrocatalysts substrate is greatly suppressed, the 1T or 1T′-MoS_2-based electrocatalysts resulted in a limited HER performance.

Secondly, the role of crystal phases in controlling the structure and properties of MoS_2-based hybrids is rarely discussed. Metastable 2D TMDs exhibit unusual structures and brand-new properties, which could serve as an ideal platform towards both fundamental research and practical application. However, due to the existence of 2H-MoS_2 in the obtained 1T or 1T′-MoS_2, little is known about the intrinsic properties of the metastable 1T or 1T′ phase materials. In addition, when incorporating with noble metal or other components, the growth of the second deposited materials cannot be precisely controlled due to the coexistence of several crystal phases and the resulted large numerous defects. In these circumstances, the role of the crystal phase in directing the growth of second deposited materials is unable to investigate.

2.4 PhD in Context of Literature

In my thesis, I focus on developing a new method to prepare metastable TMDs NSs and then exploring the electrocatalytic performance. Based on that, noble metal nanostructures are grown in situ on the TMDs NSs, the obtained hybrid nanomaterials exhibited superior electrocatalytic performance. The contribution of my thesis in this area is list as follow:

First, we report the preparation of 1T′-MoS_2 NSs by an organic molecule assisted electrochemical exfoliation method. By careful characterization, the as-prepared 1T′-MoS_2 NSs exhibited high phase purity, high crystallinity, and ultrathin thickness. It is also found that the obtained 1T′-MoS_2 NSs exhibited superior HER activity as compared with 2H-MoS_2 NSs prepared by the same method showing great potential to be used as electrocatalysts substrate. In addition, the developed electrochemical exfoliation method is also suitable to the preparation of other metastable TMDs NSs such as 1T′-$MoSe_2$ and 1T′-MoSSe NSs. Besides, other kinds of layered materials can also be prepared by such method.

Second, we report the epitaxial growth of noble metal nanostructures on 1T′- and 2H-MoS_2 substrate. Due to the large lattice mismatch and different symmetry, only small Pt clusters with non-crystallinity structure are grown epitaxial on the 1T′-MoS_2 NSs. On the contrary, big Pt particles are epitaxially grown on the 2H-MoS_2 NSs with clear lattice. In addition, Pt/1T′-MoS_2 hybrid nanomaterials showed excellent activity outperforming the commercial 10 wt% Pt/C for electrocatalytic hydrogen evolution reaction in acid electrolyte reaching 50 mA cm^{-2} current density and $11.3S^{-1}$ turn over frequency at only 30 mV overpotential, with a Tafel slope of 28.3 mV dec^{-1}. The durability of Pt/1T′-MoS_2 is also tested. After 40 hours HER test, the Pt/1T′-MoS_2 exhibited no degradation for HER. The Pt clusters and the 1T′ phase of MoS_2 remain unchanged according to the careful characterization.

References

1 Novoselov, K. S. Electric Field Effect in Atomically Thin Carbon Films. *Science* **306**, 666-669 (2004).

2 Chhowalla, M. *et al.* The chemistry of two-dimensional layered transition metal dichalcogenide nanosheets. *Nat. Chem.* **5**, 263-275 (2013).

3 Manzeli, S., Ovchinnikov, D., Pasquier, D., Yazyev, O. V. & Kis, A. 2D transition metal dichalcogenides. *Nature Reviews Materials*, **2**, 17033 (2017).

4 Yang, H., Kim, S. W., Chhowalla, M. & Lee, Y. H. Structural and quantum-state phase transition in van der Waals layered materials. *Nat. Phys.* **13**, 931-937 (2017).

5 Yu, Y. *et al.* High phase-purity 1T'-MoS_2- and 1T'-$MoSe_2$-layered crystals. *Nat. Chem.* **10**, 638-643 (2018).

6 Keum, D. H. *et al.* Bandgap opening in few-layered monoclinic $MoTe_2$. *Nat. Phys.* **11**, 482-486 (2015).

7 Zhang, C. *et al.* Charge Mediated Reversible Metal-Insulator Transition in Monolayer $MoTe_2$ and $W_xMo_{1-x}Te_2$ Alloy. *ACS Nano* **10**, 7370-7375 (2016).

8 Deng, K. *et al.* Experimental observation of topological Fermi arcs in type-II Weyl semimetal $MoTe_2$. *Nat. Phys.* **12**, 1105-1110 (2016).

9 Nakata, Y. *et al.* Monolayer 1 T-$NbSe_2$ as a Mott insulator. *NPG Asia Materials* **8**, e321 (2016).

10 Splendiani, A. *et al.* Emerging photoluminescence in monolayer MoS_2. *Nano Lett.* **10**, 1271-1275 (2010).

11 Mak, K. F., Lee, C., Hone, J., Shan, J. & Heinz, T. F. Atomically thin MoS_2: A new direct-gap semiconductor. *Phys. Rev. Lett.* **105**, 136805 (2010).

12 Yin, Z. *et al.* Single-Layer MoS_2 Phototransistors. *ACS Nano* **6**, 74-80 (2012).

13 Cheng, P., Sun, K. & Hu, Y. H. Memristive Behavior and Ideal Memristor of 1T Phase MoS_2 Nanosheets. *Nano Lett.* **16**, 572-576 (2016).

14 Zhou, K. G., Mao, N. N., Wang, H. X., Peng, Y. & Zhang, H. L. A mixed-solvent strategy for efficient exfoliation of inorganic graphene analogues. *Angew. Chem. Int. Ed.* **50**, 10839-10842 (2011).

15 Eda, G. *et al.* Photoluminescence from chemically exfoliated MoS_2. *Nano Lett.* **11**, 5111-5116 (2011).

16 Eda, G. *et al.* Coherent atomic and electronic heterostructures of single-layer MoS_2. *ACS Nano* **6**, 7311-7317 (2012).

17 Voiry, D. *et al.* Enhanced catalytic activity in strained chemically exfoliated WS_2 nanosheets for hydrogen evolution. *Nat. Mater.* **12**, 850-855 (2013).

18 Zeng, Z. *et al.* Single-layer semiconducting nanosheets: High-yield preparation and device fabrication. *Angew. Chem. Int. Ed. Engl.* **50**, 11093-11097 (2011).

19 Lin, Z. *et al.* Solution-processable 2D semiconductors for high-performance large-area electronics. *Nature*, 2018, **562**, 254-258.

20 Choi, W. *et al.* Recent development of two-dimensional transition metal dichalcogenides and their applications. *Mater. Today* **20**, 116-130 (2017).

21 Empante, T. A. *et al.* Chemical Vapor Deposition Growth of Few-Layer $MoTe_2$ in the 2H, 1T′, and 1T Phases: Tunable Properties of $MoTe_2$ Films. *ACS Nano* **11**, 900-905 (2017).

22 Zhang, Q. *et al.* Iodine-Mediated Chemical Vapor Deposition Growth of Metastable Transition Metal Dichalcogenides. *Chem. Mater.* **29**, 4641-4644 (2017).

23 Liu, L. *et al.* Phase-selective synthesis of 1T′ MoS_2 monolayers and heterophase bilayers. *Nat. Mater.* **17**, 1108-1114 (2018).

24 Sun, Y. *et al.* Low-Temperature Solution Synthesis of Few-Layer 1T′-$MoTe_2$ Nanostructures Exhibiting Lattice Compression. *Angew. Chem. Int. Ed.* **55**, 2830-2834 (2016).

25 Liu, Z. *et al.* Synthesis of MoX_2 (X = Se or S) monolayers with high-concentration 1T′ phase on 4H/fcc-Au nanorods for hydrogen evolution. *Nano Res.* **12**, 1301-1305 (2019).

26 Wang, X., Shen, X., Wang, Z., Yu, R. & Chen, L. Atomic-Scale Clarification of Structural Transition of MoS_2 upon Sodium Intercalation. *ACS Nano* **8**, 11394-11400 (2014).

27 Zhang, R. *et al.* Superconductivity in Potassium-Doped Metallic Polymorphs of MoS_2. *Nano Lett.* **16**, 629-636 (2016).

28 Liu, Q. *et al.* Stable Metallic 1T-WS_2 Nanoribbons Intercalated with Ammonia Ions: The Correlation between Structure and Electrical/Optical Properties. *Adv. Mater.* **27**, 4837-4844 (2015).

29 Wang, Y. *et al.* Structural phase transition in monolayer $MoTe_2$ driven by electrostatic doping. *Nature* **550**, 487-491 (2017).

30 Kim, S. W. S. *et al.* Long-Range Lattice Engineering of $MoTe_2$ by a 2D Electride. *Nano Lett.* **17**, 3363-3368 (2017).

31 Zhu, J. *et al.* Argon Plasma Induced Phase Transition in Monolayer MoS Structural phase transition. *J. Am. Chem. Soc.* **139**, 10216-10219 (2017).

32 Lin, Y. C., Dumcenco, D. O., Huang, Y. S. & Suenaga, K. Atomic mechanism of the semiconducting-to-metallic phase transition in single-layered MoS Structural phase transition. *Nat. Nanotechnol.* **9**, 391-396 (2014).

33 Nayak, A. P. *et al.* Pressure-induced semiconducting to metallic transition in multilayered molybdenum disulphide. *Nat. Commun.* **5**, 3731 (2014).

34 Huang, X. *et al.* Solution-phase epitaxial growth of noble metal nanostructures on dispersible single-layer molybdenum disulfide nanosheets. *Nat. Commun.* **4**, 1444 (2013).

35 Shang, B. *et al.* Lattice -Mismatch-Induced Ultrastable 1T-Phase MoS_2 -Pd/Au for Plasmon-Enhanced Hydrogen Evolution. *Nano Lett.* **19**, 2758-2764 (2019).

36 Luo, Z. *et al.* Chemically activating MoS_2 via spontaneous atomic palladium interfacial doping towards efficient hydrogen evolution. *Nat. Commun.* **9**, 2120 (2018).

37 Wei, S. *et al.* Iridium-Triggered Phase Transition of MoS_2 Nanosheets Boosts Overall Water Splitting in Alkaline Media. *ACS Energy Letters* **4**, 368-374 (2018).

38 Ji, L. *et al.* One-pot synthesis of porous 1T-phase MoS_2 integrated with single-atom Cu doping for enhancing electrocatalytic hydrogen evolution reaction. *Appl. Catal. B* **251**, 87-93 (2019).

39 Li, H. *et al.* Amorphous nickel-cobalt complexes hybridized with 1T-phase molybdenum disulfide via hydrazine-induced phase transformation for water splitting. *Nat. Commun.* **8**, 15377 (2017).

Chapter 3

Experimental Methodology

This chapter introduces the detailed preparation methods of the 2D TMDs and noble metal-2D TMDs composite materials in the projects. Solution-processed exfoliation is proceeded for the selective layered TMDs and other materials. A photoreduction process is utilized for the synthesis of noble metal-2D TMDs composite materials. Besides, some important characterization techniques are highlighted, including transmission electron microscopy, Atomic force microscopy, Raman spectroscopy, X-ray crystallographic diffraction, and X-ray photoelectron spectroscopy. For each technique, the basic principles, sample preparation and data analysis methods are illustrated.

3.1 Rationale for selection

In Chapter 4 of the thesis, this project focus on the liquid phase exfoliation of metastable 2D TMD materials in high quality, large scale, and high phase purity. Exfoliation of metastable 2D TMDs materials has not been achieved. The mechanical exfoliation method can only get the metastable 2D TMDs in a limited scale, while traditional liquid phase exfoliation will result in a mixed-phase structure instead of pure metastable phase. Thus, it is urgent to develop a general, high yield, high quality and high phase purity method to exfoliate metastable TMDs bulk materials.

In the Chapter 5 of the thesis, this project focused on the epitaxial growth of noble metal nanostructure on 1T′ and 2H-MoS_2 nanosheets towards superior electrocatalysts towards HER. Electrocatalytic HER is the most promising technology to overcome the crisis of energy consumption and environmental pollution caused by the usage of fossil fuel. The small sized, highly dispersed Pt nanostructures with the highest activity are regarded as the best HER electrocatalysts. However, such materials are highly unstable due to the aggregation tendency. Based on the work in the Chapter 4, 1T′-MoS_2 with high phase purity served as excellent substrate to support and stabilize such Pt nanostructure towards superior HER performance.

The rationale for selecting characterization techniques is based on the as-grown bulk TMDs materials, as-exfoliated 2D TMDs materials, and the expected Pt nanostructures. In this project, characterizing the morphology, phase purity, size, and thickness of the as-exfoliated nanosheets are the most important issues. TEM is the most applied technique for determining the morphologies, size, lattice structure, as well as elemental compositions of samples in the nanometer-sized range. The morphology and size distribution of the samples are determined by TEM, SEM, and AFM. AFM is also used to characterize the thickness of the samples. SAED patterns along with the HRTEM are capable of confirming the phase and the atomic structure in both nanosized ranges. High-angle annular dark-field scanning transmission electron microscopy (HAADF-STEM) along with the high-resolution EDS spectrum are capable of characterizing the morphology, size, elemental distribution of the

Pt-MoS_2 hybrid nanomaterials. Raman spectroscopy and XPS are the other two methods to confirm the phase purity in large scale. In the meantime, the study of crystal structure in bulk scale is facilitated by the powder x-ray diffraction (XRD) characterization. A conventional three-electrode system with catalysts deposited on glassy carbon electrode as the working electrode, graphite rod as the counter electrode and Ag/AgCl (3 M KCl) as the reference electrode was used to characterize the HER performance of the MoS_2 nanosheets and MoS_2-based hybrid nanomaterials.

3.2 Chemicals and Synthesis

3.2.1 Chemicals

Potassium molybdate (K_2MoO_4, 98%), sulfur powder (S, 99.5%), tetraethylammonium bromide, isopropanol (IPA, 99.8%), acetonitrile (99.8%), potassium tetrachloroplatinate (II) (K_2PtCl_4, 99.99% trace metals basis) were purchased from Sigma Aldrich. Hydrogen (20% H_2/80% Ar) and purified Argon (Ar, 99.9%) were purchased from Leeden National Oxygen Ltd. in Singapore. Copper foils were purchased from ACME Research Support Pte Ltd (Singapore). Ethanol (99.9%) and acetone (Tech Grade) were purchased from Merck (Germany). N, N-dimethylformamide (DMF) was purchased from Fisher Scientific. Molybdenum powder (~22 mesh, 99.9975%, Puratronic®) was purchased from Alfa Aesar (USA). All chemicals and materials were used as received without any further purification. The Milli-Q water used in experiments was obtained in the Milli-Q System (USA).

3.2.2 Crystal growth

Synthesis of K_xMoS_2 crystals. The K_2MoO_4 (500 mg) and S powder (500 mg) were mixed, ground, and then annealed at 450 °C for 1.5 h under a gas flow of H_2 (10 s.c.c.m.) and Ar (190 s.c.c.m.). After cooling down to room temperature, the product was taken out and mixed with S powder (500 mg) and then annealed again at 450 °C for 1.5 h under an atmosphere of H_2 (10 s.c.c.m.) and Ar (190 s.c.c.m.). Subsequently, the reaction zone was heated to 850 °C at a rate of 30 °C min^{-1} under a reduction atmosphere of H_2 (40 s.c.c.m.) and Ar (160 s.c.c.m.), and maintained at 850 °C for 10 h. After cooling down to room

temperature, the obtained powder was collected and washed with Milli-Q water until the suspension showed a pH of 7-8. The obtained powder was then stored in Milli-Q water for 24 h. After washing with Milli-Q water once again and drying at room temperature under vacuum, the K_xMoS_2 crystals were finally obtained and collected for further usage.

$KMoSe_2$ crystals were synthesized by the similar process as K_xMoS_2 crystals, while Se powder was used instead of S powder.

K_xMoSSe crystals were synthesized by the similar process as K_xMoS_2 crystals, while Se/S mixed powder (molar ratio 1:1) was used instead of S powder.

Preparation of 1T′-MoS_2 crystals. The obtained K_xMoS_2 crystals were soaked in 15 ml I_2 acetonitrile solution (4 mmol) for 3 h and then washed with DI water once. After drying at room temperature under vacuum, 1T′-MoS_2 crystals can be obtained.

3.2.3 Electrochemical exfoliation

Preparation of 1T′-MoS_2 nanosheets (NSs) by electrochemical intercalation. The electrochemical intercalation process was conducted in a two-electrode electrochemical cell. The cathode was prepared by mixing K_xMoS_2 crystals and PVDF as a binder in DMF, which was then coated uniformly on a copper foil and dried under vacuum. The mass ratio of K_xMoS_2 crystals, PVDF, and DMF were 8:1:80. The graphite rod was used as anode. THAB dissolved in acetonitrile with a concentration of 5 mg ml^{-1} served as electrolyte. The intercalation process was performed for 1 h at an applied voltage of 8 V. Then the intercalated sample was transferred into a centrifuge tube and sonicated in 5 ml DMF for a short time (less than 5 seconds). The dispersion was centrifuged at 6,000 r.p.m. for 10 min and the obtained precipitate was then re-dispersed in 5 ml acetonitrile. The final product was collected by centrifugation at 6,000 r.p.m. for 10 min and re-dispersed in Milli-Q water for further experiments.

Preparation of 2H-MoS_2 NSs by electrochemical intercalation. The intercalation and exfoliation process were similar to those used for 1T′-MoS_2, except that the K_xMoS_2 crystals were replaced by commercial 2H-MoS_2 powder.

Synthesis of Pt nanoclusters on 1T′-MoS_2 (Pt/1T′-MoS_2). In a typical procedure, 120 µl of 0.05 M K_2PtCl_4 was injected in 10 ml of 1T′-MoS_2 water-ethanol solution (0.10 mg ml^{-1}, determined by inductively coupled plasma-optical emission spectrometry (ICP-OES)), in which the volume ratio of water/ethanol was 9/1. This mixed solution in a 15 ml glass vial was then irradiated with a 150 W halogen lamp at 10% of its full intensity for 14 h at ambient condition. After the photoreduction reaction, the resulting solution was centrifuged at 6,000 r.p.m. for 15 min, and the precipitates were washed with IPA and collected for further characterization.

Synthesis of Pt nanoparticles on 2H-MoS_2 (Pt/2H-MoS_2). The synthesis process was similar to that used for Pt/1T′-MoS_2, except that the 1T′-MoS_2 NSs were replaced by 2H-MoS_2 NSs and the reaction time was prolonged to 18 h.

3.3 Electrocatalytic measurements.

Hydrogen evolution reaction (HER) measurements were conducted at an ambient condition in a conventional three-electrode system using an Autolab electrochemical workstation (PGSTAT12). The graphite rod and Ag/AgCl (3 M KCl) were used as counter electrode and as reference electrode. The Ag/AgCl electrode was calibrated with respect to a reversible hydrogen electrode (RHE). The working electrode of Pt/1T′-MoS_2 was prepared by drop-casting the Pt/1T′-MoS_2 IPA dispersion onto a glassy carbon electrode (GCE) (3 mm in diameter) with the Pt loading amount of 0.01 mg cm^{-2} as measured by the ICP-OES. The catalyst-coated GCE was dried at room temperature, then 2 µl Nafion ethanolic solution (0.1 wt%) was dropped on its surface to protect the catalyst. Using the same procedure, the Pt/2H-MoS_2, 1T′-MoS_2 NSs, 2H-MoS_2 NSs, and Pt/C were loading on the working electrode as well. The weights of 1T′-MoS_2 NSs, 2H-MoS_2 NSs and Pt/1T′-MoS_2 were kept the same (0.1 mg cm^{-2}). The mass loadings of Pt were kept the same (0.01 mg

cm^{-2}) for Pt/1T′-MoS_2, Pt/2H-MoS_2, and Pt/C catalysts. After being dried, the electrodes were used for the electrochemical measurements. The HER test was conducted in 0.5 M H_2SO_4 aqueous solution (purged by pure N_2). Current densities were normalized by the geometric area of the electrode. Linear sweep voltammetry (LSV) curves were measured in the N_2-saturated 0.5 M H_2SO_4 aqueous solution at a sweep rate of 5 mV s^{-1}. The durability tests were performed by applying the cyclic potential sweeps between 0.1 V and -0.1 V (vs RHE) at a scan rate of 100 mV s^{-1} for 10,000 cycles. The chronoamperometric test was conducted in the N_2-saturated 0.5 M H_2SO_4 aqueous solution for 30 h. Electrochemical impedance spectroscopy (EIS) was recorded over the frequency range from 100 kHz to 0.1 Hz with an amplitude of applied voltage of 10 mV. All the LSV curves are iR-corrected on basis of the EIS data.

Measurements of ECSA. Electrochemically active surface area (ECSA) of catalysts were measured by the CO stripping experiments using the previously reported method[1]. The CO adsorption was conducted in 0.5 M H_2SO_4 aqueous solution with bubbling CO for 20 min. The electrolyte was then saturated with N_2 by bubbling N_2 for 15 min to remove the dissolved CO in the electrolyte. During all the aforementioned procedures, the potential was maintained at 0.1 V *vs.* RHE. In this method, the number of active sites was calculated on basis of the CO stripping charge (Q_{CO}) with the following equation:

$$n=Q_{co}/(2Fm) \quad (1)$$

where F is the Faraday constant (96485 C mol^{-1}), and m is the metal mass loading (1.9×10^{-6} g).

The turnover frequency (TOF, H_2 s^{-1}) can be calculated by using the following equation:

$$TOF=I/(2Fnm) \quad (2)$$

where I represent for the current (A) during measurement. The factor, 2, is the number of electron transferred.

Assuming a value of 420 μC cm^{-2} for a saturated CO monolayer formation on active metal

sites, the ECSA can be calculated as follows:

$$ECSA = Q_{CO}/(m \times 420\ \mu C\ cm^{-2}) \quad (3)$$

3.4 Characterization.

3.4.1 Field emission scanning electron microscope (FESEM)

JEOL 7600F instrument FESEM was used to obtain the SEM images in this project with an accelerating voltage of 10 kV. FESEM is a very effective tool to determine the size and surface morphology of the samples and is commonly used all over the world. FESEM utilized electrons instead of light to work as a microscope. Under an accelerating voltage, electrons generated by the field emission source are liberated from the electron gun. The electron beam will then be focused under a high vacuum column and deflected by a series of lenses resulting with a very narrow electron beam bombarding the sample. During the interaction between the sample and electron beam, several electronic signals will be generated such characteristic X-rays, back-scattered electrons, and secondary electrons. Among these signals, secondary electrons are capable of revealing the sample morphology on the surface. Such secondary electrons are collected and analyzed by the computer ending up as a real image.

For the SEM test, secondary electrons were utilized as the signal to get detail surface morphology of K_xMoS_2 crystals, K_xMoS_2 crystals after washing, 1T′-MoS_2 nanosheets, 1T′-$MoSe_2$ nanosheets, and 1T′-MoSSe nanosheets. K_xMoS_2 crystals after washing was directly placed on the conductive carbon tape for measurement. For the nanosheets samples, the nanosheets are dispersed in the solution and dropped on the silicon substrate for characterization. The gold coating is not necessary for the sample.

3.4.2 Transmission electron microscopy (TEM)

All the TEM characterization including, TEM images, EDS and element mapping were obtained by a JEOL JEM-2100 electron microscope. TEM is a major analytical technique in modern nanotechnology. TEM is consisted of four main systems including electron

source, electromagnetic lens system, specimen port, and imaging system. When a material is bombard by a focused high-energy electron beam in a high vacuum environment, the transmission electrons will be detected and to be viewed. Because of the smaller wavelength of electrons, TEM has an extraordinarily high magnification up to 1,000,000x and ultra-high resolution of <1 nm. The signal of transmission electrons is highly influenced by the chemical composition, thickness and other properties of samples, so that the following information can be obtained from TEM test: (a) Sample morphologies from high resolution images; (ii) Crystal structures from diffraction pattern; (iii) Elemental compositions and distribution from EDS analysis.

For the sample preparation, the 1T′-MoS_2, 1T′-$MoSe_2$, 1T′-MoSSe, 2H-MoS_2 nanosheets sample and the Pt/1T′-MoS_2, Pt/2H-MoS_2 samples were dispersed in IPA and dropped on ultrathin amorphous carbon film-coated copper girds, following by drying at room temperature in a vacuum oven.

3.4.3 Scanning Transmission Electron Microscopy (STEM)

The high angle annular dark field (HAADF) scanning transmission electron microscopy (STEM) images were recorded on a JEOL ARM200F (JEOL, Tokyo, Japan) transmission electron microscope equipped with a cold field emission gun and double hexapole Cs correctors (CEOS GmbH, Heidelberg, Germany), operating at accelerating voltage of 200 kV. Since the HRTEM cannot distinguish different elemental atoms on the nanodots and nanosheets, the HAADF-STEM technique is another powerful supplementary technique used to acquire the clear and precise atomic distribution of the Pt-MoS_2 hybrid nanomaterials. The underlying principle is that under HAADF-STEM mode, the image contrast of different atom is highly correlated to the Z number of the elements, i.e., heavy atom (large Z number) shows brighter contrast compared to the light atom (small Z number).

For the sample preparation, the 1T′-MoS_2, 1T′-$MoSe_2$, 1T′-MoSSe, 2H-MoS_2 nanosheets sample and the Pt/1T′-MoS_2, Pt/2H-MoS_2 samples were dispersed in IPA and dropped on

ultrathin amorphous carbon film-coated copper girds, following by drying at room temperature in a vacuum oven.

3.4.5 UV-Vis Absorption Spectroscopy

The UV-Vis absorption spectra were measured by a Lambda 950 UV/Vis Spectrophotometer (PerkinElmer Inc., USA) at room temperature using QS-grade quartz cuvettes (111-QS, Hellma Analytics). In this thesis, the UV-Vis technique is used to study the absorption features of 1T′- and 2H-MoS_2 nanosheets dispersion.

3.4.6 X-ray diffraction (XRD)

XRD is one of the most common used technique to investigate the crystal structure of materials. The continues X-ray passes through the crystals and be scattered by the lattice of the crystals, elastic scattering is generated as a secondary spherical wave. The interference of the scattering waves results in an enhancement at specific direction. The relationship between incident X-ray wavelength, lattice spacing and the diffraction angle can be described as Bragg′s Law which is expressed as $2d\sin\theta=n\lambda$. It has multiple functions, such as identification of the crystal structure, determination of the spacing between lattice planes and the particle size, as well as investigation of the preferential ordering and epitaxial growth of crystallites.

For the sample preparation, the crystals sample were deposited on the XRD sample holder and pressed a little bit to make the surface flat. All of the XRD patterns were measured in the range of 10° to 80° with an

average interval of 0.05o and a dwell time of 1 second.

3.4.7 Atomic force microscopy (AFM)

AFM characterization was conducted on a Dimension 3100 AFM machine. A typical AFM is consisted of AFM probe (cantilever & tip), laser, piezo position system, photodiode detector and electronic control system. What′s most important among these is an ultra-

sharp tip with size of around 1 nm. During AFM test, the tip will be forced to approach the sample surface very closely while the van der Waals′s force leads to the vibration of the tip. The vibration is then amplified by the laser reflection, and the signal is collected by the photodetector. Analyzed by the computer, a real image of the surface morphology is presented.

For the sample preparation, the nanosheets sample are dispersed in the solution and dropped on the silicon substrate for characterization.

3.4.8 X-ray photoelectron spectroscopy (XPS)

X-ray photoelectron spectroscopy was performed on an Axis Ultra spectrometer. A typical XPS instrument is consisted of the X-rays source, vacuum system, electron collection lens and electron energy analyzing system. In a normal XPS test, a focused X-ray beam will bombard the sample and generated photoelectrons, while the kinetic energy and escaped electron number can be recorded. Accordingly, the electron binding energy can be calculated by the equation: $E_{binding}=E_{photon}-E_{kinetic}-\phi$, where E_{photon} represented the energy of the X-ray photons and ϕ is the work function which is determined by both the spectrometer and the material. However, XPS spectra can only collect the signals close to the sample surface (depth of 1~10 nm). Therefore, XPS is sensitive both the chemical valence of the elements and the surface chemical composition.

For the sample preparation, the nanosheets and the Pt-MoS_2 hybrid samples are dispersed in the solution and dropped on the silicon substrate for characterization.

3.4.9 Raman spectroscopy

By utilizing the interaction of light and matter, Raman spectroscopy provides information about intra- and inter-molecular vibrations which helps researchers analysis the material′s composition or properties. The incident high intensity laser light is scattered by the sample molecules. Most of the scattered light is elastic scatter, known as Rayleigh Scatter, which has the same wavelength as the laser source and provides nothing useful. Whereas, the

weak inelastically scattered light, known as Raman Scatter, which occupied only a small percentage (normally 0.0000001%) is scattered at different wavelengths strongly depending on the chemical structure of the sample. Raman scattered light was featured as peaks in a Raman spectrum with specific intensity and wavelength corresponding to a characteristic molecular bond vibration. Both the individual bonds vibration including C-C, C=C, C-H, N-O, and the groups of bonds such as benzene ring breathing mode, lattice modes and polymer chain vibrations can be detected clearly.

Therefore, specific chemical structure of samples can be distinguishable probed by Raman spectroscopy and the following information is provided: (a) Chemical structure and identity; (b) Polymorphism and Phase, (c) Intrinsic stress/strain, (d) Contamination and impurity.

For the sample preparation, the nanosheets and the Pt-MoS_2 hybrid samples are dispersed in the solution and dropped on the silicon substrate for characterization.

3.5 Strengths and Limitations of Methodological Approach

In this project, liquid-phase exfoliation method is used. It is one of the most popular and powerful method towards the exfoliation of layered TMD materials. Significant progress has been achieved after years of development, almost all the layered TMD materials can be exfoliated to monolayer or few-layers by the liquid-phase exfoliation method such as solvent assisted exfoliation, alkali metal intercalation method in large scale, and high quality. However, there remains several disadvantages. Liquid-phase exfoliation strongly relies on long time sonication, active metal intercalation, surfactant or strict operation environment (in glove box) which will induce phase transition. The exfoliation induced phase transition will destroy the original phase structure which severely hinders the application in metastable TMDs exfoliation. Therefore, a new liquid-phase exfoliation method is developed in this project. Quaternary ammonium molecules instead of the alkali metal is electrochemical intercalated inside the TMD materials which donor fewer electrons to the materials resulting in maintain the original phase structure. In addition, the

sonication time is reduced to only tens of seconds and no surfactant is used. This method is particular useful for metastable materials exfoliation. However, the liquid-phase exfoliation process introduced many organic molecules or solvent which may harmful for the following device fabrication or application.

In terms of characterization, SEM, TEM and Raman spectroscopy are three of the most important characterization in this project. Such measurement revealed the morphology, crystal structure, phase purity on both bulk materials and as-exfoliated nanosheets. However, the metastable TMDs, especially in the 2D form, are sensitive to the Raman laser and the electron beam bombarding of TEM. The utilizing of high energy laser, electron beam and longtime measurement will result in partially or even complete phase transition within single nanosheet, which will destroy the sample and provides wrong information. Therefore, the SEM, TEM and Raman spectroscopy should be measured carefully.

Reference

1 Liu, G. *et al.* Synthesis of RuNi alloy nanostructures composed of multilayered nanosheets for highly efficient electrocatalytic hydrogen evolution. *Nano Energy*, **66**, 104173 (2019)

Chapter 4

Preparation of high phase purity 1T′-TMD nanosheets

This chapter presents the results and discussion of the preparation of high phase purity 1T′-TMD nanosheets. An introduction is given first. Characterization results are presented then revealing the morphology, thickness distribution, crystal phase etc. The exfoliation results of many other layered materials are presented as well to show the generality of this method.

4.1 Introduction

Great advancement has been achieved in 2D materials which greatly accelerated the research in 2D transition-metal dichalcogenides (TMDs) owing to the intrinsic novel properties and applications[1-3]. TMDs can be written with the formula MX_2, with transition metal 'M' and chalcogen 'X'. With different chemical composition and polymorphism, TMDs bulk exhibit a variety of unique electronic properties which have been widely studied. While exfoliated to few-layers or monolayer, 2D TMDs materials display extraordinary electrical and optical properties owing to surface effects and quantum confinement. For example, bulk 2H-MoS_2 exhibited an indirect bandgap of 0.88eV while monolayer 2H-MoS_2 was proved to have a direct bandgap 1.71 eV[4]. In addition, the 2H-MoS_2 is a semiconductor while the metastable 1T-MoS_2 shows metallic property[5]. However, it is still limited towards large scale preparation of metastable 2D TMDs materials. Take MoS_2 as an example, large scale preparation of MoS_2 nanosheets was traditionally achieved liquid phase exfoliation[6], chemical/electrochemical lithium intercalation[7,8] or directly synthesis by wet-chemical method such as hydrothermal method[9,10]. However, the obtained metastable 2D MoS_2 from aforementioned methods was normally a mixture of 2H and 1T′ phase, which severely hindered the deep study of the pure 1T′ phase properties or application. Mechanical exfoliation of bulk 1T′-TMDs crystals[11] and CVD growth of the 1T′-TMDs[12] are reported recently while such methods are limited by low yield, low production rate, and harsh experimental condition, which are not suitable for practical applications[11,12]. Therefore, it is urgent to develop a facile, controllable method for high yields of 2D 1T′-TMDs production with high phase purity.

Taking MoS_2 as an example, liquid phase exfoliation of 1T′-MoS_2 holds great promise for scalable production as well as the following functionalization and hybridization of MoS_2. However, the traditionally used liquid phase exfoliation method requires longtime sonication which is detrimental for the 1T′-MoS_2. As a proof, as-synthesized 1T′-MoS_2 crystals were dispersed in DMF solvent, UV-Vis spectra were used to test the stability of the as-sonicated samples. The UV-Vis spectra of the sample with different sonication time is shown in Figure 4.1, the inset shown the optical images of different samples. It is found

that, even after 1-minute sonication, a clear absorption peak of 2H-MoS_2 is shown in the UV-Vis spectra. After 5 minutes sonication the peak becomes more obvious, while the 30 minutes sonication leads to a color change of the solution from grey to green indicating a high percentage of 2H-MoS_2.

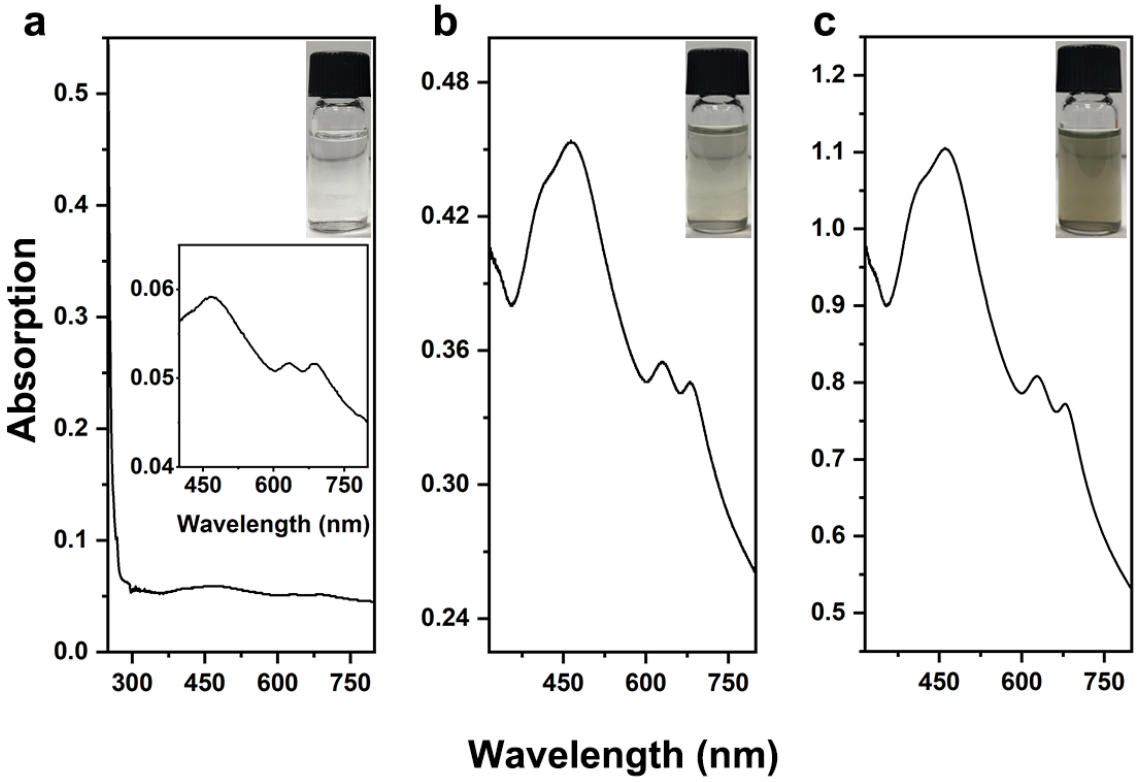

Figure 4.1 Ultraviolet-visible absorption spectra of the 1T′-MoS_2 sonicated in the DMF solvent for **a**, 1 minute, **b**, 5 minutes, and **c**, 30 minutes. Insets show the photographs of the as-sonicated samples in DMF samples.

In addition the reported lithium intercalation method can only operate in glove box and requires the use of hazardous chemicals such as *n*-butyllithium which is not suitable for the large-scale production of 1T′-MoS_2. In addition, the lithium intercalation method could also induce irreversible phase transition from 1T′ to 2H. As a proof, a small amount of 1T′-MoS_2 crystals are immersed inside a 1.6 M solution of n-BuLi in hexane for 3 days and then take out and washed following the previous reported method[13]. As shown in Figure

4.2, the as-prepared 1T′-MoS_2 nanosheets showed an absorption peak at around 400 nm, indicating the formation of 2H-MoS_2 (REF[6]).

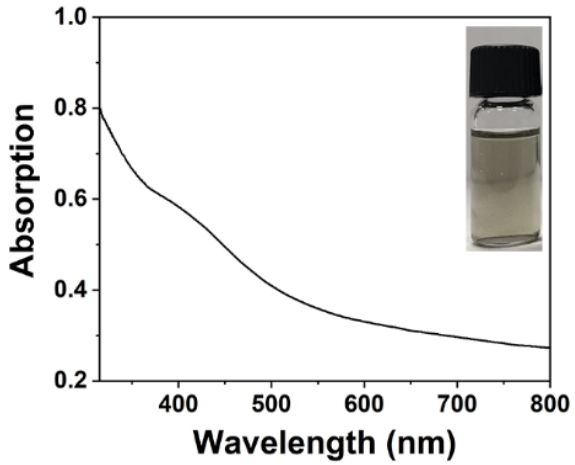

Figure 4.2 UV-Vis spectrum of the lithium intercalation exfoliated 1T′-MoS_2 NSs. Inset shows the photograph of the as-exfoliated sample in water.

Here, a general electrochemical intercalation and exfoliation method was developed in this project. In this approach, THAB was used as intercalation agents instead of the traditional alkali metal. Highly uniform, ultrathin TMD nanosheets can be exfoliated in a large scale. What′s more important is that the intercalation of THAB will not result in any phase transition, thus high phase purity 1T′-TMDs nanosheets can be exfoliated successfully. Take the example of MoS_2, the intercalation is proceeded in a layered K_xMoS_2 crystals resulting in a large scale of 1T′-MoS_2 nanosheets while the intercalated K can be simultaneously removed. High phase purity, 1T′-MoS_2 NSs with a thickness of 1.4±0.4 nm were prepared and systemically characterized by Raman, STEM, UV-Vis and electrical transport characterizations. As a proof of concept application, the solution processed 1T′-MoS_2 NSs showed high catalytic activity for HER. In addition, such method can be expanded to prepare other kind of 1T′-TMDs NSs such as 1T′-$MoSe_2$, 1T′-MoSSe. Our approach offered a promising way towards the large-scale preparation of ultrathin metastable 2D 1T′-TMD materials to further explore their properties and applications.

4.2 Outcomes

4.2.1 Electrochemical intercalation and exfoliation process

Large scale, high uniformity, high phase purity exfoliation of 1T′-TMDs materials is achieved within a simple electrochemical cell. Taking MoS_2 as an example, the K_xMoS_2 crystals are prepared through a crystal growth process combined with the following treatment. K_xMoS_2 is synthesized as described in Chapter 3, and the as-prepared crystals were washed three times till the suspension shows a pH of 7-8. The sample was then soaked in water for 24 hours. After soaking, the water is intercalated inside while the potassium amount decreased slightly. The as-prepared K_xMoS_2 is observed by SEM and analyzed by EDS as shown in Figure 4.3. it can be seen from Figure 4.3a and b, after washing and soaking for 24 hours, the K atomic percentage in the as-prepared crystals decreased from 11.77% to ~6.58%. Meanwhile, the EDS data shows that the Mo and S in both crystals have a similar atomic ratio of 1:2 which is in accordance with the formula. As shown in Figure 4.4c from SEM observation, the as-prepared K_xMoS_2 crystals have a flake-like morphology with the lateral size of about 50-500 μm.

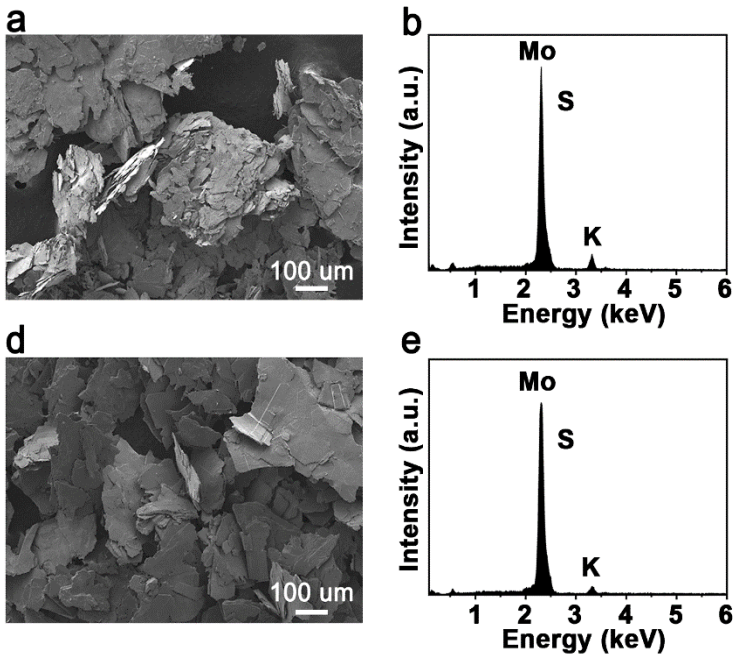

Figure 4.3 a, SEM image and the corresponding **b**, EDS spectra, and **c**, element composition of $KMoS_2$ crystals. **d**, SEM image, and the corresponding **e**, EDS spectra and **f**, element composition of K_xMoS_2 crystals after washing.

As proof of the enlarged layer distance, the XRD patterns of the K_xMoS_2 crystals, K_xMoS_2 crystals after washing are presented in **Figure 4.4**. As shown in the XRD patterns, the peaks of K_xMoS_2 after washing matched well with the as-prepared K_xMoS_2, indicating that the washing process did not influence the crystal structure of K_xMoS_2. The K_xMoS_2 after washing was then loaded on the cathode for further exfoliation.

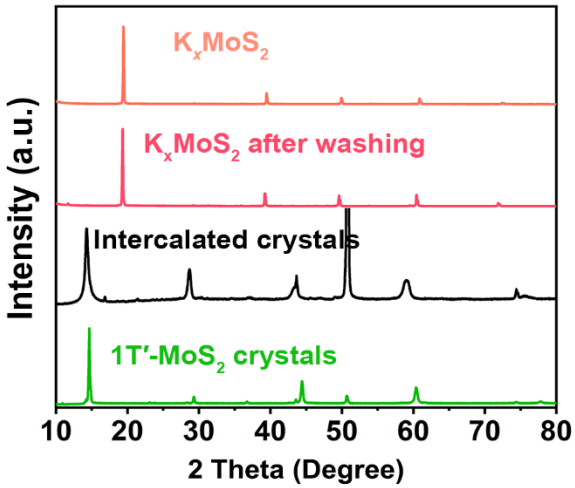

Figure 4.4 XRD patterns showing the structural transition during the intercalation process.

4.2.2 The morphology characterization

The preparation of 1T′-MoS_2 NSs is illustrated in Figure 4.5a (see Chapter 3 for details). Briefly, the THAB molecules were first intercalated into the prepared K_xMoS_2 crystals in an electrochemical cell (Step 1 in Figure 4.5a). The intercalated crystals exhibit a similar XRD pattern with the 1T′-MoS_2 crystals (Figure 4.4a). Then the intercalated crystals were transferred into a centrifuge tube and sonicated in 5 ml DMF for less than 5 s (Step 2 in Figure 4.5a).

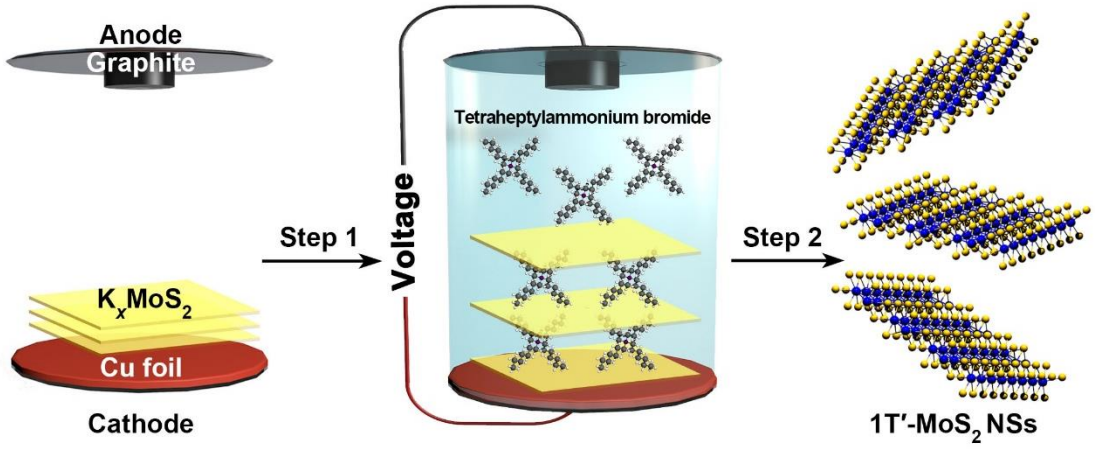

Figure 4.5 Schematic illustration of preparing 1T′-MoS_2 NSs from K_xMoS_2 crystals through the electrochemical intercalation (Step 1) and subsequent exfoliation (Step 2).

After the washing process, 1T′-MoS_2 NSs with a lateral size of up to several micrometers (Figure 4.6a) can be prepared. The AFM results in Figs. 4.6 b and c show that the 1T′-MoS_2 NSs exhibit a narrow thickness distribution of 1.4±0.4 nm. TEM image (Figure 4.6d) shows a representative 1T′-MoS_2 NS with a clean surface. The selected area electron diffraction (SAED) pattern (Figure 4.6e) confirms the distorted octahedral coordinated structure and the good crystallinity of the obtained 1T′-MoS_2 NSs. As shown in the aberration-corrected HAADF-STEM image (Figure 4.6f), the zigzag chains with the shortest Mo-Mo distance can be easily observed, which is consistent with the structure of 1T′-MoS_2 (Figure 4.7).

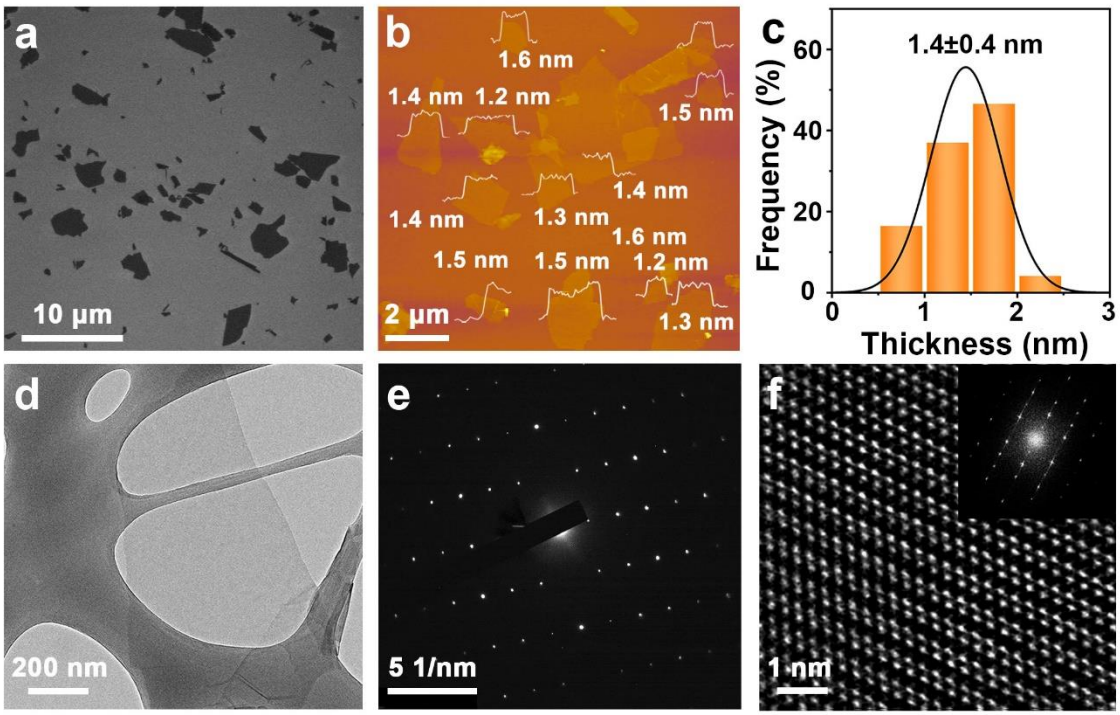

Figure 4.6 Morphology characterization of the exfoliated 1T′-MoS_2 nanosheets: **a**, SEM image of 1T′-MoS_2 NSs. **b**, AFM image of the 1T′-MoS_2 NSs. Insets in **b**: the height profiles and measured thicknesses of 1T′-MoS_2 NSs. **c**, Statistical analysis of the thickness of 1T′-MoS_2 NSs measured by AFM. **d**, TEM image and **e**, the corresponding SAED pattern of the 1T′-MoS_2 NSs. **f**, HAADF-STEM image of a typical 1T′-MoS_2 NS. Inset: the corresponding FFT pattern.

The magnified HAADF-STEM image and the corresponding line-scanning intensity profile in Figure 4.7 show that the shortest Mo-Mo distance is measured as 2.78 Å, which

is consistent with the theoretical 1T′-MoS_2 structure (Figure 4.8).

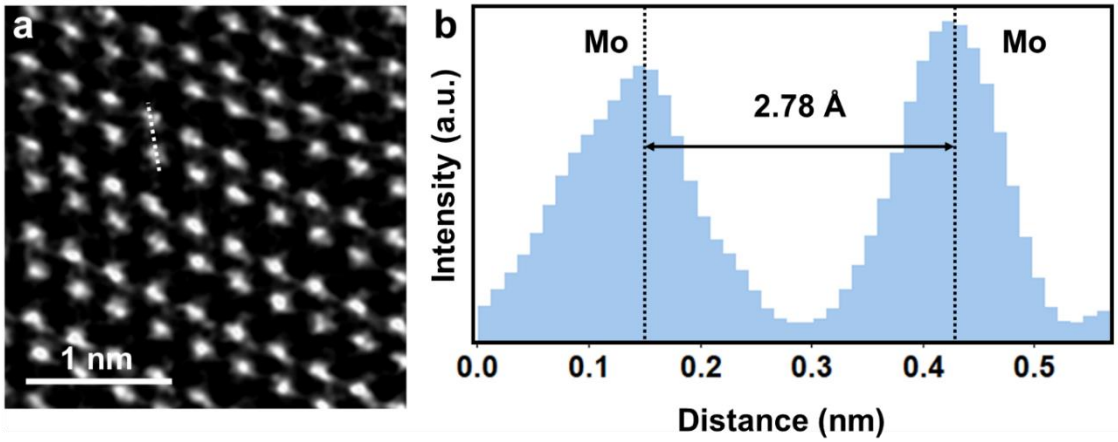

Figure 4.7 a, HAADF-STEM image of 1T′-MoS_2 NS. **b**, The corresponding line-scanning intensity profile obtained from the white dotted line in **a**.

The following Figure 4.8 show the detailed atomic structure of 1T′-MoS_2 and 2H-MoS_2. 1T′-MoS_2 exhibits a distorted octahedral coordinated structure and a characteristic Mo-Mo zig-zag chain with a theoretically shortest distance of 2.78 Å. In comparison, the 2H-MoS_2 exhibits a trigonal prismatic coordinated structure with hexagonal symmetry. Theoretically, the (100) planes of 2H-MoS_2 exhibit an interlayer spacing of 2.74 Å.

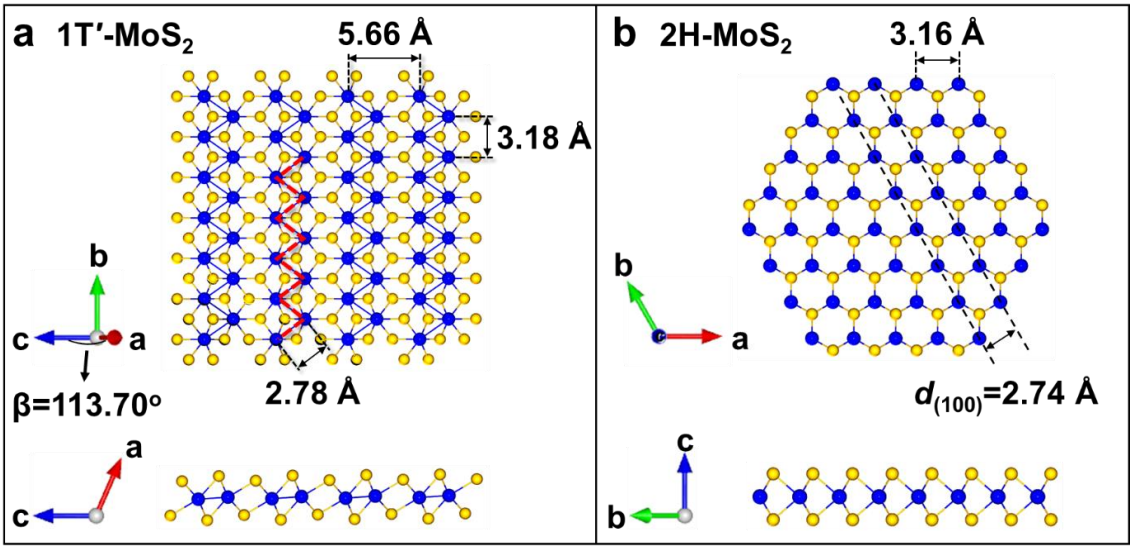

Figure 4.8 a,**b**, Schematic illustrations of the atomic structures of 1T′-MoS_2 (**a**) and 2H-MoS_2 (**b**). The red dashed lines in **a** show the zig-zag chain of Mo atoms in 1T′-MoS_2 with a shortest Mo-Mo distance of 2.78 Å. The black dashed lines in **b** show the (100) planes of 2H-MoS_2 with a theoretical interlayer spacing of 2.74 Å.

The uniform elemental distribution of Mo and S elements with an expected Mo/S ratio of ~1:2 is further confirmed by the energy dispersive X-ray spectroscopy (EDS). As indicated by the EDS results no potassium, bromide, and other residues are detected in the obtained 1T′-MoS_2 NSs, confirming the high purity of 1T′-MoS_2 NSs.

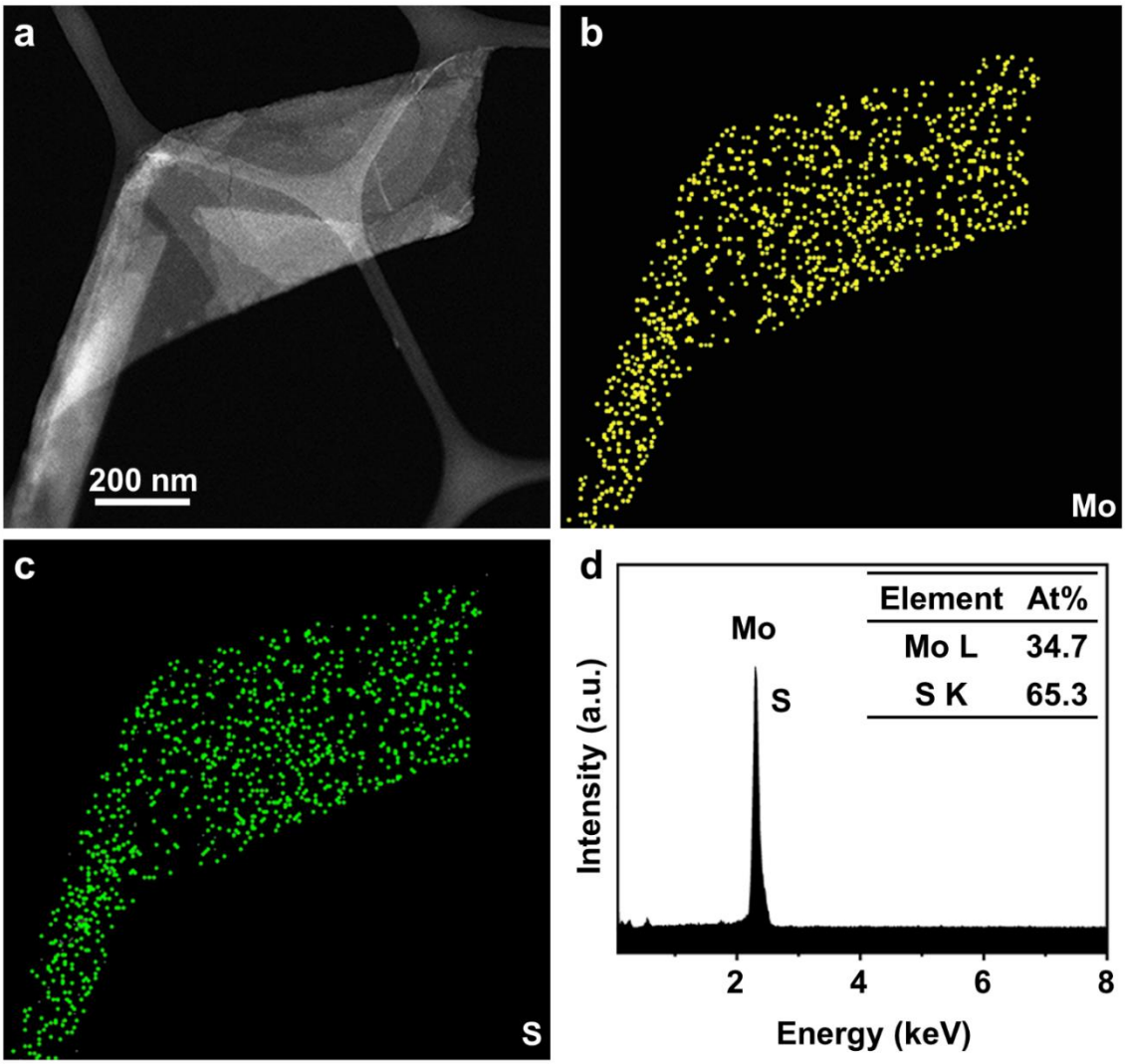

Figure 4.9 a, STEM image, and **b**,**c**, the corresponding EDS mappings of a representative 1T′-MoS_2 NS. **d**, EDS spectrum of the 1T′-MoS_2 NS in **a**, indicating no detectable potassium (Kα 3.31 eV), bromide (Lα 1.48 eV), and other residues in 1T′-MoS_2 NS. Inset in **d**, the corresponding elemental ratio.

In addition, XPS spectrum was used to detect the K element residue. As shown in Figure 4.10, after the intercalation process, the K element is removed from the sample, no K signal is detected in the XPS spectrum.

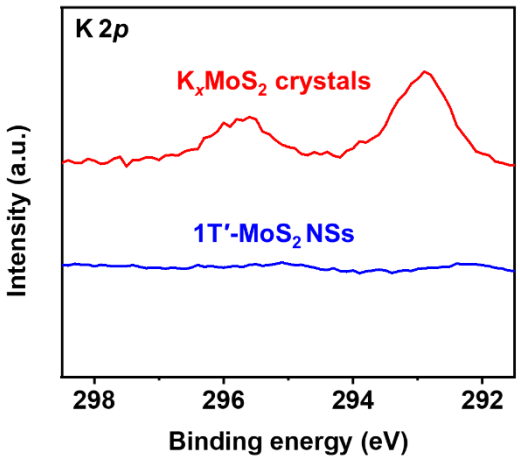

Figure 4.10 The K 2*p* XPS spectra of the K_xMoS_2 crystals and the obtained 1T′-MoS_2 NSs.

To make a clear comparison, the same electrochemical intercalation and exfoliation method is utilized to exfoliate the 2H-MoS_2 NSs. The SEM image (Figure 4.11a) shows that micrometer-sized 2H-MoS_2 NSs were prepared. The TEM image and the corresponding SAED pattern with hexagonal diffraction spots (Figure 4.11b) indicate the high crystallinity of the 2H-MoS_2 NSs. Moreover, the measured lattice spacing of 2.71 Å as shown in the HRTEM image (Figure 4.11c) can be assigned to the {100} planes of the 2H-MoS_2 NSs, which is consistent with the theoretical structure of 2H-MoS_2 as illustrated in (Figure 4.8b). In addition, the EDS spectrum (Figure 4.11d) shows an expected Mo/S ratio of ~1:2. Furthermore, AFM results reveal that the exfoliated MoS_2 NSs possess a thickness of 1.9±0.4 nm (Figures 4.11e,f).

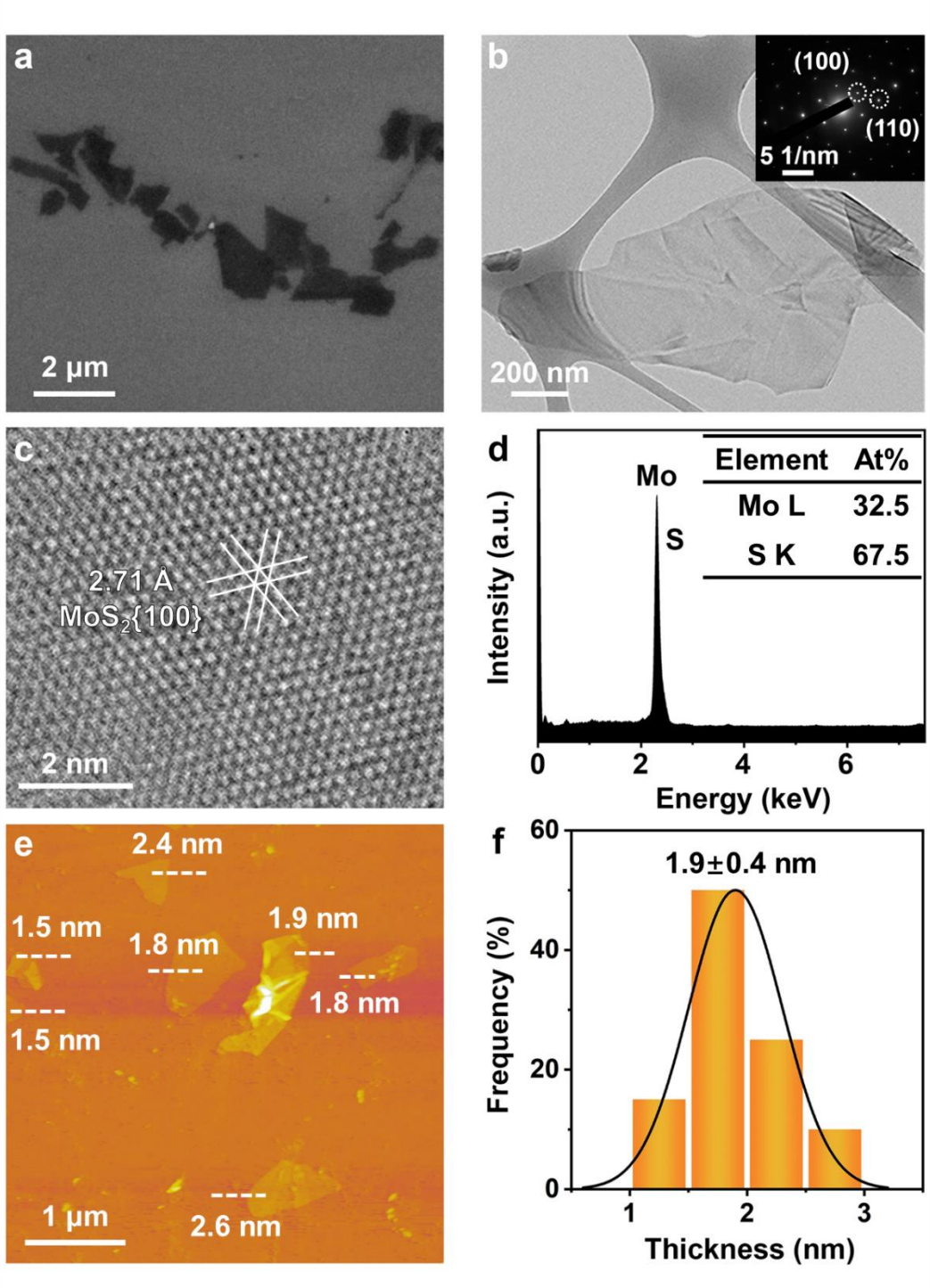

Figure 4.11 a, SEM image of the exfoliated 2H-MoS_2 NSs. **b**, TEM and **c**, HRTEM images of a representative 2H-MoS_2 NS. Inset in **b** shows the corresponding SAED pattern. **d**, EDS spectrum and the element ratio (inset in **d**) of the 2H-MoS_2 NSs. **e**, AFM image and the measured thicknesses

(insets in **e**) of 2H-MoS_2 NSs. **f**, Statistical analysis of the thickness of 2H-MoS_2 NSs measured by AFM.

Various methods were then conducted to characterize the phase purity of exfoliated nanosheets in detail. The prepared 1T′-MoS_2 and 2H-MoS_2 NSs were further characterized by the ultraviolet-visible (UV-Vis) absorption, XPS, and Raman spectra. As shown in the UV-Vis spectrum (Figure 4.12), the featureless absorption of 1T′-MoS_2 NS dispersion indicates its metallic nature. On the contrary, the 2H-MoS_2 NS dispersion shows four featured peaks located at 400, 454, 618, and 675 nm, respectively, consistent with the previous report[6].

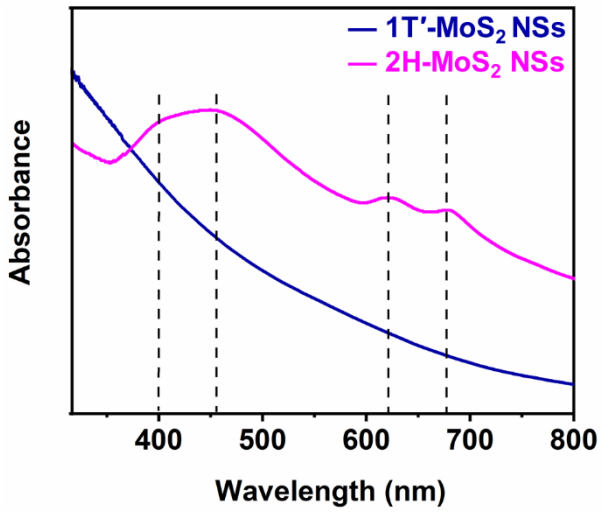

Figure 4.12 UV-Vis spectra of the exfoliated 1T′-MoS_2 NSs and 2H-MoS_2 NSs dispersed in DMF. Four featured peaks are clearly observed in the UV-Vis spectrum of 2H-MoS_2 NSs as indicated by the black dashed lines.

As shown in Figure 4.13a, the XPS spectra of 1T′-MoS_2 NSs shows that both binding energies of Mo 3$d_{5/2}$ and Mo 3$d_{3/2}$, *i.e.*, 228.7 eV, and 231.8 eV, respectively, shift to lower values by about 0.8 eV compared to that of 2H-MoS_2, which is in accordance with a previous report[11]. A similar upshifted was also observed in the binding energy for the S 2*s* region from 224.9 eV to 226.6 eV .In addition, the Raman spectrum of the as-prepared 1T′-MoS_2 NSs exhibit five characteristic peaks, *i.e.*, 151.8 (J_1), 213.6 (J_2), 280.8, 328.4 (J_3), and 404.1 (A_{1g}) cm^{-1}, respectively (Figure 4.13b), matching well with previous reports[11,14].

Importantly, the characteristic E^1_{2g} peak of 2H-MoS_2 located at 382.8 cm^{-1} is absent, confirming the high phase purity of the prepared 1T′-MoS_2 NSs.

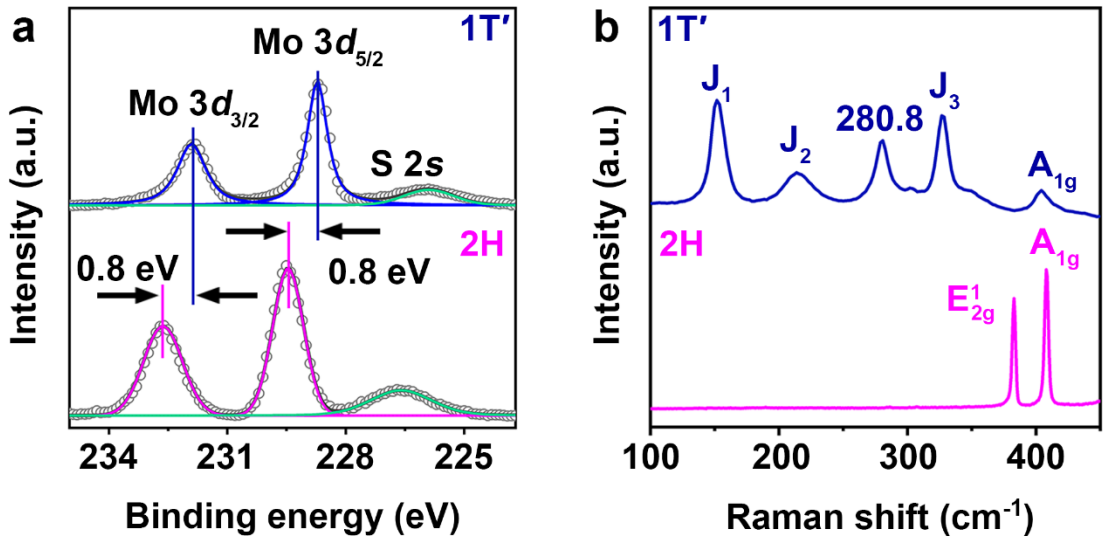

Figure 4.13 a, XPS spectra of exfoliated 1T′-MoS_2 NSs and 2H-MoS_2 NSs. The grey circles and the solid lines show the experimental XPS data and the corresponding deconvoluted spectra, respectively. **b**, Raman spectra of exfoliated 1T′-MoS_2 NSs and 2H-MoS_2 NSs.

As compared with bulk 1T′-MoS_2 crystals (Figure 4.14a), the peaks of 1T′-MoS_2 NSs are all upshifted to the higher wavenumbers, which could be caused by the thickness reduction of layered TMD nanomaterials[15]. In the meantime, the phase transition test is conducted during the Raman characterization process. The 1T′-MoS_2 nanosheets can be converted to 2H phase under Raman beam irradiation. As shown in Figure 4.14b, under continuous laser irradiation, two typical Raman modes (A_{1g} and E^1_{2g}) were appeared in the intermediate and getting stronger in the final product after long time of irradiation. A complete phase transition is demonstrated by the strong A_{1g}, E^1_{2g} characterization peaks of 2H-MoS_2 and the absence of J_1, J_2, J_3 peaks for 1T′-MoS_2.

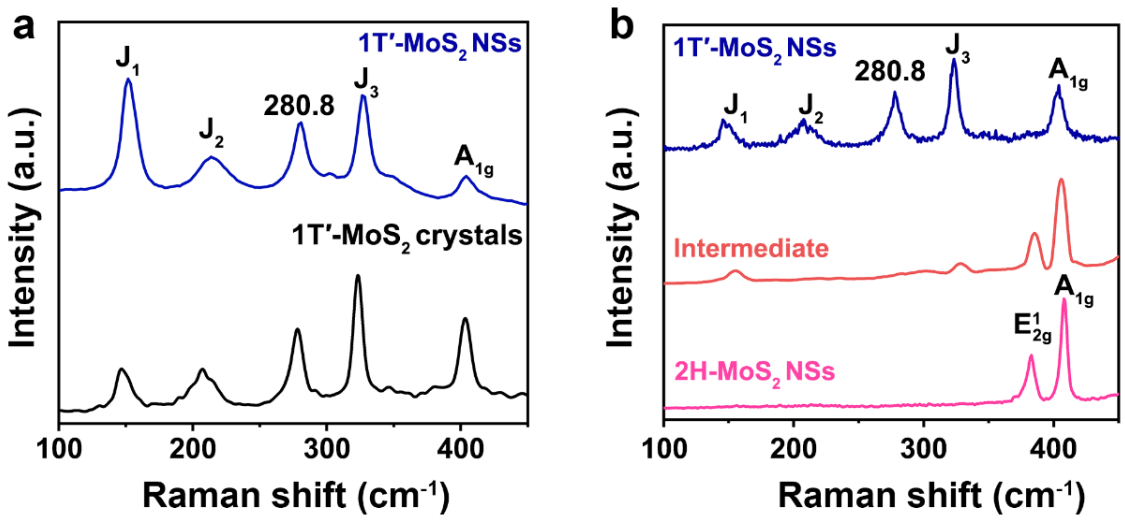

Figure 4.14 a, Raman spectra of 1T′-MoS_2 crystals and 1T′-MoS_2 NSs. **b**, Raman spectra showing the phase transition from 1T′-MoS_2 NSs to 2H-MoS_2 NSs under the continuous laser beam.

As for the 2H-MoS_2 NSs, two characteristic Raman peaks, *i.e.*, 382.8 cm^{-1} (E^1_{2g}) and 407.8 cm^{-1} (A_{1g}), are clearly observed (Figure 4.13b), which are consistent with the previous report[3]. All the aforementioned results confirm that the 1T′-MoS_2 and 2H-MoS_2 NSs with high-phase purity and high crystallinity have been prepared by using our method.

Besides 1T′-MoS_2, the exfoliation method has been successfully used to prepare a variety of metastable TMD nanosheets, such as 1T′-$MoSe_2$, and metastable alloys 1T′-MoSSe crystals. Such crystals are synthesized recently within our group. Same with the 1T′-MoS_2, it is proved that the K_xMoSe_2, K_xMoSSe crystals can be used to prepare 1T′-$MoSe_2$ and 1T′-MoSSe NSs. The morphology and phase purity characterization are conducted by SEM, TEM and the corresponding SAED patterns. Figure 4.15 and 16 showed that the 1T′-$MoSe_2$ nanosheets and 1T′-MoSSe nanosheets have a flat-like morphology, a clean surface and a lateral size more than 1 μm. The corresponding SAED patterns confirmed the 1T′ phase of the obtained nanosheets.

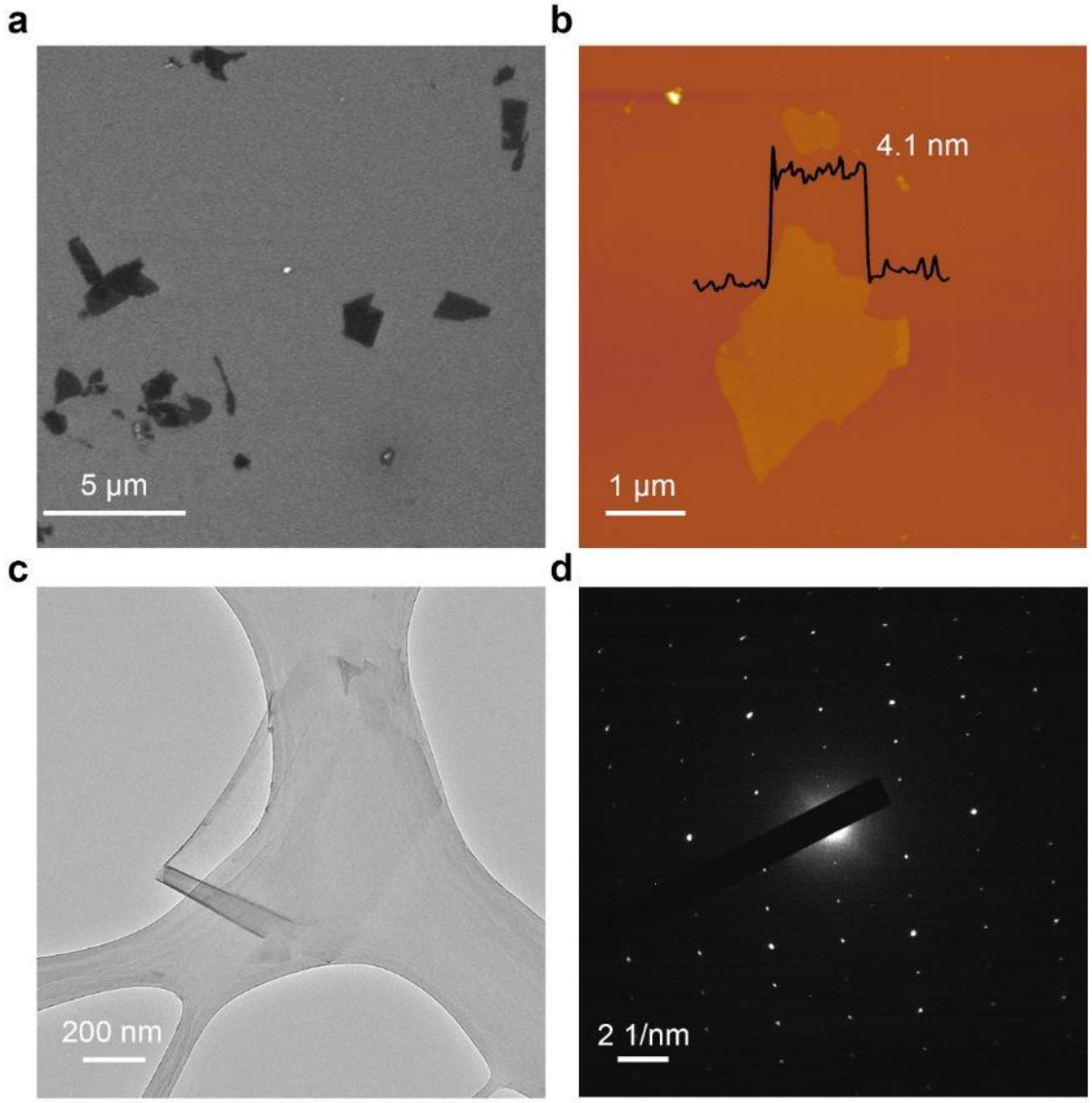

Figure 4.15 a, SEM, **b**, AFM, **c**, TEM, and **d**, the corresponding SAED patterns of the obtained 1T′-$MoSe_2$ NSs.

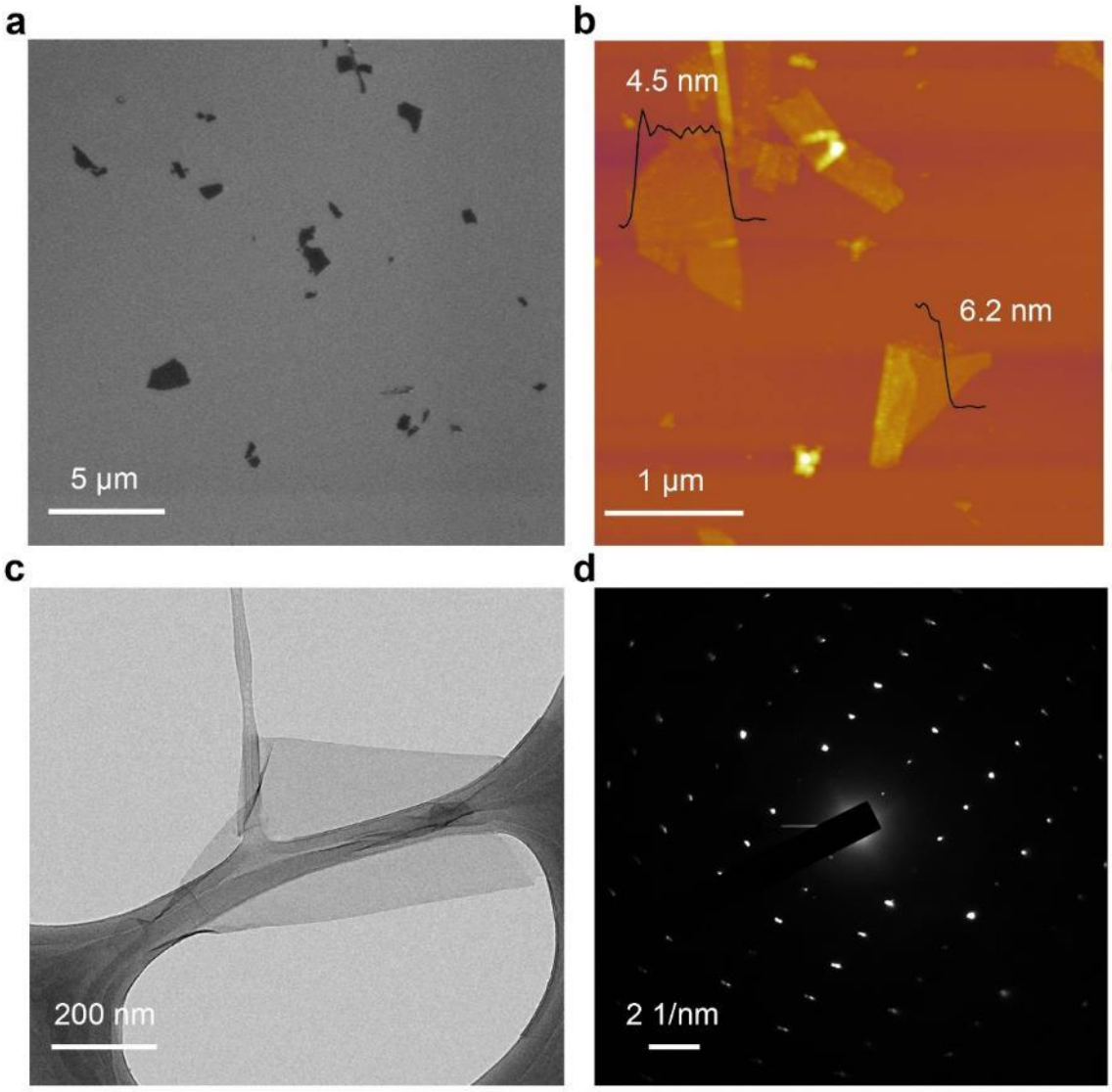

Figure 4.16 a, SEM, **b**, AFM, **c**, TEM, and **d**, the corresponding SAED patterns of the obtained 1T′-MoSSe NSs.

Apart from the metastable TMD nanosheets exfoliation, the reported liquid-phase exfoliation method in this project can also be introduced to many other layered materials exfoliations. From the one element materials Telluride (Te), two elements Boron Nitride (BN), Niobium diselenide ($NbSe_2$) and muti-elements materials $CuInP_2S_6$ which is synthesized by a newly developed CVT method. The TEM images showed the flake-like morphology and clean surface of the as-exfoliated nanosheets.

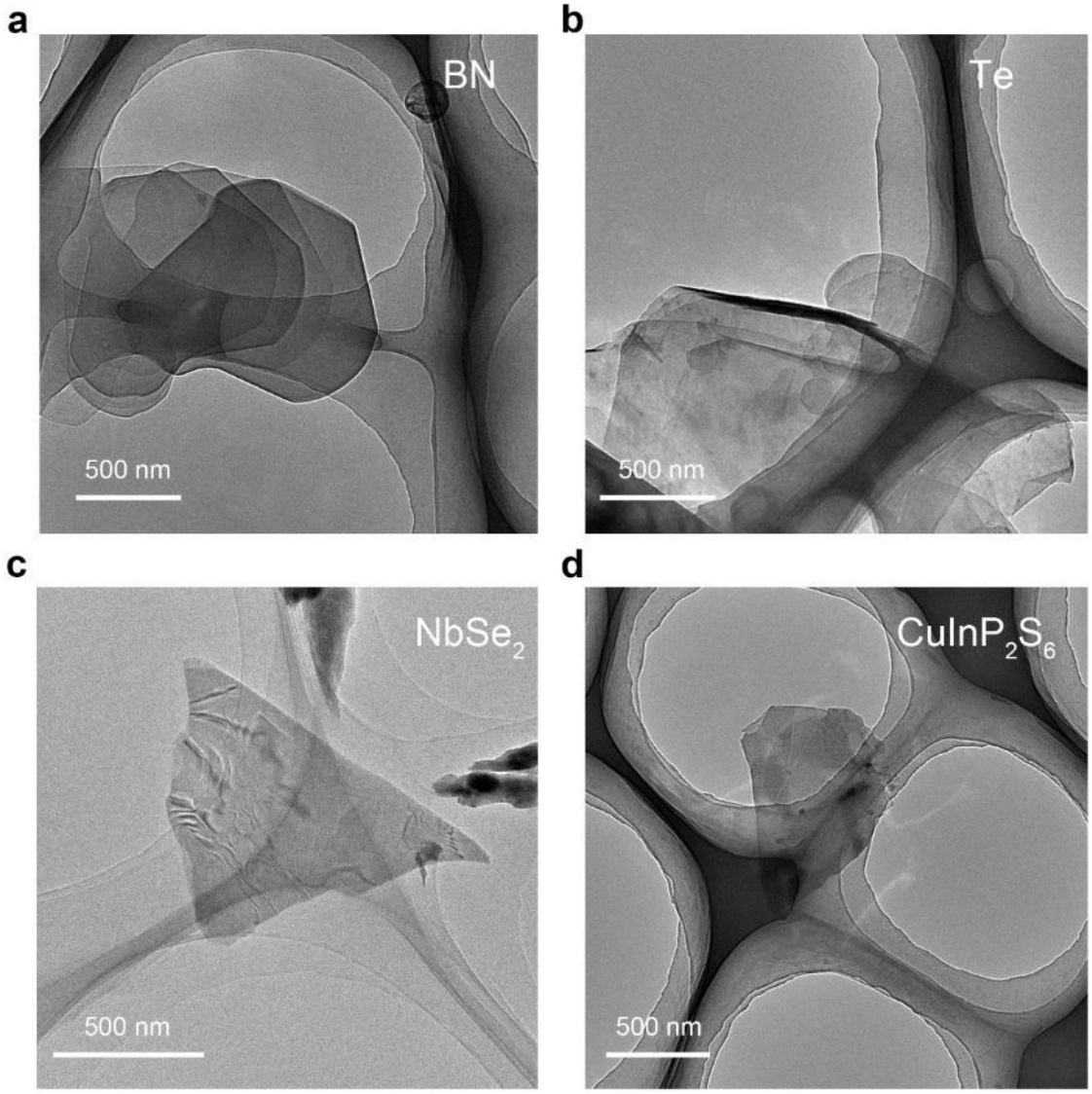

Figure 4.17 TEM images of the as-exfoliated **a**, Te, **b**, BN, **c**, $NbSe_2$, and **d**, $CuInP_2S_6$.

4.2.2 Electrochemical measurements

Previous studies demonstrated that the metallic phase MoS_2 nanosheets exhibited dramatically enhanced HER catalysis compared with the 2H-MoS_2 (REF[5]). However, the traditional lithium induced chemical exfoliation resulted in a mixture phase of 1T, 1T′ and 2H phase in the obtained MoS_2 layers. The HER electrocatalytic property of high purity 1T′-MoS_2 and 2H-MoS_2 nanosheets remains unclear. In this project, high purity 1T′-MoS_2

and 2H-MoS_2 nanosheets are prepared from bulk materials by the newly developed liquid-phase exfoliation method. As a proof-of-concept application, the sample is tested for electrocatalytic HER. Then the HER performance is then measured as mentioned before in Chapter 3. Impressively, the 1T′-MoS_2 nanosheets achieved a lower overpotential of 212 mV at current densities of 10 mA cm^{-2}, while the 2H counterparts showed a much higher overpotential 363mV (Figure 4.18 a). The corresponding Tafel slope of 1T′-MoS_2 nanosheets is 140 mV dec^{-1} (Figure 4.18 b), while the Tafel slope of 2H-MoS_2 nanosheets is 186.2 mV dec^{-1}. The big differences between the overpotential at 10 mA cm^{-2} and Tafel slope of the nanosheets in two different phases suggesting that phase is very important in determining the electrocatalytic properties.

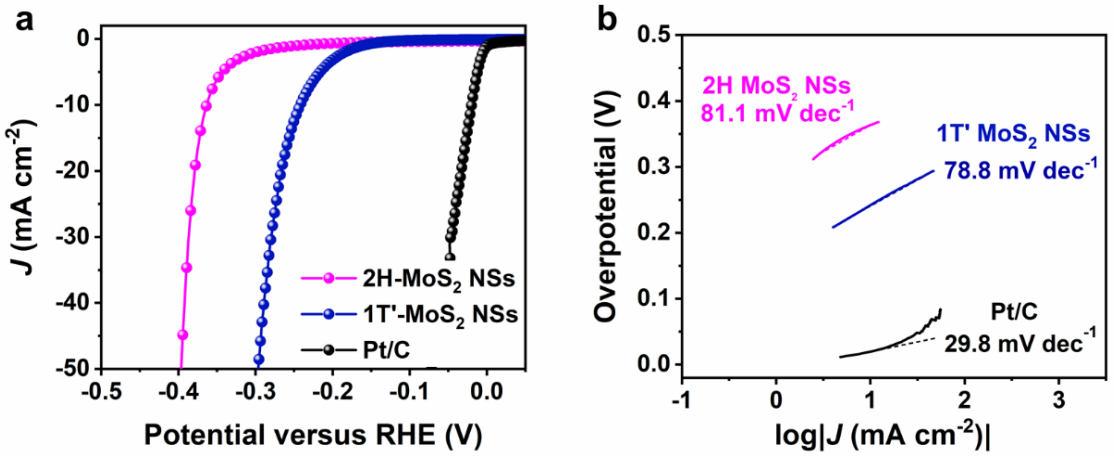

Figure 4.18 Electrocatalytic HER performance of 1T′-MoS_2 and 2H-MoS_2 nanosheets. **a**, Polarization curves and the **b**, corresponding Tafel plots of 1T′-MoS_2 and 2H-MoS_2 nanosheets in comparison to commercial Pt/C catalysts.

To understand the superior HER activity of 1T′-MoS_2 NSs, the electrochemical impedance spectroscopy (EIS) plots of 1T′-MoS_2 NSs and 2H-MoS_2 NSs were recorded. The semi-metallic 1T′-MoS_2 NSs exhibit an apparently smaller charge transfer resistance (R_{ct}) as compared with the semiconducting 2H-MoS_2 NSs, resulting in a faster electron-transfer process and better HER kinetics of 1T′-MoS_2 NSs. Such results illustrate that that 1T′-MoS_2 is suitable to be used as support for HER electrocatalysts. The electrical conductivity

1T′-MoS_2 and 2H-MoS_2 nanosheets are also measured as shown in Figure 4.19b. the 1T′-MoS_2 and 2H-MoS_2 films were prepared by the vacuum filtration method[16] on Millipore PVDF filtration paper with a diameter of 47 mm and a pore size of 0.22 μm. The current of 1T′-MoS_2 film is remarkably higher than that of 2H-MoS_2 film in the sweeping voltage of -0.1 to 0.1 V, indicating a greatly enhanced conductivity of 1T′-MoS_2. The much better HER performance of 1T′-MoS_2 NSs can also be attributed to the excellent conductivity of the 1T′-MoS_2.

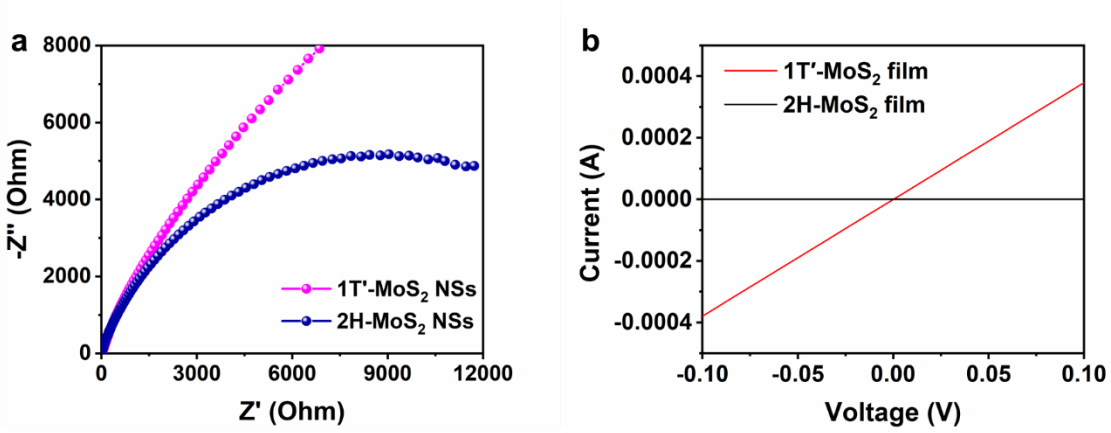

Figure 4.20 a, EIS spectra of 1T′-MoS_2 NSs and 2H-MoS_2 NSs. **b**, Current-voltage (I-V) characteristic curves of 1T′-MoS_2 and 2H-MoS_2 films.

References

1 Voiry, D. *et al.* Enhanced catalytic activity in strained chemically exfoliated WS_2 nanosheets for hydrogen evolution. *Nat. Mater.* **12**, 850-855 (2013).

2 Bonaccorso, F. *et al.* 2D materials. Graphene, related two-dimensional crystals, and hybrid systems for energy conversion and storage. *Science* **347**, 1246501 (2015).

3 Lin, Z. *et al.* Solution-processable 2D semiconductors for high-performance large-area electronics. *Nature* **562**, 254-258 (2018).

4 Manzeli, S., Ovchinnikov, D., Pasquier, D., Yazyev, O. V. & Kis, A. 2D transition metal dichalcogenides. *Nature Reviews Materials* **2** (2017).

5 Chhowalla, M. *et al.* The chemistry of two-dimensional layered transition metal dichalcogenide nanosheets. *Nat. Chem.* **5**, 263-275 (2013).

6 Coleman, J. N. *et al.* Two-dimensional nanosheets produced by liquid exfoliation of layered materials. *Science* **331**, 568-571 (2011).

7 Zeng, Z. *et al.* Single-layer semiconducting nanosheets: high-yield preparation and device fabrication. *Angew. Chem. Int. Ed. Engl.* **50**, 11093-11097 (2011).

8 Eda, G. *et al.* Photoluminescence from chemically exfoliated MoS_2. *Nano Lett.* **11**, 5111-5116 (2011).

9 Matte, H. S. *et al.* MoS_2 and WS_2 analogues of graphene. *Angew. Chem. Int. Ed.* **49**, 4059-4062 (2010).

10 Zhang, X., Lai, Z., Tan, C. & Zhang, H. Solution-processed two-dimensional MoS_2 nanosheets: Preparation, hybridization, and applications. *Angew. Chem. Int. Ed.* **55**, 8816-8838 (2016).

11 Yu, Y. *et al.* High phase-purity 1T′-MoS_2- and 1T′-$MoSe_2$ -layered crystals. *Nat. Chem.* **10**, 638-643 (2018).

12 Liu, L. *et al.* Phase-selective synthesis of 1T′ MoS_2 monolayers and heterophase bilayers. *Nat. Mater.* **17**, 1108-1114 (2018).

13 Splendiani, A. *et al.* Emerging photoluminescence in monolayer MoS_2. *Nano Lett.* **10**, 1271-1275 (2010).

14 Nam, G. H. *et al.* In-plane anisotropic properties of 1T′-MoS_2 layers. *Adv. Mater.* **31**, e1807764 (2019).

15 Li, H. *et al.* From bulk to monolayer MoS_2: Evolution of raman scattering. *Adv. Funct. Mater.* **22**, 1385-1390 (2012).

16 Withers, F. *et al.* Heterostructures produced from nanosheet-based inks. *Nano Lett.* **14**, 3987-3992 (2014).

Chapter 5

Pt nanoclusters supported on 1T′-MoS_2 nanosheets for highly efficient hydrogen production

Developing efficient and durable electrocatalysts is a promising way towards electrochemical hydrogen evolution reaction (HER). However, it is challenging to stabilize the nanostructured noble metal catalysts while simultaneously maintaining their high activities. Herein, we report that high purity 1T'-MoS_2 nanosheets can serve as an excellent support to host the platinum nanoclusters (Pt/1T'-MoS_2) towards highly efficient hydrogen evolution. Importantly, when used as a catalyst, the Pt/1T'-MoS_2 exhibits excellent catalytic activity towards HER with a small overpotential of ~30 mV at a current density of 50 mA cm^{-2} and TOF of 11.3 H_2 s^{-1}, outperforming the commercial Pt/C catalyst (71 mV at 50 mA cm^{-2}, a TOF value of 3.17 H_2 s^{-1} at 30 mV) showing great potential in practical application.

5.1 Introduction

Developing efficient and durable electrocatalysts towards electrochemical hydrogen evolution reaction (HER) is a promising way to solve the global environmental and energy crisis[1-3]. Platinum is the best electrocatalyst for the HER. However, the massive use of Pt is severely hampered by its scarcity and high cost. Therefore, improving the Pt atom-utilization efficiency while boosting the catalytic activity per atom is essential for HER[4]. The highly dispersed Pt nanoclusters catalysts are regarded as the most promising candidate. However, the aggregation tendency of Pt nanoclusters during both the synthetic and electrocatalytic process presents great difficulty in achieving high loading of Pt nanoclusters catalysts while maintained the high stability. Currently developed Pt-based electrocatalysts suffer from orders of magnitude lower current density and poor stability than the practical electrolyzer (>1000 mA cm^{-2}, hundreds of hours stability)[5]. Stabilizing the Pt nanoclusters by appropriate supporting substrates might be an effective way to achieve ultrahigh current density as well as exceptional stability.

Traditionally, the design and synthesis of catalyst substrate mainly focus on some complicated processes such as defects engineering, porosity enhancing, surface functionalizing, etc. In addition, the reported catalysts exhibited either low Pt loading to ensure the atomic dispersion or low Pt atom utilization due to the aggregation, thus retarded the unleashing of intrinsically high HER activity of Pt nanoclusters. The emerging phase engineering strategy paves a new effective way to tailor the structure and property of the substrate[6,7]. Yet almost no research focused on investigating the role of crystal phase in stabilizing nanoclusters. As a typical polyphase material, two-dimensional (2D) MoS_2 can crystallize in 2H, 1T and 1T′ phases with different electronic structures and functionality. With its high specific area, ultrathin nature, and high conductivity, 1T and 1T′-MoS_2 nanosheets served as an ideal platform to host nanoclusters with improved catalytic performance. However, the metastable nature of 1T and 1T′ phase resulted in the coexistence of 2H-MoS_2 within the obtained 1T and 1T′-MoS_2 nanosheets. The mixed phase nature makes it formidable to unravel the role of the crystal phase in determining the growth and stabilization of nanoclusters. Furthermore, the poor conductivity and

electrochemical inert basal plane of 2H-MoS_2 greatly suppressed the HER performance of the developed 1T or 1T′-MoS_2 based catalysts. Therefore, to construct noble metal-MoS_2 hybrids using the high phase purity 1T- or 1T′-MoS_2 NSs as templates could be an effective way to develop HER electrocatalysts with improved performance.

In this contribution, we report the preparation of 1T′-MoS_2 nanosheets with high phase purity which can effectively immobilize Pt nanoclusters (Pt/1T′-MoS_2) and exhibited superior HER performance. The strong interaction between 1T′ phase MoS_2 and Pt atom endowed Pt/1T′-MoS_2 with a high activity, high stability towards HER. The Pt/1T′-MoS_2 showed excellent HER activity (reaching 10, and 50 mA cm^{-2} current density at only 10 and 30 mV overpotential, respectively), outperforming commercial Pt/C catalysts and most of the previously reported electrocatalysts. The exceptional performance can be ascribed to the synergetic effect between highly conductive 1T′-MoS_2 substrate and Pt nanoclusters active sites with high intrinsic activity. The superior catalytic performance of Pt/1T′-MoS_2 highlights the significance of crystal phase for structure and property tailoring towards promising applications.

5.2 Results and Discussions

5.2.1 Phase-directing epitaxy growth of Pt and characterization

The high phase purity 1T′-MoS_2 and 2H-MoS_2 NSs offered ideal platforms for studying the phase-property relationship. After the 1T′-MoS_2 and 2H-MoS_2 NSs were prepared and transferred in water, the platinum (Pt) metal nanoclusters were synthesized in situ on the MoS_2 surface. K_2PtCl_4 was used as Pt precursor, while photochemical reduction method was applied with ethanol as a sacrificial agent and at an extremely mild condition to facilitates the epitaxy growth (see the detailed synthetic methods in the Chapter 3), the Pt loading is controlled at 10 wt% (identified by ICP result in Table 1) to make a clear comparison.

Table 5.1 ICP-OES results and the corresponding Pt mass loadings in Pt/2H-MoS_2 and Pt/1T′-MoS_2.

Sample	Mo Concentration (ppm)	Pt Concentration (ppm)	Pt wt%
Pt/2H-MoS_2	6.760	1.190	9.6
Pt/1T′-MoS_2	7.757	1.434	10.0

The transmission electron microscopy (TEM) in Figure 5.1a showed that the Pt clusters dispersed uniformly on 1T′-MoS_2 and 2H-MoS_2 nanosheets surfaces, with the similar average size of 0.9±0.4 nm (Figure 5.1b inset). Using the ICP-OES analysis, the loading amount of Pt on 2H-MoS_2 NSs is 10.0 wt% (Table 5.1). The SAED patterns of a Pt/1T′-MoS_2 (Figure 5.1c) showing orthorhombic lattice structure indicated 1T′ phase of MoS_2 substrate maintained after the Pt growth. There is no SAED patterns of Pt shown in Figure 5.1c, which implied that the Pt existed in the form of non-crystalline nanoclusters. A clear zig-zag chain of Mo atoms within 1T′-MoS_2 lattice can be clearly seen in the HAADF-STEM image in Figure 5.1d. The presence of bright spots assembly suggesting heavy constituent atoms in the structure, indicating the formation of Pt nanoclusters. In the magnified STEM image in Figure 5.1e, the bright spots of Pt atoms are clearly aligned with in the MoS_2 substrate, showing the epitaxial relationship between Pt nanoclusters and the 1T′-MoS_2. The atomically resolved image also showed a clear zigzag chains structure with a shortest Mo-Mo distance of 2.78 Å, indicating that the as-prepared MoS_2 NSs were in 1T′ phase. The high-resolution EDS elemental mapping images in Figure 5.1f confirmed that Pt clusters are well dispersed on the 1T′-MoS_2 nanosheets. As shown in Figure 5.1f, the Pt clusters mapping results are matched well with the bright spots in the STEM image confirming that the bright spots in STEM represent for the Pt clusters.

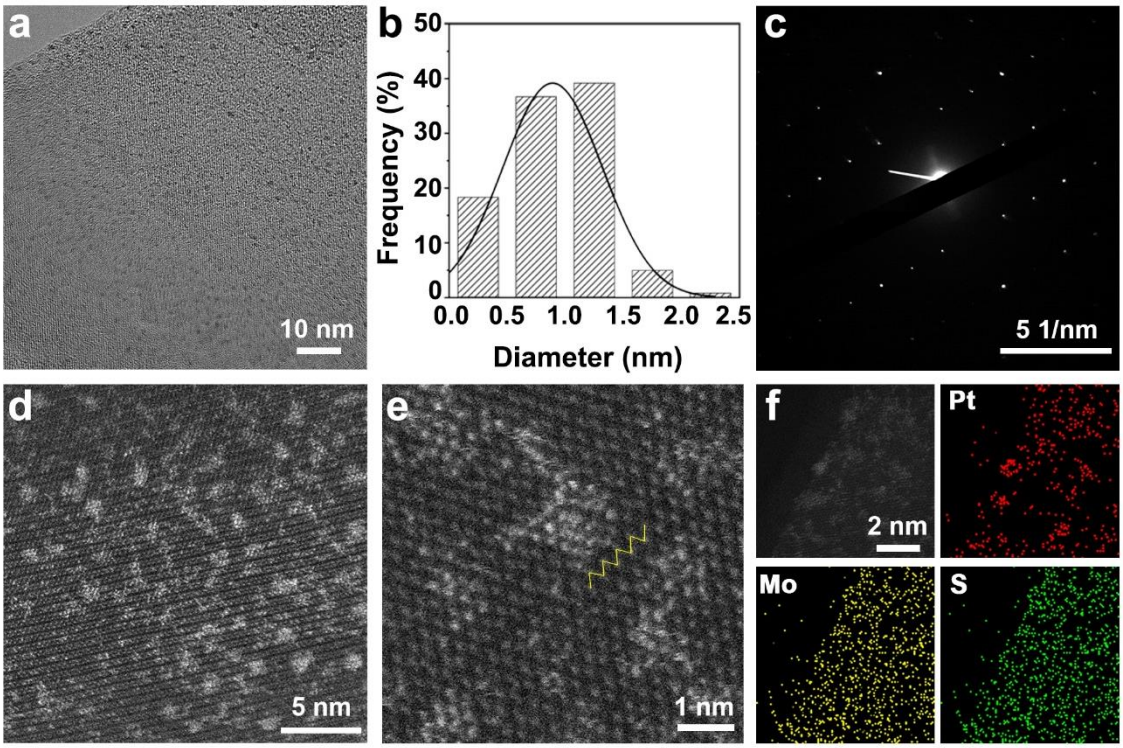

Figure 5.1 **a**, TEM image and. **b**, The diameter distribution of Pt nanoclusters with 100 nanoclusters counted. **c**, the corresponding SAED pattern of Pt/1T′-MoS_2. **d**, HAADF-STEM image and **d**, the magnified HAADF-STEM image of Pt/1T′-MoS_2. **e**, High resolution EDS mapping images the Pt/1T′-MoS_2.

The STEM image and the cross-sectional compositional line profiles in Figure 5.2 indicated further confirmed the elemental distribution of Pt/1T′-MoS_2. With the presence of a bright spot clusters in Figure 5.2b, a strong the Pt Lα1 peak presents in the EDS line scanning profile as shown in Figure 5.2c, which confirmed the presence of Pt clusters. The width of such Pt peak is around 1 nm which is in good accordance with the diameter of Pt clusters in Figure 5.1b.

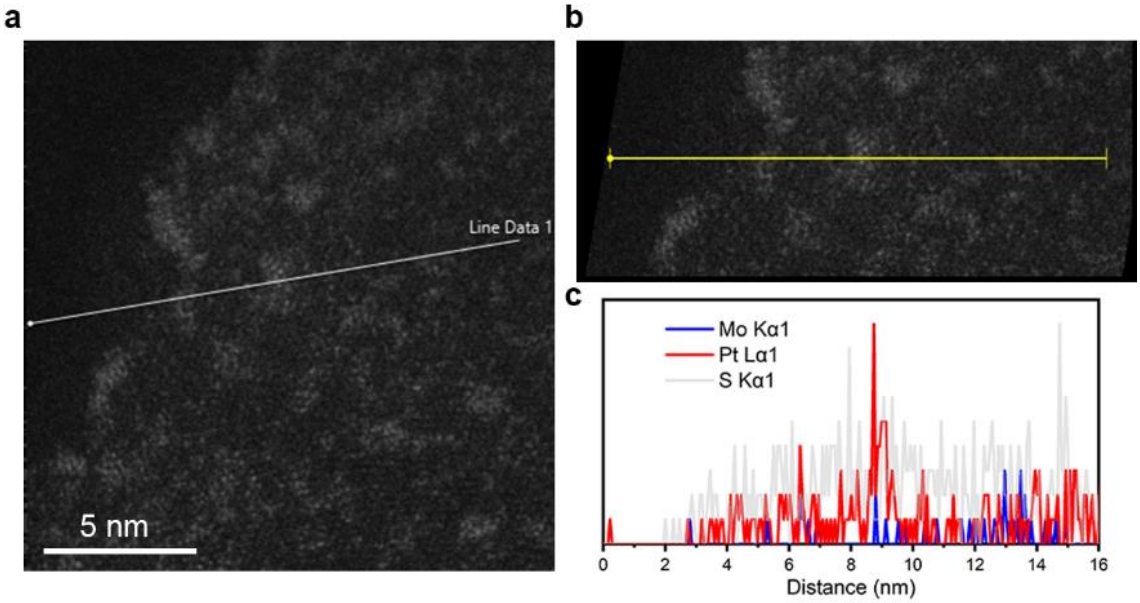

Figure 5.2 a, STEM image and the **b**,**c**, high resolution EDS line-scanning results of the Pt/1T′-MoS_2.

The large area EDS elemental mapping and spectrum in Figure 5.3 confirmed the presence of Mo, S and Pt elements and showed the uniform distribution of Pt clusters on MoS_2 nanosheets.

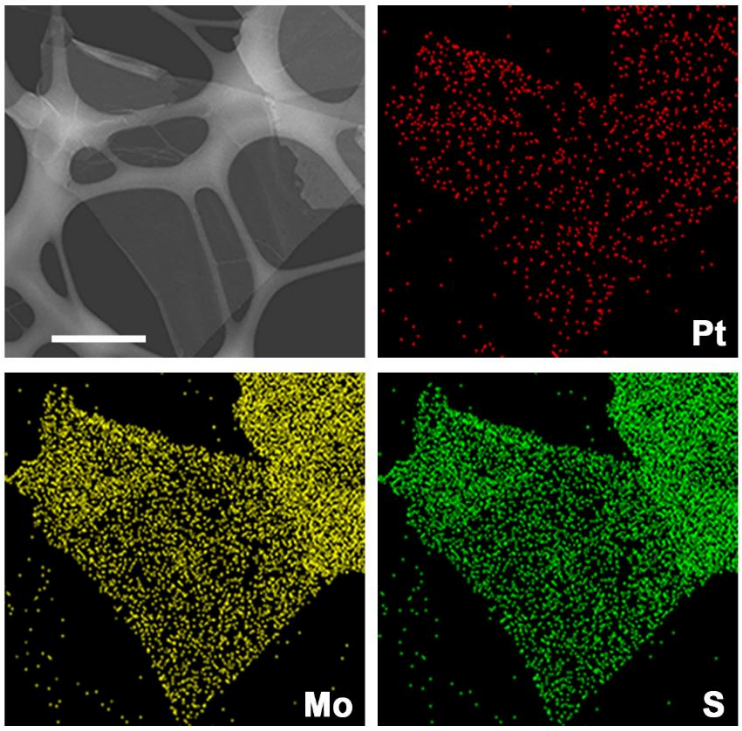

Figure 5.3 a, Large area EDS mapping results and **b**, the EDS spectrum of Pt/1T′-MoS_2.

After the growth of Pt on 2H-MoS_2, ultra-small PtNPs with an average size of 1.1±0.4 nm were obtained as shown in Figure 5.4 a. The SAED pattern (Figure 5.4b) shows two sets of diffraction spots, which can be assigned to the {111} planes of face-centered cubic (*fcc*) Pt and the {100} planes of 2H-MoS_2 with theoretical interlayer spacings of 2.27 Å and 2.74 Å, respectively. The diffraction spots of Pt align well with those of 2H-MoS_2, demonstrating that the ultra-small PtNPs are epitaxially grown on the 2H-MoS_2 NSs. Moreover, the (111) facets of PtNPs can be observed in the HAADF-STEM image (Figure 5.4c) with an average lattice spacing of 2.28 Å (Figure 5.4d), which are well aligned with the (100) planes of 2H-MoS_2 with a measured lattice spacing of 2.77 Å.

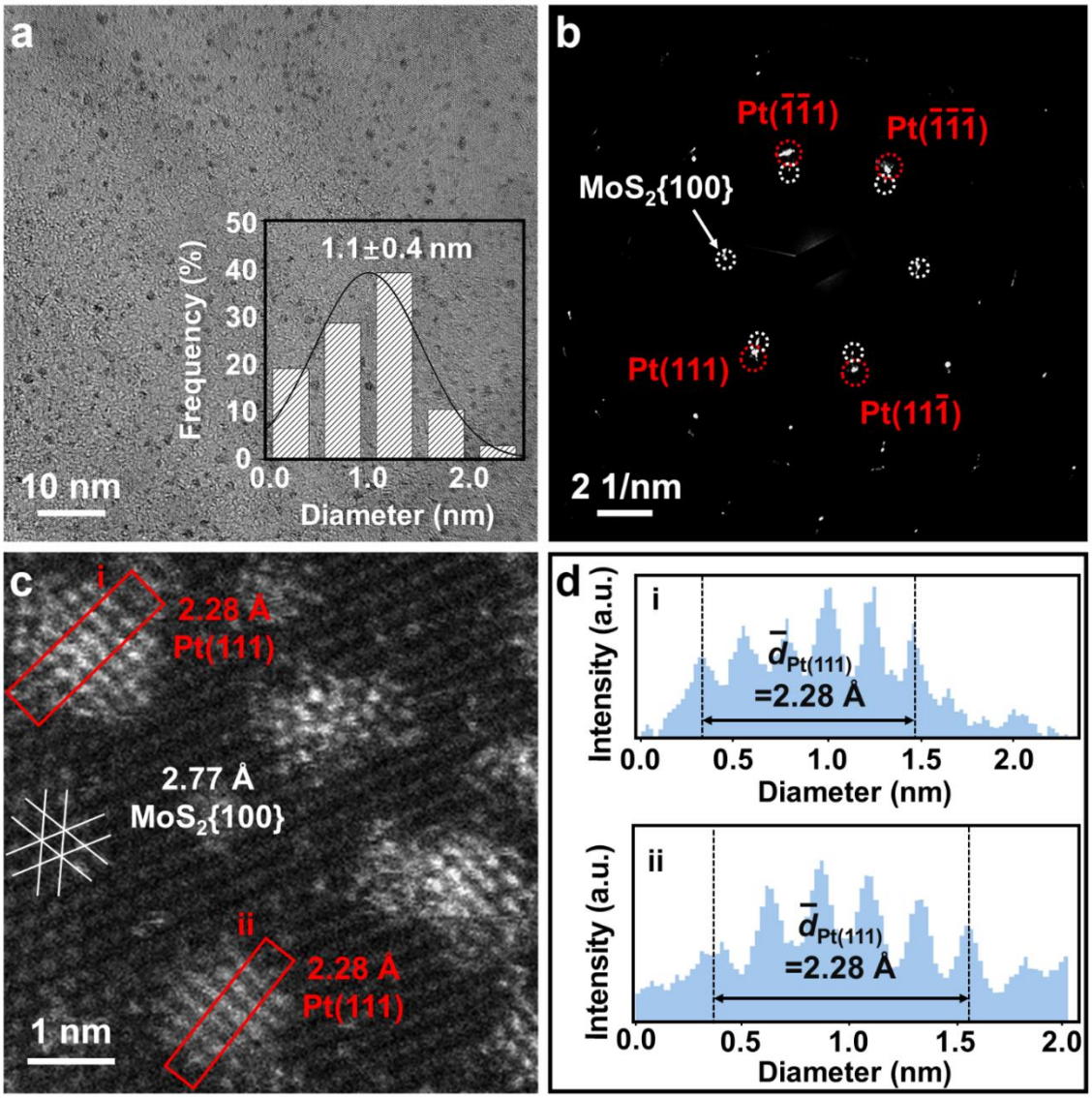

Figure 5.4 a, TEM image of Pt/2H-MoS_2. Inset: the diameter distribution histogram of PtNPs grown on 2H-MoS_2 NSs. **b**, SAED pattern of Pt/2H-MoS_2. **c**, HAADF-STEM image of Pt/2H-MoS_2. **d**, The corresponding line-scanning intensity profiles obtained from the areas **i** and **ii** in **c**, respectively. The average lattice spacings of Pt(111) planes were calculated to be 2.28 Å, which is consistent with the theoretical value of 2.27 Å.

Additionally, the EDS mapping results (Figure 5.5) confirm the homogeneous distribution of Pt, Mo, and S elements in the synthesized Pt/2H-MoS_2 hybrids. Using the ICP-OES analysis, the loading amount of Pt on 2H-MoS_2 NSs is 9.6 wt% (Table 5.1).

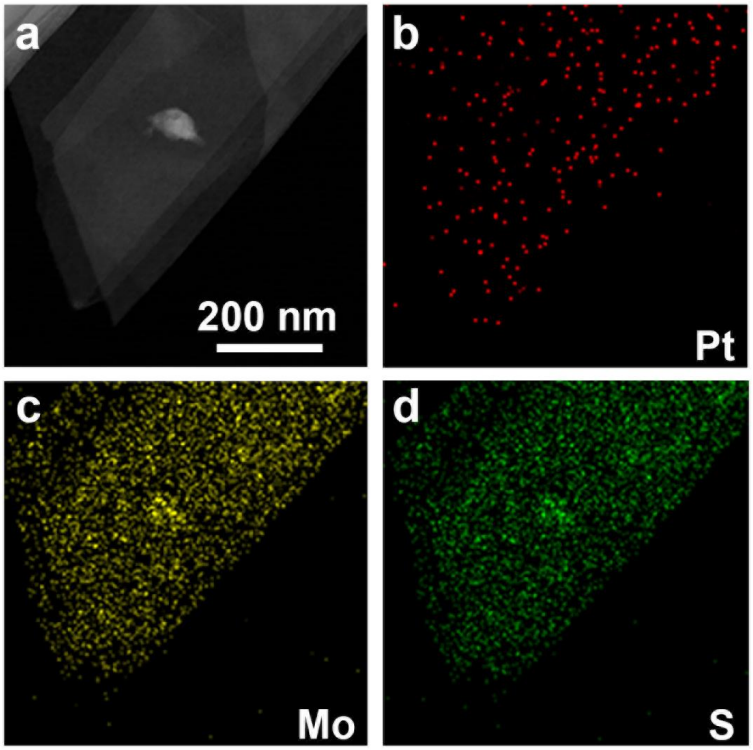

Figure 5.5 a, EDS mapping images and **b**, the EDS spectrum of Pt/2H-MoS_2.

The aforementioned results demonstrate that the Pt nanostructures with similar loading amount and similar particle size are grown on the 1T′-MoS_2 and 2H-MoS_2 NSs. The electronic states of Pt, Mo, and S elements are characterized by XPS, EXAFS results.

5.2.2 Electronic states of atoms in Pt/MoS_2 hybrid nanomaterials.

Furthermore, we characterized the electronic states Pt/1T′-MoS_2 and Pt/2H-MoS_2 by means of XPS. XPS was further used to reveal the valance states of Pt and Mo in the synthesized Pt-MoS_2 hybrids. As shown in Figure 5.6a, the fitted peaks of Pt 4$f_{7/2}$ located at 72.5 eV, 73.5 eV, and 74.8 eV can be assigned to $Pt^{\delta+}$, Pt^{2+}, and Pt^{4+}, respectively[31], suggesting the formation of Pt-S bond. On the contrary, a strong Pt^0 peak at 71.8 eV is observed in Pt 4*f* spectrum of Pt/2H-MoS_2 besides the $Pt^{\delta+}$, Pt^{2+}, and Pt^{4+} peaks, indicating the dominant metallic state of PtNPs grown on 2H-MoS_2. The XPS results demonstrate the different electronic states of Pt grown on 1T′-MoS_2 and 2H-MoS_2 templates. The valance states of MoS_2 templates after the growth of Pt were also characterized. As shown in Figure

5.6b, the Mo $3d_{5/2}$ and Mo $3d_{3/2}$ peaks of Pt/1T′-MoS_2 and Pt/2H-MoS_2 can be well assigned to 1T′-MoS_2 and 2H-MoS_2, respectively, which are consistent with the XPS results of the 1T′-MoS_2 and 2H-MoS_2 NSs (Figure 4.13a). The S 2*s* peaks of Pt/1T′-MoS_2 and Pt/2H-MoS_2 were also observed at 225.7 eV and 226.5 eV, respectively. These results confirm that no phase transition occurred in the 1T′-MoS_2 and 2H-MoS_2 templates after the growth of Pt, which is also confirmed by Raman spectra (Figure 5.7a).

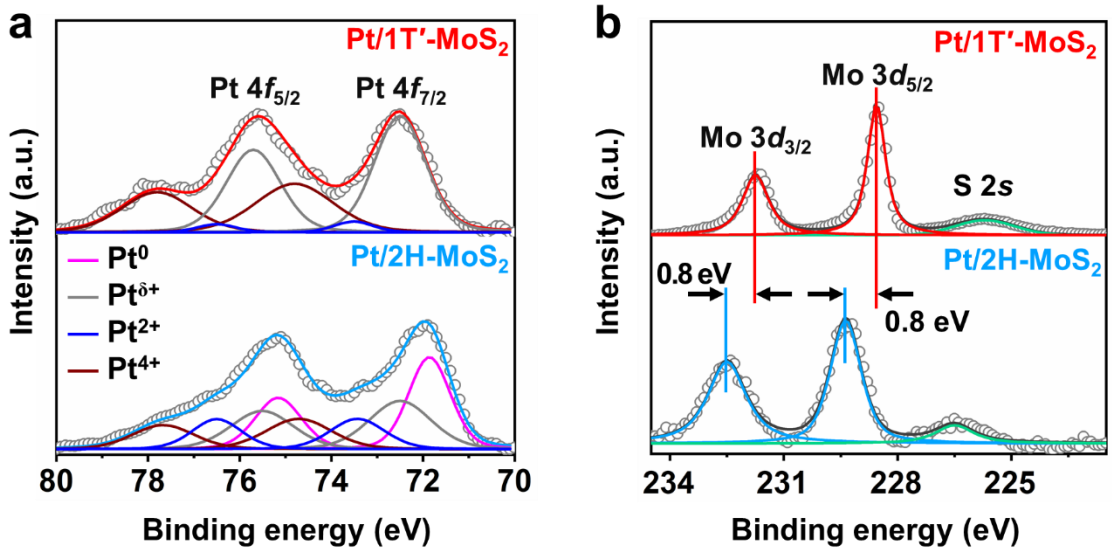

Figure 5.6 a, Pt 4*f*, and b, Mo 3*d* XPS spectra of Pt/1T′-MoS_2 and Pt/2H-MoS_2. The grey circles and the solid lines in (**a**,**b**) show the experimental XPS data and the corresponding deconvoluted spectra, respectively.

As shown in the Raman spectra of 1T′-MoS_2 NSs and Pt/1T′-MoS_2 (Figure 5.7a), all the Raman peaks of Pt/1T′-MoS_2 shift to higher wavenumbers compared to the 1T′-MoS_2 NSs. This result could be attributed to the interaction of 1T′-MoS_2 and the as-grown Pt (REF.[9,10]). Importantly, the characteristic peak of 2H-MoS_2 (E^1_{2g} located at 382.8 cm^{-1}) cannot be observed, indicating that no phase transition of 1T′ to 2H occurred after the growth of Pt on 1T′-MoS_2. As shown in Figure 5.7b, the phase of 2H-MoS_2 was also maintained after the grow of Pt to form the Pt/2H-MoS_2, although the Raman peaks of Pt/2H-MoS_2 slightly

shift to higher wavenumbers compared to the 2H-MoS_2 NSs which could also be ascribed to the interaction between the 2H-MoS_2 and PtNPs[9,10].

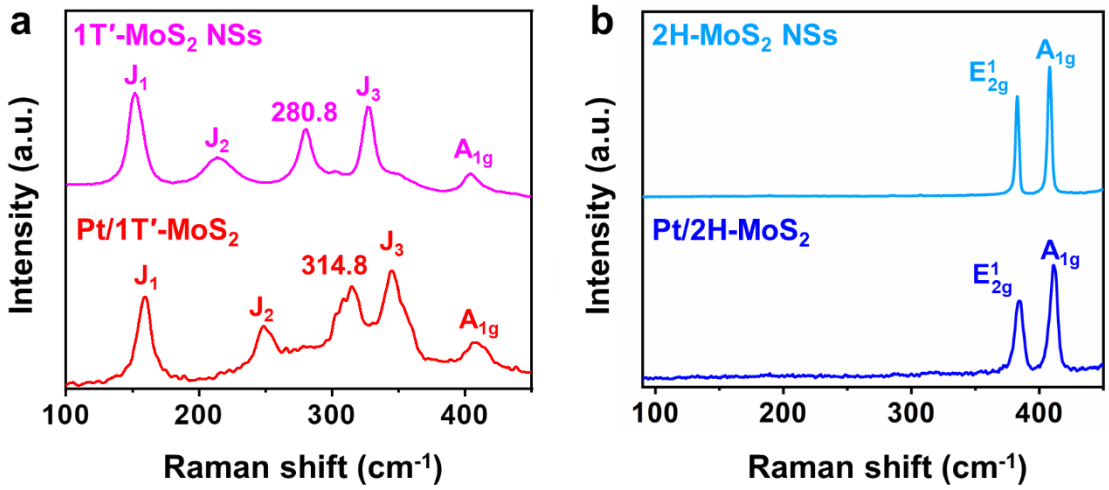

Figure 5.7 a, Raman spectra of 1T′-MoS_2 NSs and Pt/1T′-MoS_2. **b**, Raman spectra of 2H-MoS_2 NSs and Pt/MoS_2 NSs.

The local electronic structure of S element is characterized by S K-edge XANES spectrum. The S K-edge XANES spectra of Pt/1T′-MoS_2 and Pt/2H-MoS_2 are shown in Figure 5.8. The most obvious peaks of the S atoms in 1T′-MoS_2 locate at 2467 eV, 2469 eV and 2478 eV maintained almost unchanged after Pt atoms loading. The shoulder peak appears at 2467 eV arises from the electron of S *1s* transferred to unoccupied hybridized orbitals of S 3*p* and Mo 4*d*. The slight shift of white line intensity of Pt/1T′-MoS_2 towards the high energy compared with bare 1T′-MoS_2 implying an increase of the valence state of S atoms. The peaks of 2469 eV, 2477 eV, 2480 eV in the S Kedge XANES of Pt/2H-MoS_2 is in accordance with the reported 2H-MoS_2.

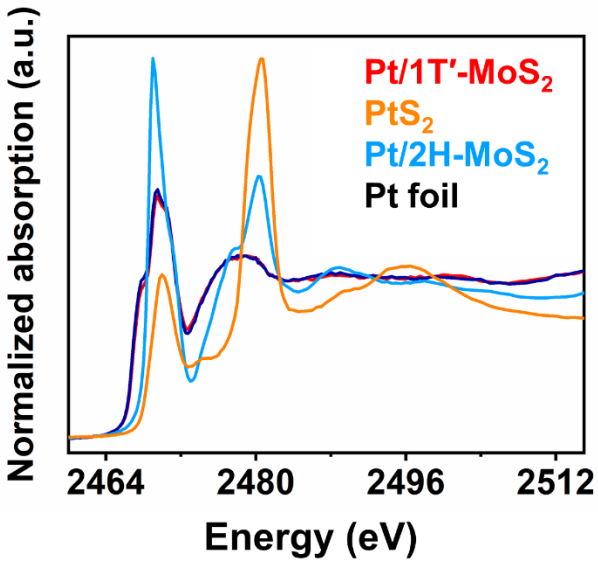

Figure 5.8 The S K-edge XANES spectra of Pt/1T′-MoS_2, commercial PtS_2, Pt/2H-MoS_2, and Pt foil.

5.2.3 Electrochemical HER evaluation of Pt/1T′-MoS_2.

Pt/1T′-MoS_2 and Pt/2H-MoS_2 hybrid nanomaterials were further used to study phase-dependent HER performance. For comparison, the catalytic performances of the commercial Pt/C (10 wt%) (Figure 5.9), 1T′-MoS_2 NSs (Figure 4.5), and 2H-MoS_2 NSs (Figure 4.11) were also evaluated. Figure 5.9 showed the characterization of commercial Pt/C catalysts. As shown in Figures 5.9a and b, the PtNPs grow uniformly on the carbon substrate with a diameter around 5 nm. The EDS spectrum and elemental mapping results in Figures 5.9c and d showed that the presence of PtNPs and the uniform distribution nature of Pt on the carbon substrate.

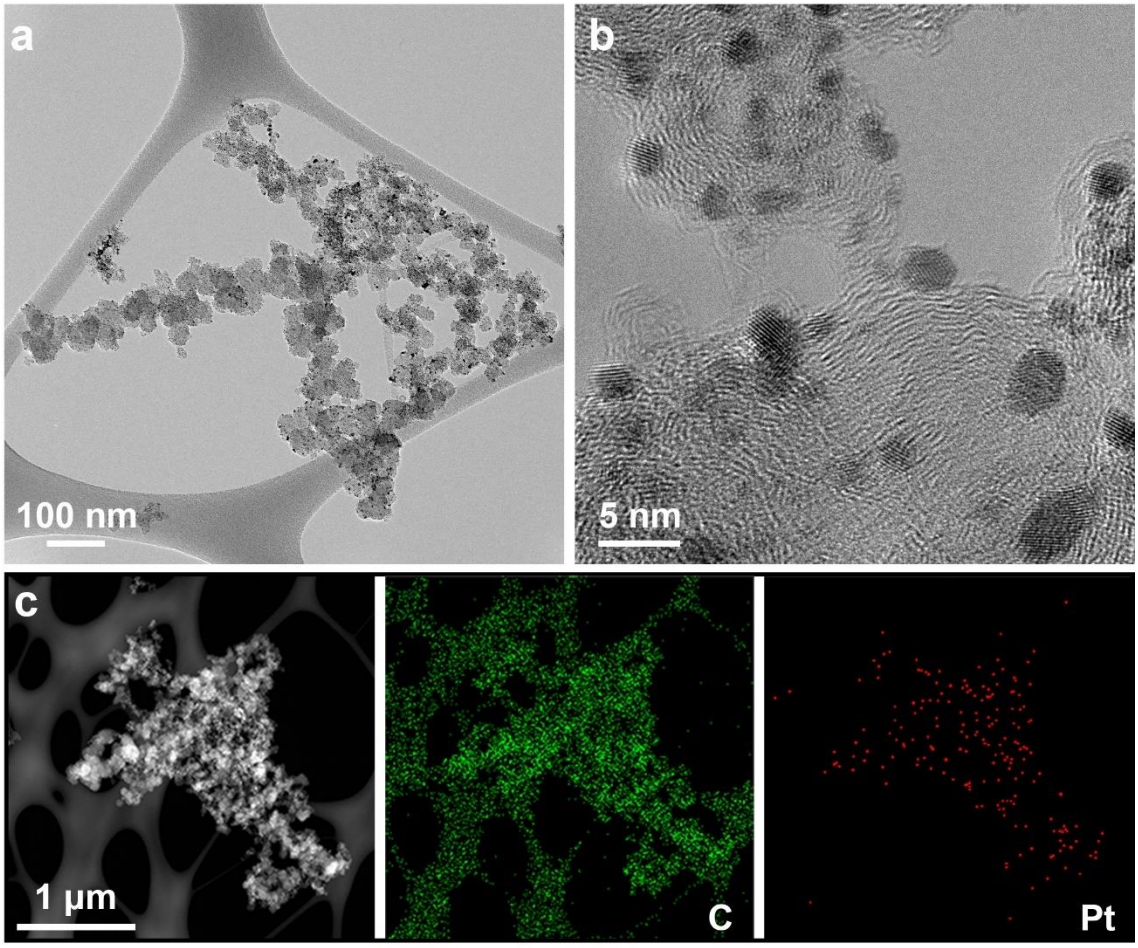

Figure 5.9 a, TEM image, **b**, HRTEM image, and **c**, STEM image and the corresponding EDS mappings of the commercial Pt/C catalysts.

As shown in Figure 5.11a, the Pt/1T′-MoS_2 exhibits an excellent activity with an overpotential of only 10 mV to reach a current density of 10 mA cm^{-2}. Such an overpotential is significantly lower compared to the Pt/2H-MoS_2 (113 mV@10 mA cm^{-2}) and commercial Pt/C (19 mV@10 mA cm^{-2}). Impressively, an ultralow overpotential of 30 mV is required for the Pt/1T′-MoS_2 to reach a current density of 50 mA cm^{-2}, which is also lower than that of commercial Pt/C (71 mV@50 mA cm^{-2}). Additionally, the Tafel slope (28.3 mV dec^{-1}) of the Pt/1T′-MoS_2 (Figure 5.10b) is dramatically smaller than that of Pt/2H-MoS_2 (139.5 mV dec^{-1}) and is similar to that of commercial Pt/C (29.8 mV dec^{-1}), revealing its rapid HER kinetics. Furthermore, the Pt/1T′-MoS_2 exhibits much higher mass

activities for HER than the commercial Pt/C in the whole investigated potential window (Figure 5.10c). Especially, the mass activity of Pt/1T′-MoS_2 at 40 mV overpotential was calculated as 6,814 A g_{Pt}^{-1}, which is ca. 2.66 times that of the commercial Pt/C (2,557 A g_{Pt}^{-1}). The aforementioned results demonstrate that the Pt/1T′-MoS_2 possesses a significantly enhanced activity for hydrogen generation in comparison with the commercial Pt/C. Importantly, the Pt/1T′-MoS_2 exhibits excellent stability during the HER process. The polarization curve shows no obvious degradation after 10,000 cyclic voltammetry cycles (Figure 5.10d). Moreover, a negligible variation in the current density of hydrogen evolution is observed after a 30-h test as revealed by the chronoamperometric curve (inset of Figure 5.10d).

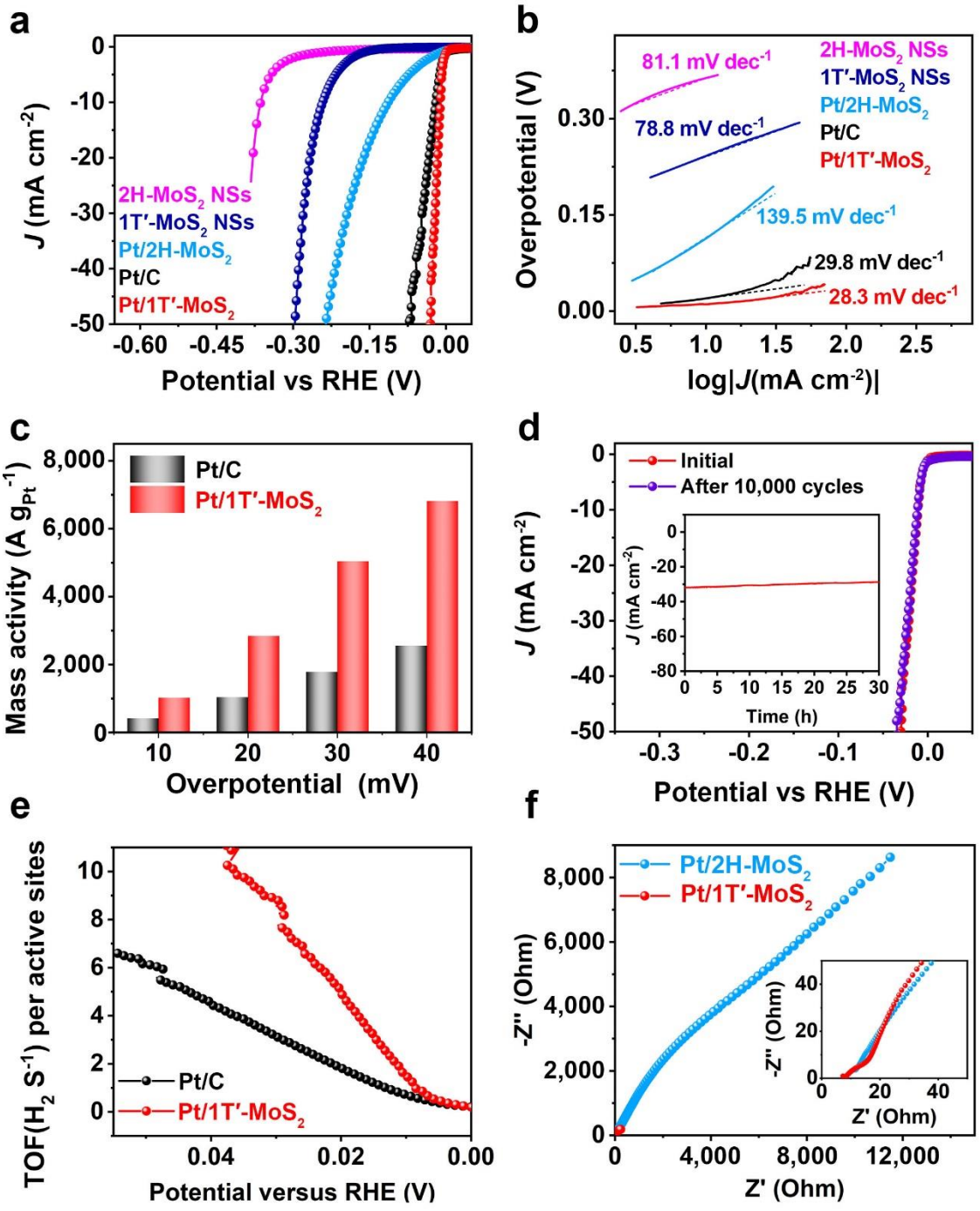

Figure 5.10 a, HER polarization curves of Pt/1T′-MoS_2, Pt/2H-MoS_2, 1T′-MoS_2 NSs, 2H-MoS_2 NSs, and commercial Pt/C electrocatalysts loaded on the glassy carbon electrode. The weights of 1T′-MoS_2 NSs, 2H-MoS_2 NSs and Pt/1T′-MoS_2 were kept the same (0.1 mg cm^{-2}). The mass loadings of Pt were kept the same (0.01 mg cm^{-2}) for Pt/1T′-MoS_2, Pt/2H-MoS_2 and Pt/C. **b**, Tafel plots of the catalysts derived from **a**. **c**, Mass activities of Pt/1T′-MoS_2 and commercial Pt/C. **d**,

Long-term stability test for Pt/1T′-MoS_2. The polarization curves were recorded before and after 10,000 potential cycles. Inset: the chronoamperometric test of Pt/1T′-MoS_2, showing that the current density remains stable over 30 h. **e**, Comparison of the TOF values of Pt/1T′-MoS_2 and Pt/C. **f**, EIS spectra of Pt/1T′-MoS_2 and Pt/2H-MoS_2, showing that the R_{ct} of Pt/1T′-MoS_2 is much lower than that of Pt/2H-MoS_2.

To evaluate the intrinsic activity of the Pt/1T′-MoS_2 catalyst, the turnover frequency (TOF) was calculated based on the ECSA results measured through the CO stripping method. As shown in Figure 5.10e, at the same overpotential, Pt/1T′-MoS_2 exhibits a much higher TOF value compared to Pt/C, indicating that the Pt nanoclusters on 1T′-MoS_2 have a much higher intrinsically activity in comparison with to catalyze hydrogen generation in comparison with the commercial Pt/C. At the overpotential of 30 mV, the TOF value of Pt/1T′-MoS_2 is 11.3 H_2 s^{-1}, which is three times higher than those of Pt/C (3.17 H_2 s^{-1}) respectively. Specifically, this value is also among the best of recently reported representative HER electrocatalysts in acid condition[9-12]. To understand the superior HER activity of Pt/1T′-MoS_2, the electrochemical impedance spectroscopy (EIS) plots of Pt/1T′-MoS_2, and Pt/2H-MoS_2 were then recorded. As shown in Figure 5.10f, Pt/1T′-MoS_2 exhibits an ultrasmall R_{ct} as compared with Pt/2H-MoS_2, resulting in an ultrafast electron-transfer process and superior HER kinetics. Such results indicate that the highly conductivity of the 1T′-MoS_2 NSs could be one of the key factors determining the superior HER performance of Pt/1T′-MoS_2. It is also worth mentioning that the activity of as-synthesized Pt/1T′-MoS_2 is among the best of reported HER electrocatalysts under acidic conditions (Table 5.2).

Table 5.2 Comparison of HER activities of some representative reported catalysts tested in 0.5 M H_2SO_4.

Catalysts	Metal loading (mg cm^{-2})	Metal weight percent	Overpotential (mV)@10 mA cm^{-2}	Tafel slope (mV dec^{-1})	Scan rate (mV s^{-1})	References
Pt/1T′-MoS_2	**0.01 (Pt)**	**10 wt%**	**10**	**28.3**	**5**	**This work**
Pt/C	**0.01 (Pt)**	**10 wt%**	**19**	**29.8**	**5**	**This work**
Pt single atoms/MoS_2	N/A	5.1 wt%	59	31	2	11
Pt doped 1T-MoS_2	N/A	3 wt%	140	57	50	12
K_2PtCl_4/N-doped carbon	0.0055 (Pt)	1.92 wt%	11	21	2	13
Pt single atoms/nitrogen-carbon framework	~0.00625 (Pt)	2.5 wt%	19	14.2	5	14
Pt single atoms decorated nanoporous $Co_{0.85}Se$	0.0204 (Pt)	1.03 wt%	55	37	2	15
Pt single atoms/$Mo_2TiC_2T_x$	0.012 (Pt)	1.2 wt%	30	30	5	16
Co single atoms/distorted 1T-MoS_2	N/A	3.54 wt %	42	32	N/A	17
Pd doped MoS_2	0.00222 (Pd)	~0.65 wt %	89	62	2	18
Pt single atoms/curved carbon	0.00168 (Pt)	0.33 wt%	38	35	5	19
Pt single atoms/MoS_2	0.018 (Pt)	1.7 wt%	150	96	2	20
Pt single atoms/graphene	0.00707 (Pt)	0.44 wt%	12	29.33	2	21
Pt-graphitic tubes-FeCo/Cu	0.0014 (Pt)	0.5 wt%	18	24	2	22
Ru/multi-walled carbon nanotubes	~0.0896 (Ru)	12.8 wt%	13	27	5	23
Rh_2P/N-doped carbon	0.07 (Rh)	N/A	9	26	5	24
PtNPs/MoS_2	0.027 (Pt)	36 wt%	80	40	2	25
Pt/TiS_2	N/A	N/A	70	40.6	2	26
Pt cluster/carbon spheres	0.0076 (Pt)	5.08 wt%	20	28.3	1	27

The superior electrocatalytic performance of Pt/1T′-MoS_2 can be attributed to the following reasons. Firstly, the high conductivity of the 1T′-MoS_2 substrate facilitates the electron transfer during the electrochemical HER process. 1T′-MoS_2 exhibited a much higher conductivity and apparently smaller charge transfer resistance (R_{ct}) as compared with 2H-MoS_2. The introduction of atomic dispersed Pt further reduced R_{ct} of Pt/1T′-MoS_2, resulted in an ultrafast electron-transfer process and superior HER kinetics. Secondly, the well-dispersed Pt nanoclusters provide abundant active sites for the electrochemical reaction. In addition, the TOF results (11.3 $H_2\ s^{-1}$ at 30 mV overpotential) indicated that the Pt nanoclusters on 1T′-MoS_2 surface possessed an ultrahigh intrinsic activity for HER, leading to a rapid formation and release of hydrogen molecule. Therefore, the high HER activity is a synergistic effect of the highly conductive 1T′-MoS_2 substrate and highly active Pt nanoclusters.

5.3 Conclusions

By using the 1T′ and 2H-MoS_2 nanosheets as templates, the crystal phase effect in tailoring the structure and properties of TMD-based hybrid nanomaterials is unraveled. Non-crystalline Pt nanoclusters can be stabilized on 1T′-MoS_2, while 2H-MoS_2 facilitates the growth of highly crystalline PtNPs during the same photoreduction process. More importantly, the Pt/1T′-MoS_2 exhibited superior HER activity and long-term stability outperforming commercial Pt/C. Our phase engineering strategy paves an avenue to construct hybrid nanomaterials with desired structures, unique properties, and excellent performance towards various promising applications.

Reference

1 Liu, J., Ma, Q., Huang, Z., Liu, G. & Zhang, H. Recent Progress in Graphene-Based Noble-Metal Nanocomposites for Electrocatalytic Applications. *Advanced Materials*, 2018, **1800696**, 1800696.

2 Li, C. & Baek, J. B. Recent Advances in Noble Metal (Pt, Ru, and Ir)-Based Electrocatalysts for Efficient Hydrogen Evolution Reaction. *ACS Omega*, 2019.

3 Liu, G. *et al.* Synthesis of RuNi alloy nanostructures composed of multilayered nanosheets for highly efficient electrocatalytic hydrogen evolution. *Nano Energy*, 2019, **66**, 104173.

4 Ji, S. *et al.* Chemical Synthesis of Single Atomic Site Catalysts. *Chemical Reviews*, 2020, 10.1021/acs.chemrev.9b00818.

5 Zhu, C., Fu, S., Shi, Q., Du, D. & Lin, Y. Single-Atom Electrocatalysts. *Angewandte Chemie International Edition*, 2017, **56**, 13944-13960.

6 Chen, Y. *et al.* Phase engineering of nanomaterials. *Nature Reviews Chemistry*, 2020, 1-14.

7 Ge, Y. *et al.* Two-Dimensional Nanomaterials with Unconventional Phases. *Chem*, 2020, **6**, 1237-1253.

8 Harada, M. & Einaga, H. Formation Mechanism of Pt Particles by Photoreduction of Pt Ions in Polymer Solutions. *Langmuir*, 2006, **22**, 2371-2377.

9 Fang, S. *et al.* Uncovering near-free platinum single-atom dynamics during electrochemical hydrogen evolution reaction. *Nature Communications*, 2020, **11**, 1029.

10 Jiang, K. *et al.* Single platinum atoms embedded in nanoporous cobalt selenide as electrocatalyst for accelerating hydrogen evolution reaction. *Nature Communications*, 2019, **10**, 1743.

11 Zhang, J. *et al.* Single platinum atoms immobilized on an MXene as an efficient catalyst for the hydrogen evolution reaction. *Nature Catalysis*, 2018, **1**, 985-992.

12 Qi, K. *et al.* Single-atom cobalt array bound to distorted 1T MoS_2 with ensemble effect for hydrogen evolution catalysis. *Nature Communications*, 2019, **10**, 1-9.

Chapter 6

Conclusion and future work

This chapter gives a general discussion on this thesis by summarizing the significance and novelties of the research work. Firstly, this thesis provides a facile electrochemical exfoliation method to prepare metastable solution-processable 1T' TMD nanosheets with high phase purity and high quality. The successful exfoliation of metastable TMD nanosheets offers a great opportunity towards a detailed research on the metastable phase of TMD and the phase-dependent properties relationship. In this thesis, noble metal Pt is grown on the 2H-and 1T'-MoS_2 nanosheets which showed different growth behavior and different functionality. The Pt/1T'-MoS_2 exhibited superior catalytic performance much better than the Pt/2H-MoS_2, even outperforming the Pt/C. This work emphasizes the significance of crystal phase in determining the property and functionality of nanomaterials and pave a new way towards designing highly efficient electrocatalysts towards various application.

6.1 General Discussion

6.1.1 Discussion on the preparation of high phase purity 1T′-TMD nanosheets

A facile, large-scale and solution-processed method to prepare 1T′-TMD nanosheets with high phase purity, and high quality is developed. The obtained 1T′-TMD nanosheets in this thesis include 1T′-MoS_2, 1T′-$MoSe_2$ and the alloyed TMDs 1T′-MoSSe with high crystallinity and ultrathin thickness. In addition, such a method can be extended to prepare many other kinds of nanosheets from layered nanomaterials such as Te, Bn, $NbSe_2$, and $CuInP_2S_6$ showing great generality. The obtained 1T′-MoS_2 exhibits orders of magnitude higher conductivity and a much higher HER activity than the 2H counterpart[1].

The novelty of this work is listed briefly:

1. Carefully design of the electrochemical intercalation process. The metastable nature of 1T′-TMD greatly inhibits the electrochemical intercalation method to get 1T′-TMD nanosheets from their bulk crystals. One of the most important reasons is that the electron injection to the MoS_2 materials is quite high[2]. When the injection of electrons exceeds about 0.29 electrons for MoS_2 unit, a phase transition will occur inside the MoS_2. Therefore, we carefully choose the THAB molecule as the intercalation agent, which will only inject limited number of electrons per MoS_2 unit. In addition, the potassium intercalated TMDs instead of the 1T′-TMD crystals are used as precursors. In this case, the potassium could stabilize the 1T′ structure of the TMDs nanomaterials before the intercalation process. In the meantime, the intercalation process will remove the K ion from the TMDs lattice as proved by the experimental results. Owing to the careful design of the electrochemical intercalation process, a series of 1T′-TMDs nanosheets can be easily prepared from their bulk crystals with high quality, which is also in accordance with our hypothesis at the beginning of this thesis.

2. A general electrochemical intercalation process towards the preparation of nanosheets from the layered crystals. Upon successfully developing the THAB assisted electrochemical intercalation method, a variety of different layered crystals are used as

precursors to obtain different nanosheets materials. As confirmed by the experimental results, a wide range of layered crystals can be exfoliated by such a method. In addition, the preliminary results show that the layered organic materials such as MOF, COF nanomaterials can also be exfoliated by such a method. The above results indicate the generality of the newly developed method and prove that such a method can be used to further exfoliate many other layered crystals into nanosheets structure.

3. A direct comparison showing the phase-dependent properties of TMDs. After exfoliation, the conductivity and the HER performance of 1T′-MoS_2 and 2H-MoS_2 nanosheets are compared directly. 1T′-MoS_2 shows a much enhanced conductivity and HER activity compared with the 2H-MoS_2 showing the phase-dependent properties.

6.1.2 Discussion on Pt nanoclusters supported on 1T′-MoS_2 nanosheets for highly efficient hydrogen production

By using the 1T′- and 2H-MoS_2 nanosheets as templates, the crystal phase effect in tailoring the structure and properties of TMD-based hybrid nanomaterials is investigated in detail. Non-crystalline Pt nanoclusters can be grown and stabilized on 1T′-MoS_2, while 2H-MoS_2 facilitates the growth of crystalline Pt nanoparticles during the same photoreduction process. More importantly, the Pt/1T′-MoS_2 exhibited superior HER activity and long-term stability outperforming commercial Pt/C owing to the synergistic effect between the conductive 1T′-MoS_2 and the Pt nanoclusters.

The novelty of this work is listed briefly:

1. Crystal phase effect in TMDs nanosheets. By using the same exfoliation method, 1T′ and 2H-MoS_2 nanosheets are prepared and used as template. Owing to the different atomic arrangement of Mo and S on the surface of the nanosheet, the MoS_2 should direct different growth behavior of the second deposit nanomaterials as hypothesized at the beginning of the thesis. The experimental results further confirm the hypothesis. Owing to the different symmetry, the Pt which grows in situ on the 1T′-MoS_2 nanosheets exhibits the non-crystalline structure. While on the 2H-MoS_2 nanosheets, well-crystalline Pt nanoparticles

are formed. Such results indicate that the crystal phase plays a key role in determining the growth behavior of the Pt nanostructure.

2. Synergetic effect in the enhancement of HER activity. Pt/1T′-MoS_2 exhibited superior HER activity and long-term stability outperforming commercial Pt/C. The superior electrocatalytic performance of Pt/1T′-MoS_2 can be attributed to the following reasons, which is the high conductivity and the charge transfer resistance of the 1T′-MoS_2 substrate, and the ultrahigh intrinsic activity of Pt non-crystalline nanoclusters for HER. Therefore, the high HER activity is a synergistic effect of the highly conductive 1T′-MoS_2 substrate and highly active Pt nanoclusters.

6.2 Future work

6.2.1 Preparation of TMD nanosheets with novel phase towards various application

Preparation.

Besides the 1T′-MoS_2, $MoSe_2$, and MoSSe, our electrochemical intercalation method should be able to prepare many other 1T′-TMD nanosheets which have not been investigated yet. Firstly, many recently reported 1T′-TMDs crystals can be exfoliated by our newly developed electrochemical intercalation method. For example, 1T′-$MoTe_2$ crystals have been investigated for years and exhibit quite unique properties in superconducting, electronic devices, and many other applications. However, the exfoliation of 1T′-$MoTe_2$ crystals into nanosheets is rarely reported. By using our electrochemical intercalation method, the 1T′-$MoTe_2$ nanosheets with high phase purity, high quality should be prepared in the future. In addition, many other kinds of 1T′-TMD nanosheets such as metastable $NbSe_2$, NbS_2, TaS_2 nanosheets can be exfoliated from their synthesized 1T′-TMD crystals.

In addition, by carefully tuning the composition and structure of the potassium intercalated TMDs precursor, a variety of new TMDs nanomaterials can be prepared in the future. For example, the lithium intercalated TMDs crystals are regarded as a good precursor to prepared 1T phase TMDs nanosheets. However, by using the traditional lithium

intercalation method, liquid phase exfoliation method, etc., researchers can only get the mixed phase TMDs nanosheets. The main reason is that the lithium intercalation amount is hard to control during the electrochemical method. Due to this, the as-prepared TMDs nanosheets are a mixture of 1T, 1T′ and 2H phase. Therefore, to intercalate the lithium in a more controllable way could be a solution to prepare the 1T TMDs nanomaterials. In this thesis, we already get the K_xMoS_2 crystals as precursors to prepare 1T′ nanosheets. By using the ion-exchange method, the Li-MoS_2 with controllable Li amount is easy to prepare. Once the Li-MoS_2 crystals are obtained, by using our electrochemical intercalation method, MoS_2 nanosheets with high phase purity of 1T phase is easy to prepare. In addition, by using the similar method, many other metal atoms intercalated MoS_2 crystals precursors can be prepared. By using these precursors, novel phase MoS_2 nanosheets can be prepared in the future.

Property and application study.

Based on such results, the intrinsic properties and electronic properties of the obtained novel phase TMDs nanosheets can be exploited. Firstly, the layer-dependent physiochemical could be investigated. 2H-MoS_2 has been proved to experience an indirect to direct bandgap transition when the thickness is reduced from multilayer to monolayer. However, the physicochemical property transition of 1T or 1T′-TMDs nanosheets is rarely discussed due to the limited phase purity. Based on our method, a variety of 1T or 1T′-TMDs nanosheets with different chemical compositions will be prepared in the future. The intrinsic properties of 1T or 1T′-TMDs nanosheets with monolayer, bilayer, trilayer and multilayer will be studied in detail, which will uncover lots of unique properties of 2D nanomaterials. In addition, the 1T′-MoS_2 has been proved with enhanced superconducting properties. Therefore, based on the successful preparation of 1T or 1T′-TMDs nanosheets with high phase purity, the superconducting properties of such materials will be studied in the future. With the unique semimetallic properties and the ultrathin thickness, 1T or 1T′-TMDs nanosheets may become the promising candidate towards the room temperature superconductor.

Furthermore, the 1T or 1T′-TMDs nanosheets could be used in various promising practical applications such as electrocatalysis, energy storage and conversion, electronic devices and so on. For example, the 2H-MoS_2 has been regarded as a promising candidate towards HER due to the high HER activity on the S-edge and the defects within the basal plane. However, the low conductivity, low active site density greatly limits the great potential of traditional 2H-MoS_2, as well as the traditional semiconducting TMDs. The 1T or 1T′-TMDs have been proved with orders of magnitude higher conductivity than the 2H counterpart which shows great potential in the electrocatalysis application. In addition, the basal plane of the 1T or 1T′-TMDs is also characterized with superior HER activity better than the 2H-TMDs. In this case, the 1T or 1T′-TMDs could be regarded as one of the most promising candidates to replace the current used Pt and Pt-based electrocatalysts towards HER. The newly developed electrochemical intercalation method enables us to prepare the 1T or 1T′-TMDs nanosheets with large-scale, high quality and high phase purity. In the future, the HER performance of a variety of 1T or 1T′-TMDs nanosheets will be tested towards practical application. In addition, other different reactions such as OER, ORR, CO_2RR and NRR will also be tested by using the newly prepared 1T or 1T′-TMDs nanosheets as electrocatalysts in the future. In this case, a library of metastable TMD nanosheets can be set up and the detailed phase-dependent properties and functionality can be easily investigated and compared.

6.2.2 Preparation of 1T or 1T′-TMD nanosheets based heterostructure towards promising application

In this thesis, we report the preparation of Pt/1T′-MoS_2 which should the unprecedented HER activity showing great potential in practical water splitting. Such results ignite a new promising way towards the construction of highly efficient electrocatalysis. Besides Pt, various noble metals can be hybridized with 1T′-TMDs, and their properties and functionality are waiting for the intensive study. The following images show the preliminary result of Pd/1T′-MoS_2. As proved by the TEM, SAED and the STEM images, the Pd nanoparticles are grown epitaxially on the 1T′-MoS_2.

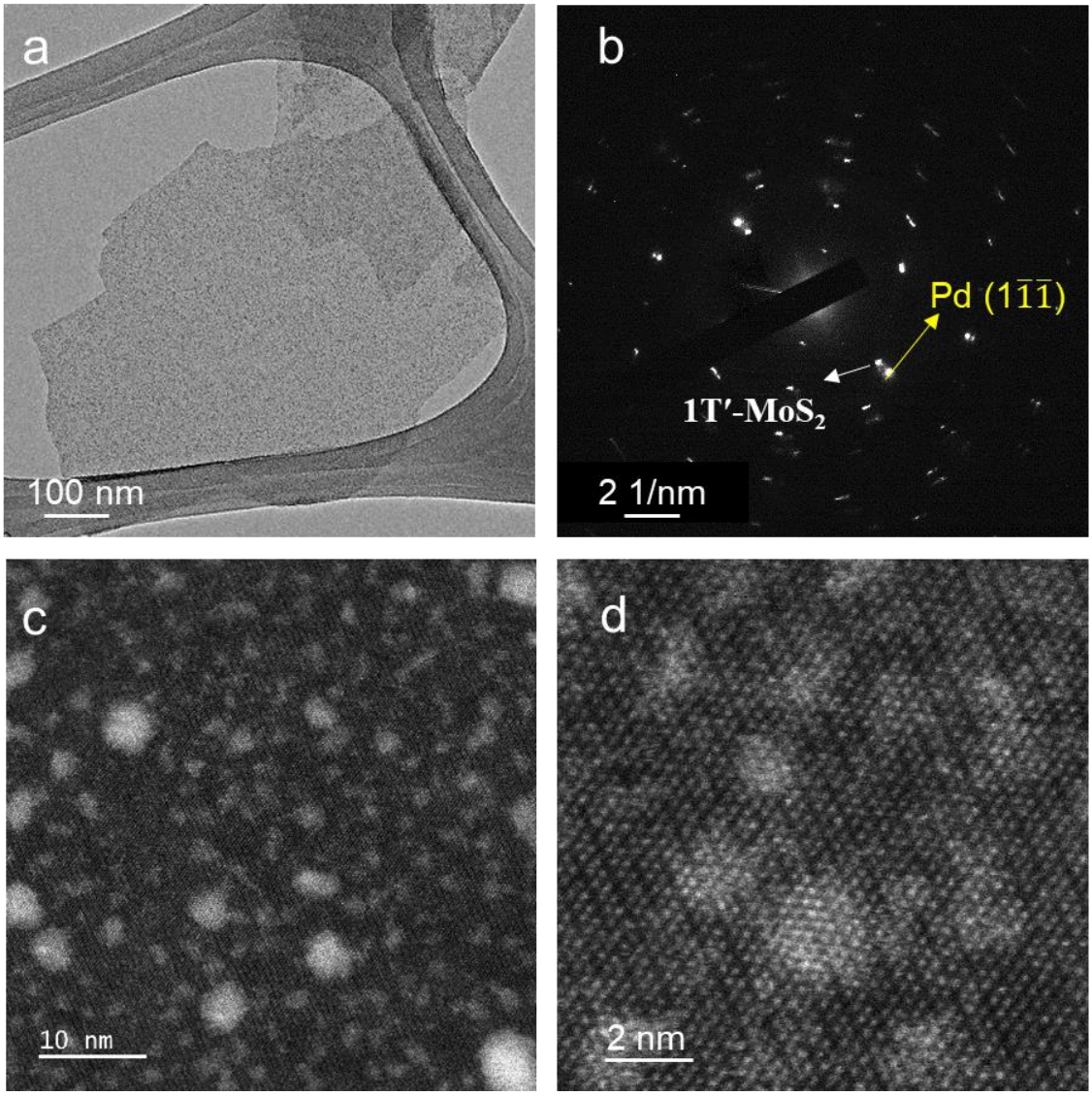

Figure 7.1 a, TEM image and **b**, the corresponding SAED pattern of Pd/1T′-MoS_2. **c**, HAADF-STEM image and **d**, the magnified HAADF-STEM image of Pd/1T′-MoS_2.

Moreover, upon the successful preparation of other 1T or 1T′ TMDs, the epitaxial growth, hybridization, doping, alloying of noble metal on the 1T or 1T′ TMDs can be accomplished. As the 1T or 1T′ TMDs nanosheets high conductivity which benefits the electron transfer, such noble metal-1T or 1T′ TMDs nanomaterials are expected to possess superior electrocatalysis performance. Therefore, after the successful preparation of noble metal-1T or 1T′ TMDs nanomaterials, the electrocatalysis performance towards various reactions

such as HER OER, ORR, CO_2RR and NRR will be tested in the future. Furthermore, various kinds of nanomaterials such as metal oxides, metal sulfide, MOF, COF etc., can be hybridized with 1T or 1T′ TMDs nanosheets towards various promising applications such as electrocatalysis, photocatalysis, chemical sensor, electronics, and energy storage and conversion applications. There's so much work to do in the future.

References

1 Yu, Y. *et al.* High phase-purity 1T′-MoS_2- and 1T′- $MoSe_2$-layered crystals. *Nature Chemistry*, 2018, **10**, 638-643.

2 Lin, Z. *et al.* Solution-processable 2D semiconductors for high-performance large-area electronics. *Nature*, 2018, **562**, 254-258.

Publication list

1. Yiyao Ge†, **Zhenyu Shi**†, Chaoliang Tan, Ye Chen, Hongfei Cheng, Qiyuan He, Hua Zhang*, Two-Dimensional Nanomaterials with Unconventional Phases. *Chem* 2020, 6, 1237-1256. (†equal contribution)
2. Zhuangchai Lai†, Apoorva Chaturvedi†, **Zhenyu Shi**†, Jiangqi Zhao, Thu Ha Tran, Bo Chen, Ying Huang, Xiehong Cao, Qiyuan He, Zhiyuan Zeng, Chaoliang Tan, Hua Zhang, High-Yield Exfoliation of Ultrathin 2D $Ni_3Cr_2P_2S_9$ and $Ni_3Cr_2P_2Se_9$ Nanosheets. *Small* 2021, 2006866. (†equal contribution)
3. Meiting Zhao, Junze Chen, Bo Chen, Xiao Zhang, **Zhenyu Shi**, Zhengqing Liu, Qinglang Ma, Yongwu Peng, Chaoliang Tan, Xue-Jun Wu, Hua Zhang, Selective Epitaxial Growth of Oriented Hierarchical Metal-Organic Framework Heterostructures. *J. Am. Chem. Soc.* 2020, 142, 19, 8953–8961.
4. Zhuangchai Lai†, Qiyuan He†, Thu Ha Tran†, D. V. Maheswar Repaka†, Dong-Dong Zhou, Ying Sun, Shibo Xi, Yongxin Li, Apoorva Chaturvedi, Chaoliang Tan, Bo Chen, Gwang-Hyeon Nam, Bing Li, Chongyi Ling, Wei Zhai, **Zhenyu Shi**, Dianyi Hu, Vinay Sharma, Zhaoning Hu, Ye Chen, Zhicheng Zhang, Yifu Yu, Xiao Renshaw Wang, Raju V. Ramanujan, Yanming Ma, Kedar Hippalgaonkar, and Hua Zhang, *Nat. Mater*. 2021, Accepted.